Somma G.L. (2019) "Adaptive Remediation of the Space Debris Environment using Feedback Control", University of Southampton, Faculty of Engineering and Physical Sciences, PhD Thesis.

UNIVERSITY OF SOUTHAMPTON

FACULTY OF ENGINEERING AND PHYSICAL SCIENCES

Aeronautics, Astronautics and Computational Engineering

ADAPTIVE REMEDIATION OF THE SPACE DEBRIS ENVIRONMENT USING FEEDBACK CONTROL

by

Gian Luigi Somma

Thesis for the degree of Doctor of Philosophy

25 July 2019

Professor Hugh G. Lewis
Faculty of Engineering and Physical Sciences, University of Southampton, United Kingdom,

Professor Camilla Colombo
Department of Aerospace Science and Technology, Politecnico di Milano, Italia.

UNIVERSITY OF SOUTHAMPTON

ABSTRACT

FACULTY OF ENGINEERING AND PHYSICAL SCIENCES

Aeronautics, Astronautics and Computational Engineering

Thesis for the degree of Doctor of Philosophy

ADAPTIVE REMEDIATION OF THE SPACE DEBRIS ENVIRONMENT USING FEEDBACK CONTROL

Gian Luigi Somma

In the last few decades, space-related services became a familiar part of everyday life. Moreover, the commercial use of space is forecast to keep increasing in the near future. However, all the spacecraft which provide these services are subject to the risk of being damaged or destroyed by an orbital collision with space debris. To solve the problem, mitigation measures and common standards were defined at industrial, national, and international levels; nevertheless, the number of debris continues to increase. The active removal of space debris was proposed as a solution, and in recent years, several studies addressed the technical and technological challenges needed to realise the first successful mission.

This thesis aims to identify general rules for increasing the effectiveness of active removal strategies in the low Earth orbit. More than 7,000 simulations were run in total, with the effectiveness of traditional post-mission disposal and active debris removal measures evaluated using the normalised effective reduction factor (NERF) as a common metric to quantify the reduction of the population against worst- and best-case scenarios.

This work uses Model to Investigate control Strategies for Space Debris (MISSD), a new source-sink model of the low Earth orbit (LEO) environment developed in Matlab. Embedded within this model, a feedback controller automatically selects the number and location of objects from two species, inactive payloads, and rocket bodies, to be removed from LEO. Different controls are tested with a proportional, linear, and quadratic laws function of the objects spatial density.

The results demonstrate that it is possible to achieve the same effectiveness with multiple strategies incorporating variations in the post-mission disposal (PMD) compliance and in the number of objects annually removed. The effectiveness of active debris removal (ADR) could be increased by selecting optimal combinations of removals of inactive payloads and rocket bodies. As a general rule, a rise of 30% in PMD compliance produces similar effectiveness to the removal of five additional debris, confirming the primary role of broad adoption of post-mission disposal. For a low number of annual removals, strategies which removed twice the number of rocket bodies compared with the number of inactive payloads results in higher effectiveness, whereas increasing the total annual removal rate and PMD compliance shift the optimal strategy to a more balanced combination of debris species actively removed.

Keywords: space debris, low-Earth orbit, feedback control, adaptive remediation, active debris removal, post-mission disposal

Table of Contents

List of Tables

List of Figures

Declaration of Authorship

I, Gian Luigi Somma

declare that this thesis and the work presented in it are my own and has been generated by me as the result of my own original research.

I confirm that:

- This work was done wholly or mainly while in candidature for a research degree at this University;
- Where any part of this thesis has previously been submitted for a degree or any other qualification at this University or any other institution, this has been clearly stated;
- Where I have consulted the published work of others, this is always clearly attributed;
- Where I have quoted from the work of others, the source is always given. With the exception of such quotations, this thesis is entirely my own work;
- I have acknowledged all the main sources of help;
- Where the thesis is based on work done by myself jointly with others, I have made it clear exactly what was done by others and what I have contributed myself;
- Parts of this work were previously published as:

  Somma, G. L., Lewis, H. G. and Colombo, C. (2016) ‘Adaptive remediation of the space debris environment using feedback control’, in 67th International Astronautical Congress (IAC). Guadalajara, Mexico. Available at: https://eprints.soton.ac.uk/403265/

  Somma, G. L., Lewis, H. G. and Colombo, C. (2017) ‘Sensitivity Analysis for a Space Debris Environment Model’, in 7th European Conference for Aeronautics and Space Sciences. Milan, Italy. doi: http://doi.org/10.13009/EUCASS2017-443 .

  Somma, G. L., Lewis, H. G. and Colombo, C. (2017) ‘Increasing ADR effectiveness via an altitude-shell-dependent removal approach’, in 68th International Astronautical Congress. Adelaide, Australia. Available at: https://www.researchgate.net/publication/329098120

Somma, G. L., Lewis, H. G. and Colombo, C. (2018) ‘Space Debris: Analysis of a Large Constellation at 1200 km Altitude’, in 69th International Astronautical Congress. Bremen, Germany. doi: https://doi.org/10.13140/RG.2.2.34854.98889.

Somma, G. L., Lewis, H. G. and Colombo, C. (2019) ‘Sensitivity analysis of launch activities in Low Earth Orbit’, Acta Astronautica, vol. 158, pp 129-139, doi: https://doi.org/10.1016/j.actaastro.2018.05.043.

Somma, G. L., Lewis, H. G. and Colombo, C. ‘A comparison of active debris removal and post-mission disposal effectiveness in the low Earth orbit’, article in preparation

Signed: ....

Acknowledgements

Firstly, I would like to acknowledge the Faculty of Engineering and Physical Sciences of the University of Southampton, which provided financial support for this work; the Doctoral Training Partnership, which funded part of this work through the Engineering and Physical Sciences Research Council (grant EP/M50662X/1); and the Space Debris Office of the European Space Agency, which provided data on the orbital population and launch traffic.

I thank my supervisors Prof Hugh Lewis and Prof Camilla Colombo for their support and encouragement during this project. At many stages of this doctorate, I benefited from their advice and knowledge, and I am grateful to them, especially for the patience and guidance. Their careful editing contributed enormously to the production of this thesis and other outputs during the whole PhD. In particular, I would like to credit Prof Lewis for teaching me the critical thinking, in which art he is a true master and Prof Colombo for the moral support and the chance to spend a period of my doctorate at the Politecnico di Milano.

My sincere thanks also go to Dr Hodei Urrutxua for the insightful comments, but also for the comments and the hard questions which encouraged me to widen my research from various perspectives. I am grateful to Dr Jennifer Kingston and Dr Ondrej Hovorka for a very pleasant VIVA, full of interesting questions and positive discussions, and for the useful feedback that they provided me to improve the quality of this thesis.

I want to express my gratitude to Richard, the graduate school, and the other administrative financial and general staff at Southampton University for giving me an amazing experience and helping me to grow both personally and professionally.

I would also like to mention Dr Darren McKnight for providing me with a genuine example of an out of the box thinker; Christopher Bonnal for the ever-present kindness and for the several informative communications and invites to space-debris events; Francesca Letizia, Alessandro Rossi, and Luciano Anselmo for providing me documents, ideas, and feedback on my work.

I am very grateful to Prof Andrea Manica, who gave me the chance to be part of his research group in Cambridge during the last months of the writing of this thesis. There I benefitted from a very friendly and productive workspace.

I thank my fellow office mates, in Southampton, Milan and Cambridge, for the entertaining discussion, their friendship and for the coffee-chats!

My sincere gratitude also goes to my girlfriend Michela who supported me in this adventure even before it started, encouraging me to search and apply for PhD positions. She helped me in so many ways during these years that it would be difficult to summarise all of them in a few sentences. A huge hug also goes to Isa and Silvia, they know why, and they deserve it!

Last but not least, I would like to thank my family: my parents and sister for their presence throughout writing this thesis and my life in general. I would also like to acknowledge the people who are not here anymore, but which contributed enormously to my past life, in particular to my father and Michele (*So say we all!*).

So long and thanks for all the fish.

Dal cielo la forza,
dal cuore passione,
dal braccio l'azione,

dal fuoco l'ardore,
dal Sole potenza,
dalla mente il pensiero.

List of Acronyms and abbreviations

ADR	Active Debris Removal
ASAT	Anti-SAtellite Test
CASCADE	Computational Adaptive Solution to Control Accurately the Debris Environment
CIRA	Committee on Space Research International Reference Atmosphere
COPUOS	Committee On the Peaceful Uses of Outer Space
DAMAGE	Debris Analysis and Monitoring Architecture to the Geosynchronous Environment
DELTA	Debris Environment Long-Term Analysis
ERF	Effective Reduction Factor
ESA	European Space Agency
FADE	Fast Debris Evolution
GEO	Geosynchronous Earth Orbit
GEODEEM	GEO space Debris Environment Evolution Model
IADC	Inter-Agency Space Debris Coordination Committee
ISO	International Organization for Standardization
ISS	International Space Station
KSCPROP	KS Canonical Propagation model
LEGEND	LEO-to-GEO Environment Debris model
LEO	Low Earth Orbit
LEODEEM	Low Earth Orbital Debris Environment Evolutionary Model
MASTER	Meteoroid and Space Debris Terrestrial Environment Reference
MEDEE	Modelling the Evolution of Debris in the Earth’s Environment
MISSD	Model for Investigating control Strategies for Space Debris
MRO(s)	Mission Related Object(s)
NASA	National Aeronautics and Space Administration
NERF	Normalised Effective Reduction Factor

PIB	Particles-In-a-Box
PID	Proportional-Integrative-Derivative (controller)
PMD	Post-Mission Disposal
PODEM	Phenomenological Orbital Debris Environment Model
SDM	Semi-Deterministic Model
SFU	Solar Flux Units
SSN	Space Surveillance Network
STAT	STochastic Analog Tool
UN	United Nations
US	United States

List of symbols

Greek symbols

β	Removal coefficient
$\delta_{i,j}$	Kronecker’s delta
ε	Error against the setpoint (in the controller)
Δt	Time interval
Δt_{SOL}	Spacecraft operative life
Δt_{SRL}	Spacecraft residual time (after becoming not operational)
λ	Percentage level of compliance with post-mission disposal guidelines
μ_E	Earth’s gravitational parameter
η	Mean motion
ν	True anomaly
π	Pi
ρ	Density of object in a volume
τ	Characteristic shell residence time
ς	Atmospheric density

Symbols

A	Cross-sectional area of an object
a	Semi-major axis
b	Impact parameter
B	ballistic coefficient
C	Collision coefficient
c_D	Drag coefficient
C_R	Collision rate
D	Decay coefficient
E	Explosion coefficient
e	Orbit eccentricity
f	Collision rate corrective factor
$F_{10.7}$	Solar flux index
h	Altitude shell
h_A	Apogee altitude
h_E	Equivalent circular altitude

h_P	Perigee altitude
k	Control gain
k_ρ	Control gain based on the total density
k_L	Multiplier of the reference launch rate
k_P	Proportional control gain
k_q	Power coefficient used in control law
L	Launch coefficient
L_C	Characteristic length
M	Post-mission disposal coefficient
m	Object's mass
N	Number of objects
n_C	Total number of collisions
n_E	Number of fragments generated in an explosion
n_F	Number of fragments generated in a collision
p	Intrinsic collision probability
R_B	Bottom radius of the selected spherical altitude shell
R_E	Radius of the Earth
R_T	Top radius of the selected spherical altitude shell
R^2	Coefficient of determination
S	Species-dependent unit-less scaling factor (for explosions fragments)
t	Time
t_{end}	Time at the end of simulation
t_{PMD}	Time of post-mission disposal
T_{exo}	Exospheric temperature
U	Control coefficient
u	Annual removal rate
u_{cum}	Cumulative number of objects removed
V	Volume of space
v_c	Orbital circular speed in the middle of altitude shell
v_r	Average relative speed in the considered volume
z	Altitude from Earth's surface
Z	Scale height

Subscripts

0	Initial / reference
AP	Active payloads species
CO	Collision fragments species
EX	Explosion fragments species
f	final
I	Intact species (i.e. rocket bodies, active and inactive payloads)
IP	Inactive payloads species
$\max$	Maximum
$\min$	Minimum
MR	Mission-related objects species
RB	Rocket bodies species
T	Total (all species)

Superscript

$*$	Setpoint / reference
T	Transposed (vector or matrix)

Mathematical entities

$\circ$	Hadamard product
∂	Partial derivative

Chapter 1. Introduction and literature review

This chapter introduces the works with a literature review on the evolution of the orbital population and environment (Section 1.1), mitigation guidelines (Section 1.2), space debris models with a special focus on the PIB method (Section 1.3), and adaptive remediation (Section 1.4). The research scope of this thesis is then illustrated (Section 1.5), and the method introduced (Section 1.6). Lastly, the structure of the thesis is described (Section 1.7).

1.1. The evolution of the orbital debris population

Satellite-based services pervade everyday life and generate a worldwide economy worth more than \$320 billion per year through science, remote sensing and telecommunication (Space Foundation, 2015), with prediction for the next three decades ranging from \$1.1 trillion (according to the Morgan Stanley bank) to \$2.7 trillion (Bank of America Merrill Lynch, 2017). Within this context, the abundance of space debris, and its constant growth poses an increasing threat to current and future space activities. Space debris is defined as “all man-made objects including fragments and elements thereof, in Earth orbit or re-entering the atmosphere, that are non-functional” (Inter-Agency Space Debris Coordination Committee, 2007). Due to their orbital speed in the order of magnitude of kilometres per second, space debris possess high kinetic energy. Therefore, even an object smaller than 1 centimetre can damage, disrupt, or even destroy a satellite, resulting in loss of services and potential costs of hundreds of millions of dollars.

Since the beginning of the space age, the number of orbital debris had an overall steady uptrend (with some period of stagnations due to the decrease in fragmentation debris), accounting now for more than 90% of the current low Earth orbit (LEO) catalogued population (Celestrak, 2014; Union of Concerned Scientists, 2016). Moreover, even without ongoing launch activities, new explosions and collisions are likely to keep degrading the environment, posing a growing threat to future space activities.

The primary hazard derives from in-orbit fragmentation events, i.e. explosions and collisions, which occur mainly with spent rocket stages and inactive spacecraft (i.e. those who completed their mission or failed during their operative time). These types of accidents are able to generate in a single event thousands of new objects, some of which can remain in orbit for decades or even centuries (Talent, 2007). Five major accidental collisions have already been recorded in history[1].

---

[1] The collisions were: the COSMOS 1934 spacecraft with the catalogued debris 13475 (1991), the Cerise spacecraft with the catalogued debris 18208 (1996), the DMSP 5B F5 Thor Burner 2A rocket body with the catalogued debris 26207 (2005), the two spacecraft Cosmos 2251 and Iridium

Among these, only one in 2009, involving the satellites Iridium 33 and Cosmos 2251, was catastrophic, i.e. with enough energy to completely fragment the two bodies involved, producing about 2300 catalogued debris[2] (Pardini and Anselmo, 2014).

Moreover, deliberate destruction of satellites and rocket bodies have also happened: from 1968 to 1982 the United States (US) and the Soviet Union performed a series of anti-satellite tests, producing about 10% of all catalogued breakup debris at that time (Farinella and Cordelli, 1991). More recently, on the 29th March 2019, also India performed an anti-satellite test (ASAT) successfully, shooting down a satellite at 300 km altitude.

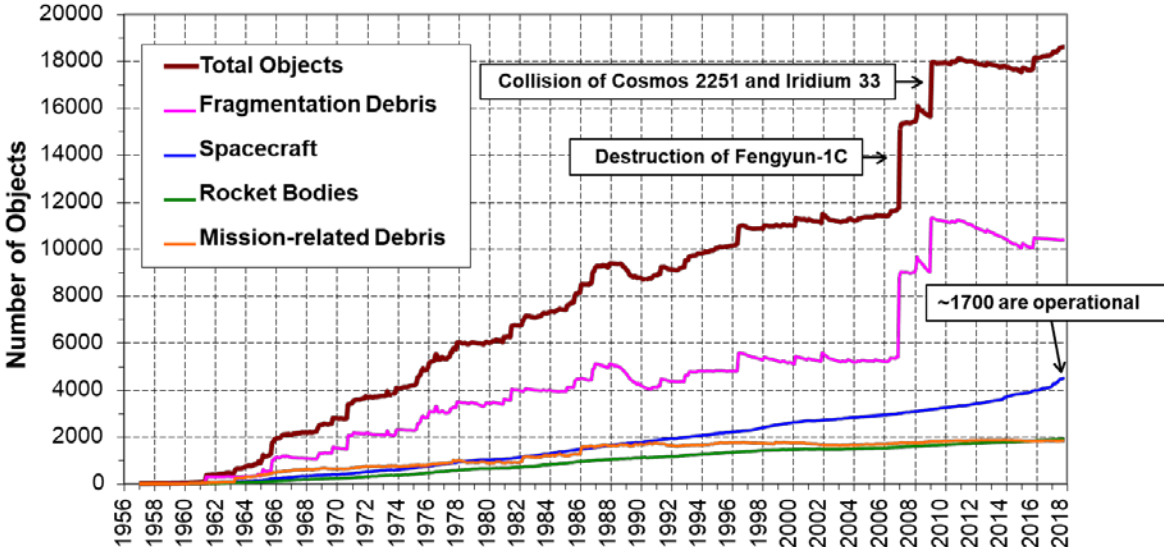

Figure 1-1. Evolution of the orbital population in Earth orbit by object species (Liou, 2018).

Nevertheless, the worst deliberate action was in 2007 with the Fengyun-1C anti-satellite test performed by the People’s Republic of China. This test consisted of the intentional destruction of a weather satellite in orbit at 854 km of altitude, in the middle of the low Earth orbit, the most crowded orbital region. This single event was classified by the National Aeronautics and Space Administration (NASA) as “by far the worst satellite fragmentation of the space age” (Liou, 2007). Indeed, it almost doubled overnight the population of fragmentation debris (Figure 1-1), with about 3,428 distinct new objects tracked (Anz-Meador, 2016a). In 2014, after seven years, more than

---

33 (2009), and the Copernicus Sentinel 1-A with an unidentified mm-size object (2016), most likely a space debris (European Space Agency, 2016).

[2] As of 2013, of the total 2296 debris catalogued, 1668 where of the Cosmos satellites and 628 of the Iridium. As of 4 January 2016, 1141 and 364 debris remained in orbit for a total of 1505, corresponding to 34.9% decay in 7 years (Anz-Meador, 2016a). The number of debris derives from performed via telescopes or lasers observing campaign and are released e.g. via the US Space Surveillance Network (SSN).

90% of the debris produced still remained in orbit (Liou, 2014), while the percentage decreased to 84% in 2017 (Bonnal and Mcknight, 2017).

In 1978 Kessler and Cour-Palais predicted that collisional breakups would become a new source of debris and that the flux of newly generated debris by collisions would exceed the natural meteoroid flux and the natural decay flux in specific orbital regions once a certain threshold is reached (Kessler and Cour-Palais, 1978). This effect, sometimes referred to as the “Kessler syndrome”, also predicts, on an extended period, a self-sustained growth of the debris flux even without any new launch activity. As highlighted by Dolado-Perez et Al., this is true from both a physical and a mathematical point of view, due to an increasing number of objects in space, the physical nature of fragmentation events and the low effectiveness of aerodynamic drag above 700 km as a natural removal method (Dolado-Perez, Pardini and Anselmo, 2015). This means that it could become harder to maintain space activities in certain orbital regions in a sustainable way from both an environmental and economic point of view. For example, to maintain the current launch rate without further damaging the environment, and to guarantee acceptable debris-related failure risks over the satellite’s operational lifespan, there would be a need to invest in spacecraft safety, e.g. on satellite design (shielding, oversized solar arrays, redundant systems) or operations (collision avoidance, mitigation, and remediation measures). Quoting J.-C. Liou: “The orbital debris problem has reached a critical point. The commonly-adopted mitigation measures will not be able to fully control the debris population growth in low Earth orbit” (Liou, 2011a). This is true for the most crowded regions in LEO, while for others it depends on how critical thresholds (i.e. unstable and runaway) are defined and computed (Su, 1993; Rossi *et al.*, 1997, 1998; Kessler and Anz-Meador, 2001) and on the real number of objects present, i.e. including or not the uncatalogued population.

1.2. The mitigation guidelines

In 1978 Kessler and Cour-Palais proposed the idea of applying mitigation policies to the human-made objects launched in space (Kessler and Cour-Palais, 1978). In the following years, recommendations were issued (Kessler, Reynolds and Anz-Meador, 1989) followed by quality standards released by space agencies (e.g. NASA in 1995, the Japanese agency in 1996, the French agency in 1998). At the international level, the Inter-Agency Space Debris Coordination Committee (IADC) was established in 1993 (after an informal meeting in 1987). In 2002, its members reached an agreement on common guidelines for the reduction of space debris, later revised in 2007 (Inter-Agency Space Debris Coordination Committee, 2007), and with a third revision expected by 2019. The United Nations (UN) Committee On the Peaceful Uses of Outer Space (COPUOS) issued in February 2007 their set of guidelines (United Nations Committee On the Peaceful Uses of Outer Space, 2007). In 2010, they recognised space debris as a problem concerning all space-faring nations (United Nations Committee On the Peaceful Uses of Outer

Space, 2010), while in June 2016 the Committee reached consensus on the first set of 12 common guidelines for long-term sustainability of outer space activities (Anz-Meador, 2016b; United Nations Committee On the Peaceful Uses of Outer Space, 2017).

In 2010 the International Organization for Standardization (ISO[3]) produced the first issue of the standards for dealing with space debris mitigations (ISO 24113:2010), later revised in 2011 (ISO 24113:2011) and currently under a further revision (International Organization for Standardization, 2010). However, many other ISO standards have been produced in relation to space debris (Stokes *et al.*, 2017).

In general, all the guidelines and standards agreed on some common practices:

- Limit the release of mission-related objects (MROs) during normal operations;
- Minimise the potential for on-orbit break-ups and prevent on-orbit collisions;
- Apply post-mission disposal (PMD) measures to objects residing in or passing through the LEO and Geosynchronous Earth orbit (GEO) regions. This could be achieved by manoeuvring the spacecraft at the end of its mission into a one of the so-called graveyard regions above LEO or out of the GEO protected region (GEO altitude ± 200 km, $\pm 15°$, Figure 1-2) or into an orbit with a residual lifetime of 25 or fewer years, or performing a safe direct re-entry into Earth's atmosphere.

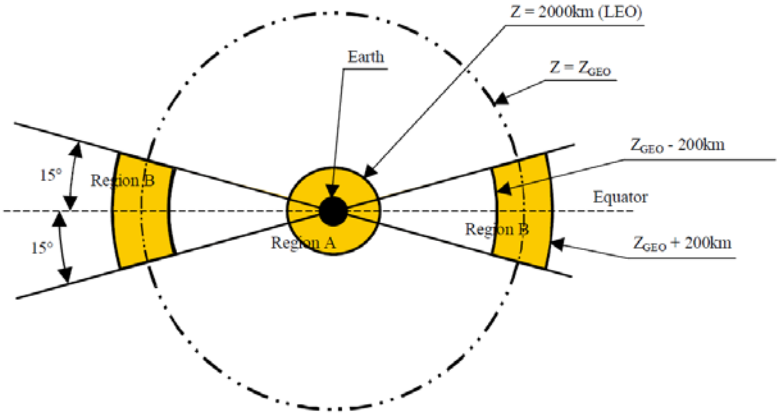

Figure 1-2. The protected region around Earth.

Satellite manufacturers and operators are gradually implementing these measures, but the lack of a legally binding worldwide framework limits their widespread adoption to the signatories of specific

---

[3] ISO is not an acronym but an abbreviation. Because the association name would have a different acronym in different languages, the organisation founder chose the name "ISO" from the Greek term *isos*, meaning equal.

agreements, such the UK's Outer Space Act (The United Kingdom, 1986) or the European code of conduct for orbital debris (ESA, 2004), or to the voluntary adoption of measures not legally binding under international law (United Nations Committee On the Peaceful Uses of Outer Space, 2010)[4].

Space debris guidelines and industry standards are becoming increasingly relevant as tools to enable the stability and sustainability of the whole space environment, i.e. the ability to maintain a dynamic equilibrium in the population and to keep performing space activities with an acceptable risk level in the future.

Some studies reported that PMD has yet to achieve a constant widespread adoption in LEO even if it is the single most effective mitigation measure (Lewis, White and Stokes, 2012), with the projected global level of compliance for the spacecraft launched between 2000 and 2012 being only 23% for satellites and 18% for launchers. When also including the natural decay, the compliance raises to about 58% for spacecraft and 60% for launchers (Morand *et al.*, 2014; ESA Space Debris Office, 2018). However, many uncertainties are linked to these numbers, with the percentage of compliant spacecraft varying greatly over the years and in many cases with no clear trend emerging from the historical data (ESA Space Debris Office, 2018). In addition, it exists a time delay (sometimes even decades) from the mission concept and design to its actual launch. Therefore, at least part of the considered spacecraft were conceived many years ago and the resulting statistics might not completely reflect the level of implementation of the mitigation guidelines for the spacecraft currently being designed or just launched.

Some authors concluded that, the application of these guidelines are slowing down the population growth (Krisko, Johnson and Opiela, 2001; Walker *et al.*, 2001; Liou and Johnson, 2005; Liou, 2011b), but simulations indicated that the future population is likely to have a steady increase in the next 200 years (Liou and Johnson, 2009; Liou, 2011c; Liou *et al.*, 2013). However, results from these studies also showed that thanks to mitigation measures, the orbital population growth shifted from an exponential toward a linear trend.

The major sources of orbital debris are the fragmentation events which may occur as a result of a spacecraft explosion (e.g. from batteries failures) or due to a debris collision with bigger and more massive objects, such as derelict spent orbital stages or satellites. Preventing some of these collisions, together with the widespread adoption of other mitigation measures, could be the key to limit the increase of fragmentation objects. While it is currently possible to reduce the explosion risk by passivating spacecraft at the end of their operative life, it may become possible in the near

---

[4] The European Centre for Space Law compiled on their website a comprehensive list of the national space legislation (European Space Agency, 2011).

future to decrease the collision risk by removing the most dangerous objects from space with the active retrieval of objects from the space environment.

The concept of active debris removal (ADR) was initially proposed more than 35 years ago with the Space Shuttle acting as retrieval spacecraft (NASA Orbital Debris Program Office, 2001).To this date, excluding some satellites retrieved by crewed Space Shuttle, no spacecraft has ever been actively removed from space by an autonomous mission. However, in recent years, an increased interest in this subject led to new studies and new concepts, such as. harpoons, nets, robotic arms, ion shepherd, and laser ablation (Bonnal, Ruault and Desjean, 2013b). Moreover, the technology readiness level of the hardware and technologies required by ADR has significantly increased thanks to ground tests and demonstrative orbital missions, planned (e.g. e.Inspector, CleanSpace One, ELSA-d) or already launched (e.g. the technology demonstrator mission RemoveDebris (Taylor *et al.*, 2018)). Nevertheless, ADR should not be taken as the universal solution to the space debris problem. Indeed, to lower the collision risk in a specific orbital region, dozens of removals might be needed to prevent a single collision (White and Lewis, 2014a), while even investing billions of dollars and removing hundreds of objects will not prevent some type of collisions, such as those between two uncatalogued objects. Nowadays, space operators continuously monitor space for both catalogued and uncatalogued debris, which could pose a threat to their operational spacecraft. When requested (i.e. when over a certain risk threshold), they respond to the collision warnings planning and performing collision avoidance manoeuvres to decrease the risk for their spacecraft. For example, the International Space Station (ISS) performed 25 manoeuvres from its launch (in 1998) to January 2018 (Corley, 2016; Liou, 2018)[5]. A collision avoidance manoeuvre might have also prevented the Iridium-Cosmos collision since the Iridium satellite was still active and manoeuvrable at the time of the collision (Pardini and Anselmo, 2014). Even if public data (obtained from the known orbital positions and orbit trajectories) provided a close approach of 584 meters (Celestrak, 2012), the actual collision was not the highest priority one identified by proximity warnings; moreover, uncertainties on relative position make manoeuvres decision very difficult. It must be pointed out that collision avoidance has a small impact on the long-term sustainability of space activities (Lewis, White and Stokes, 2012). Indeed, even if such manoeuvres can reduce (or even eliminate) the probability of some specific collisions (e.g. with tracked objects), they cannot be performed with an untracked object or between two non-manoeuvrable objects (even if they are derelict and tracked or operational but with not enough fuel), with this latter case which constitute the most likely collision scenario. For addressing this issue, the concept of just-in-time collision avoidance (JCA) was proposed as a possible solution (see Figure 1-3) (Mcknight *et al.*, 2013).

---

[5] The first debris avoidance manoeuvre performed by the ISS occurred on the 26th October 1999 (NASA Orbital Debris Program Office, 2000).

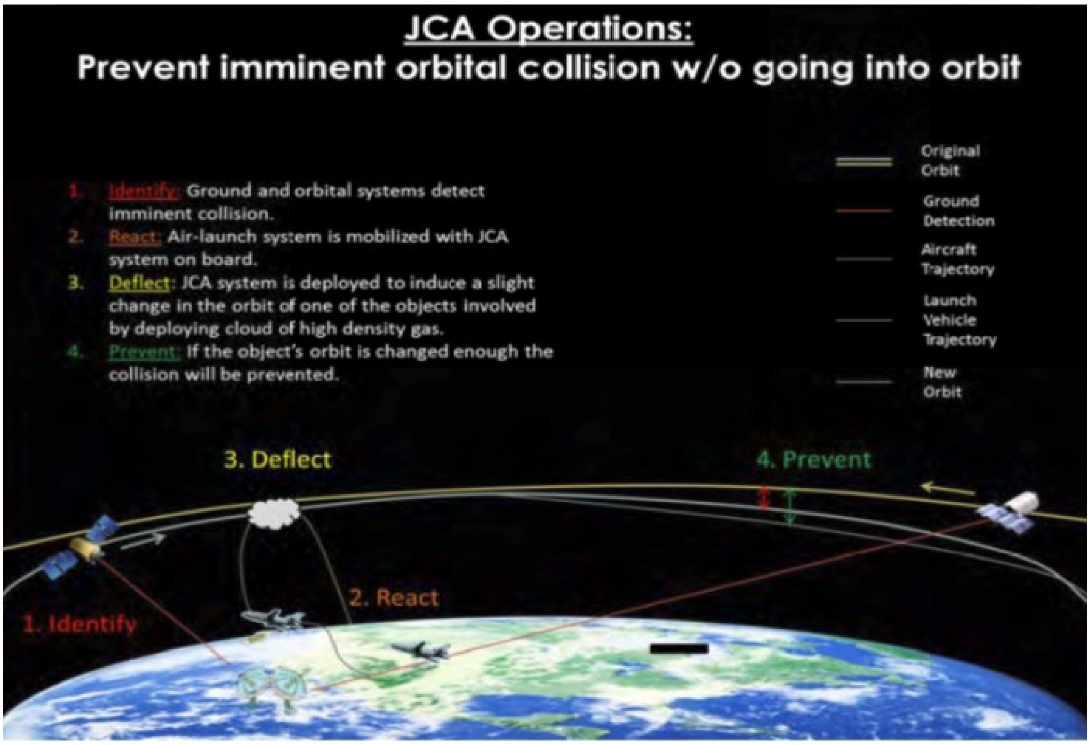

JCA Operations:

Prevent imminent orbital collision w/o going into orbit

1. Identify: Ground and orbital systems detect imminent collision.
2. React: Air-launch system is mobilized with JCA system on board.
3. Deflect: JCA system is deployed to induce a slight change in the orbit of one of the objects involved by deploying cloud of high density gas.
4. Prevent: If the object's orbit is changed enough the collision will be prevented.

Figure 1-3. A visual representation of the just-in-time collision avoidance concept (Bonnal and Mcknight, 2017).

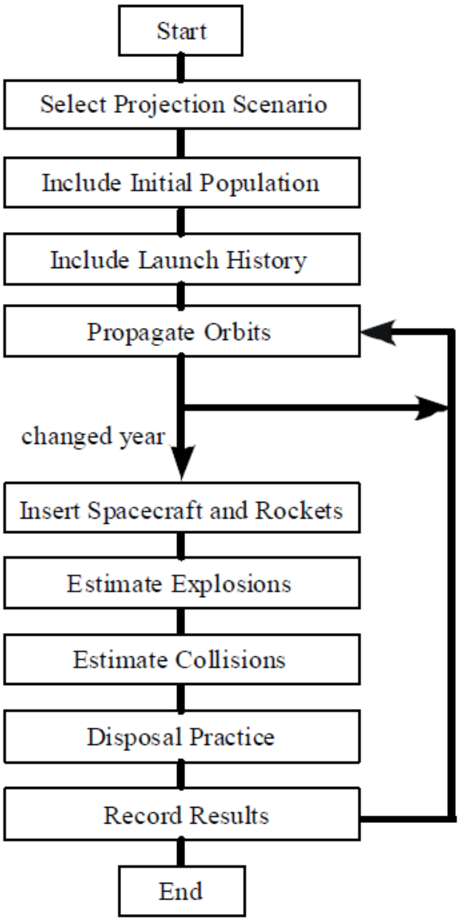

Figure 1-4. Flux diagram of the GEODEEM model (Ariyoshi and Hanada, 2009).

1.3. Space debris models

Over the years, many models of the space environment have been developed by space agencies, public and private institutions. These models used different approaches and assumptions to analyse the current situation, predict possible future scenarios, and test actual or proposed mitigation guidelines. Some of them modelled the space around Earth as mono-, or multi-dimensional (Lewis et al., 2001; Liou et al., 2004) with altitude, eccentricity and inclination bins (Rossi et al., 1997; Kebschull et al., 2013). Depending on the research objective, some models were limited just to a single zone (e.g. GEO space Debris Environment Evolution Model, GEODEEM, for the geosynchronous Earth orbit, Figure 1-4 (Ariyoshi and Hanada, 2009)), while others were able to simulate more regions (Rossi, Cordelli and Pardini, 1995; Walker et al., 2001; Liou et al., 2004). Different approaches were also used, such as stochastic (Rossi, Cordelli and Pardini, 1995), probabilistic (Reynolds, Fischer and Edgecombe, 1983), (semi-) deterministic (Lewis et al., 2001; Walker et al., 2001; Liou et al., 2004; Rossi et al., 2009; Flegel et al., 2011; Dolado-Perez, Di Costanzo and Revelin, 2013; Radtke et al., 2014), or even mixed ones (Eichler and Rex, 1990; White and Lewis, 2014a), as depicted in Figure 1-5.

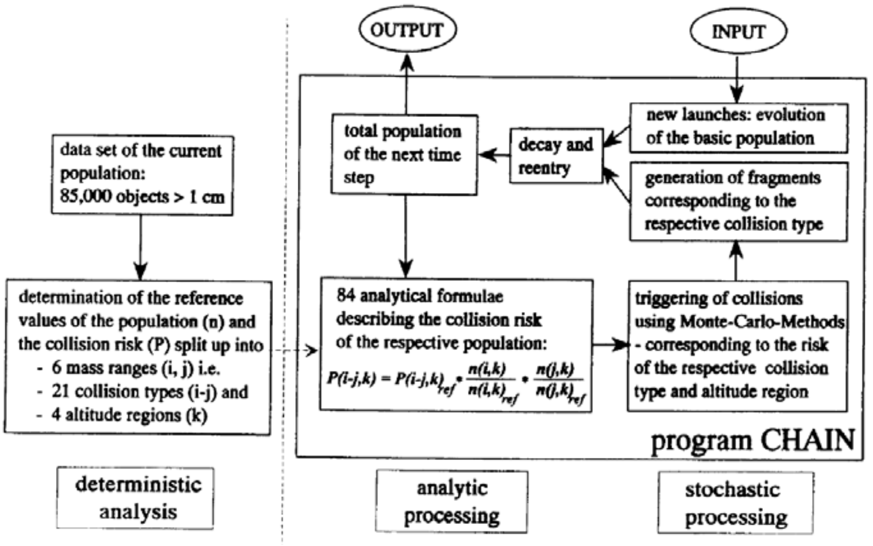

Figure 1-5. The logic flow of the “CHAIN” program (Eichler and Reynolds, 1995).

The models that propagate the orbital elements of all the objects in their databases might include several perturbations, e.g. Earth oblateness, effects of the solar cycle and solar radiation pressure. Examples of these models are: Semi-Deterministic Model (SDM,) (Rossi et al., 2009), Debris Environment Long-Term Analysis (DELTA) (Walker et al., 2001), LEO-to-GEO Environment Debris model (LEGEND, Figure 1-7) (Liou et al., 2004), Long-term Utility for Collision Analysis (LUCA) (Radtke et al., 2014), Modelling the Evolution of Debris in the Earth’s Environment (MEDEE) (Dolado-Perez, Di Costanzo and Revelin, 2013) and Debris Analysis and Monitoring Architecture to the Geosynchronous Environment (DAMAGE, **Error! Reference source not found.**) (Lewis et al., 2001).

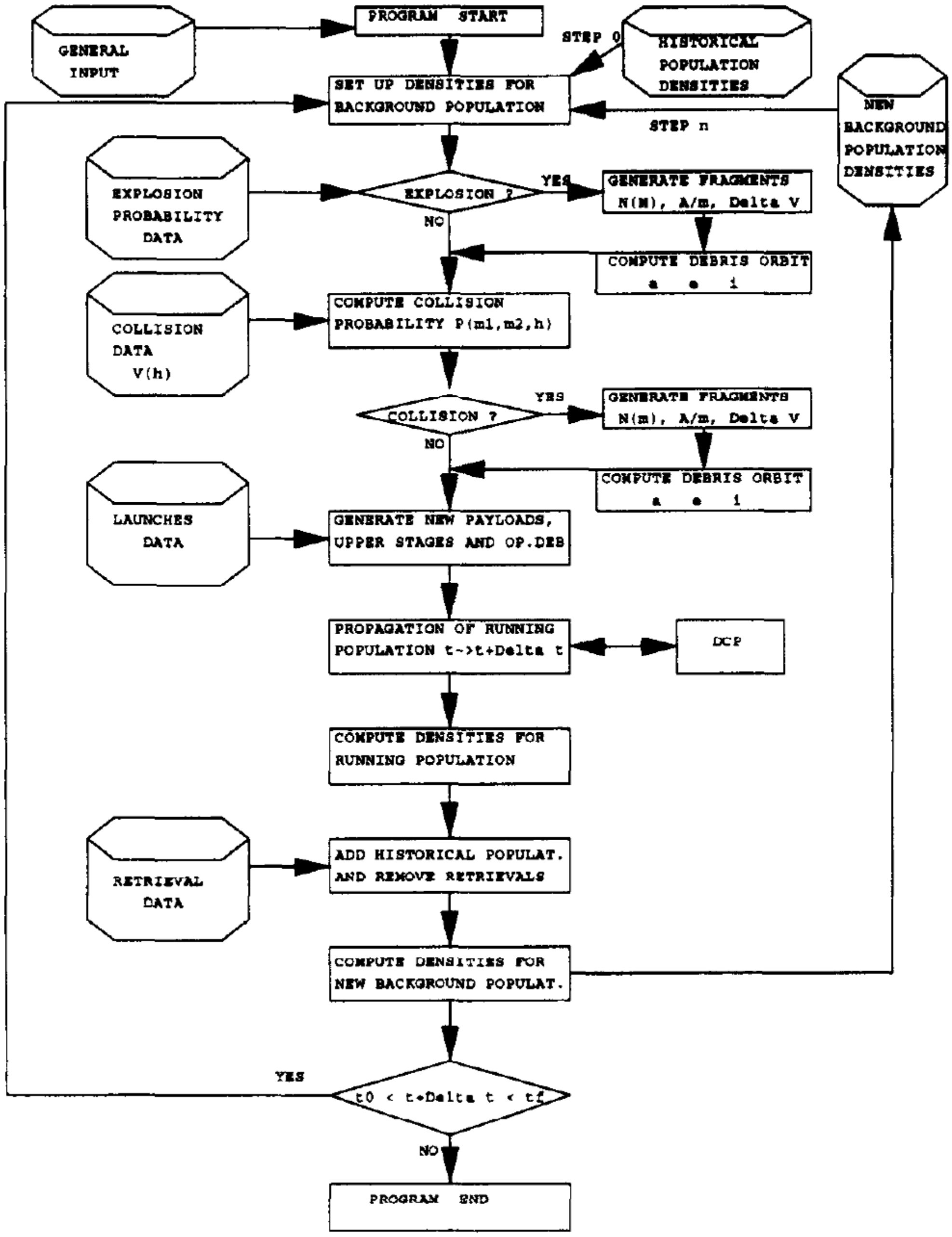

Figure 1-6. Flux diagram of the SDM model (Rossi *et al.*, 1998).

These models sometimes used Monte Carlo approaches, which is a class of algorithms that obtains numerical results repeating the random sampling of stochastic variables on multiple simulations and can describe the likelihood of events based on statistics on the generated results (Vallado, 2013). From the computational point of view, these models are time and power demanding, with dozens or hundreds of simulations that need to be run in order to perform statistics and combine the results into probability density functions of the critical parameters. Indeed, the results obtained in each simulation depended on the set of assumptions and initial conditions used, and on the stochastic events happening during each simulation.

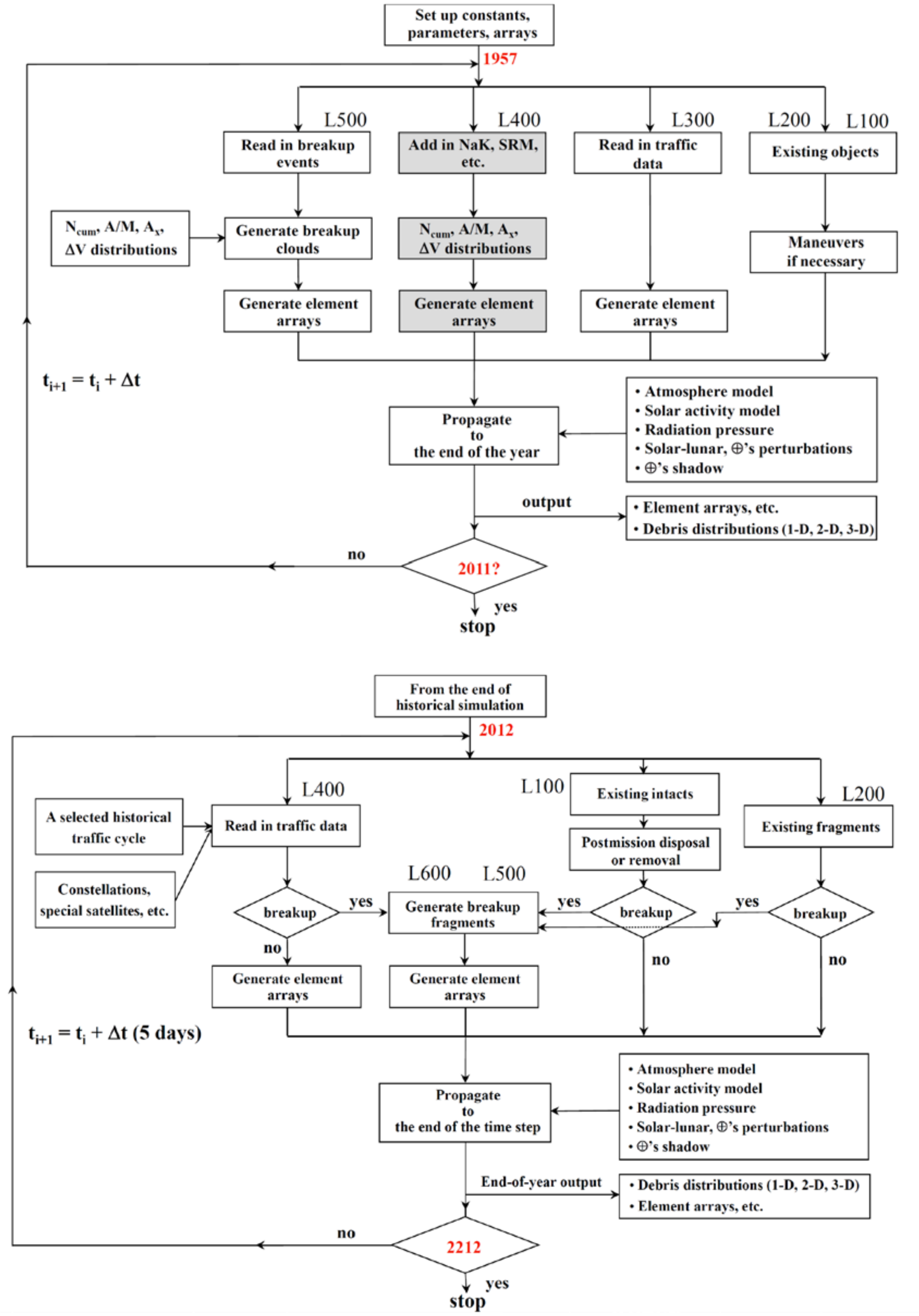

Figure 1-7. Schematics of the LEGEND model (Liou *et al.*, 2004; Liou, 2012).

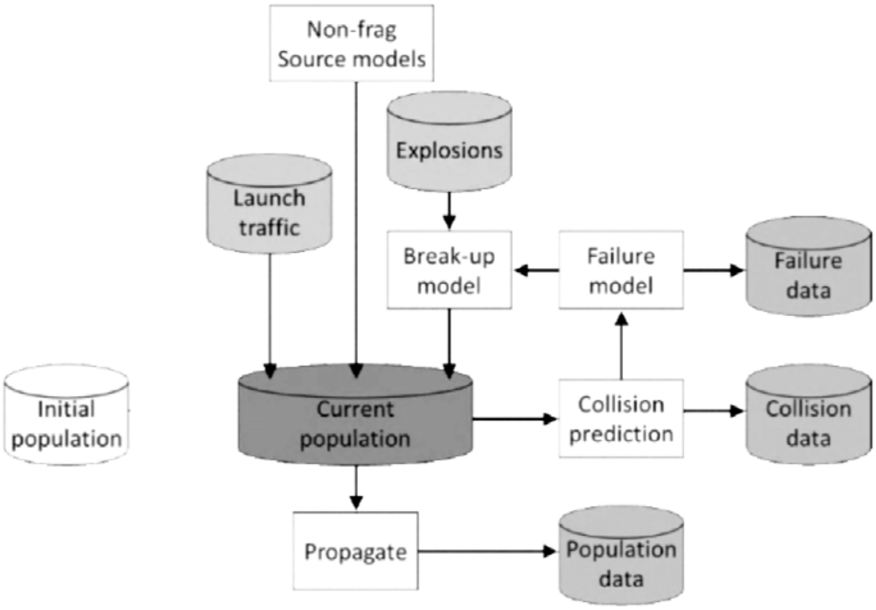

Figure 1-8. Flow diagram of the implementation of DAMAGE per time-step (Lewis, 2011).

1.3.1. History and method of PIB models

In the early debris models developed in the 1980s and 1990s (e.g. Kessler and Cour-Palais, 1978), a different approach was used. These models used mass classes and discretised the altitude with Eulerian (Reynolds, Fischer and Edgecombe, 1983; Su and Kessler, 1985; Eichler and Rex, 1990; Nazarenko, 1997) or Lagrangian meshes (Cordelli, Farinella and Rossi, 1998; Walker *et al.*, 2002) of the near-Earth environment, and did not propagate individual objects. In these works, first-order differential equations described the objects flow into and from the orbital environment, including reinforcing feedback mechanisms (collisions, explosions) and balancing feedback mechanisms (atmospheric decay, PMD, objects removal), while the meshes counted the number of objects in discrete locations in the environment. In the 1990s, several authors used this method (Talent, 1990; Farinella and Cordelli, 1991; Rossi *et al.*, 1997) that is sometimes referred to as Particle-In-a-Box (PIB)[6] because of the collision rate being computed with an equation derived from the kinetic theory of gases.

In particular, Talent modelled the variation of the number of objects with a simple first-order differential equation (Talent, 1990, 1992):

$$\dot{N} = L + \beta N + CN^2 \ , \qquad (1.1)$$

where N is the number of objects in orbit; L is coefficient responsible for objects inserted in the system by launches, which includes the fragments caused by their successive break-ups and a

---

[6] The Particle-in-a-Box term was originally coined by Wetherill in his model of the asteroid belt (Wetherill, 1967).

negative term linked to the deliberate retrieval of objects; β is a removal factor (with negative value) related to decay and active "decay sweepers" i.e. additional ADR linked to the number of objects present in orbit; and C is a collision coefficient linked to the collision frequency and computed borrowing the same theory behind collision among particles in a gas. The underlying assumption was that each object could access and move at random in all the available volume. These assumptions are valid for gasses but not for orbiting objects, which paths are constrained to a small portion of all the available space. For this reason, a corrective factor was also included in the formulation of C (Talent, 1992).

The roots of Equation (1.1) were then found solving the equilibrium case ($\dot{N} = 0$). These roots were determined by the sources and sinks coefficients ($\beta^2 - 4LC$) and defined the stability regions where the populations would asymptotically approach a finite value or grow indefinitely (Figure 1-12). In reality, in this latter case, there will be an increase in the number of collisions among objects over time, which will produce smaller particles with a shorter orbital lifetime.

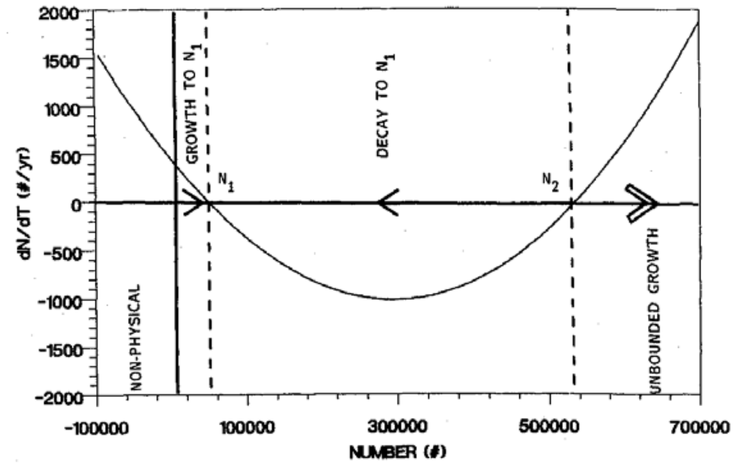

Figure 1-9. The stability regimes as related to the roots of the Equation (1.1) (Talent, 1992).

In 1991, another simple mathematical model was introduced independently in (Farinella and Cordelli, 1991). This similar model produced comparable results, using a pair of first-order differential equations. Some years later another source-sink model, called STochastic Analog Tool (STAT) used a multi-shell approach with 15 altitude shells and one object species but with ten mass bins for a total set of 150 coupled, non-linear first-order differential equations (Rossi *et al.*, 1994). The altitude shells were 50 km thick between 400 and 700 km and 100 km thick up to 1600 km while a mass bins had a logarithmic distribution from 1 g to 6000 kg. The collision rate was obtained using the intrinsic collision probability per unit of time (see Equation (2.17)).

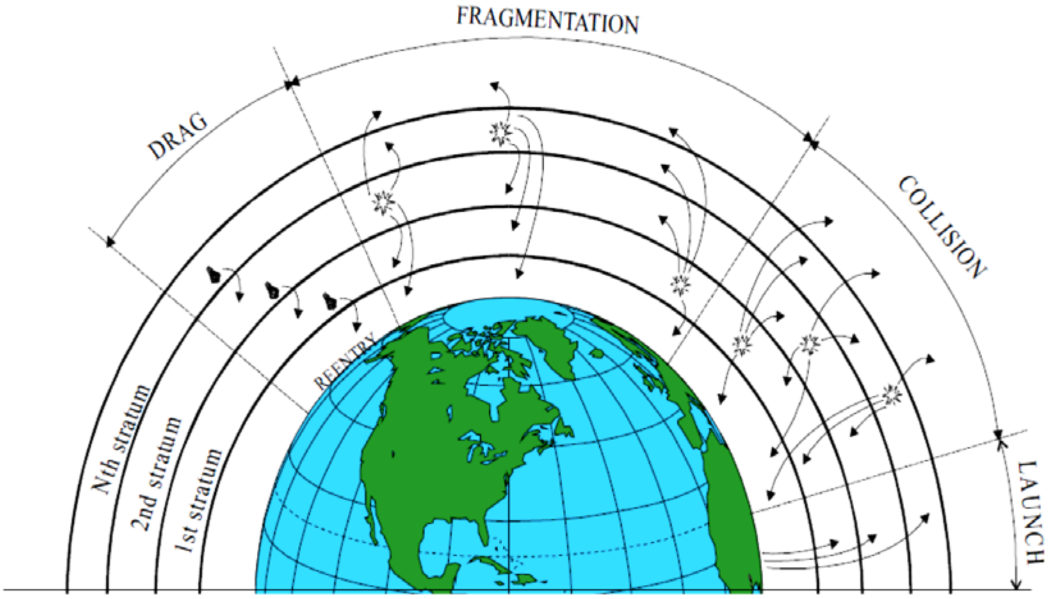

Figure 1-10. Illustration of the elements of PODEM (Talent, 2007).

In 1999, Anselmo, Rossi and Pardini used the same approach for computing collision rates (Anselmo, Rossi and Pardini, 1999). Fifteen years later, Pardini and Anselmo used in their model (with ten altitude shells of 200 km from 0 to 2,000 km) three similar relationships for computing the collision rates for intact-intact, intact-fragmented and fragmented-fragmented objects (Pardini and Anselmo, 2014). Conversely, Lewis et al. used a different approach for computing collision rates in FADE (Lewis *et al.*, 2009b) with a fixed empirical law relating the collision rate by a quadratic expression to the total number of objects in orbit for intact objects, explosion and collision fragments in the only altitude shell present.

Based on his previous research, Talent created and patented a model in 2004, called Phenomenological Orbital Debris Environment Model (PODEM, Figure 1-10) (Talent, 2007), with five particle types and ten attitude shells, for a total of 50 equations. In 2011 Bennett and Sang developed a model with 18 shells of 100 km thickness from 200 to 2,000 km and ten logarithmic mass bins (Bennett and Sang, 2011) and an exponential atmospheric model. The governing equation for this model was similar to the one used by Talent (Equation (1.1)):

$$\dot{N}_{ij}(t) = L_{ij} + D_{ij}(t,N) + C_{ij}(t,N^2) + E_{ij} \ , \tag{1.2}$$

where $\mathbf{L}$, $\mathbf{D}$, $\mathbf{C}$ and $\mathbf{E}$ represent the objects injected or removed into the shell, i and mass species j respectively due to launches, orbital decay, collisions and explosions. The Equation (1.2) does not represent a linear system because the decay term $\mathbf{D}$ includes an implicit linear dependence on the number of objects and the collision term $\mathbf{C}$ has a quadratic one. Another multi-bin model was developed in 2013 by Kebschull et al. (Kebschull *et al.*, 2013, 2014), with the LEO divided into altitude shells, diameter and eccentricity bins, but with only two object species: intact objects and fragments (Figure 1-11). Lastly, a model derived from the work discussed in this thesis has been recently presented (Lucken and Giolito, 2018).

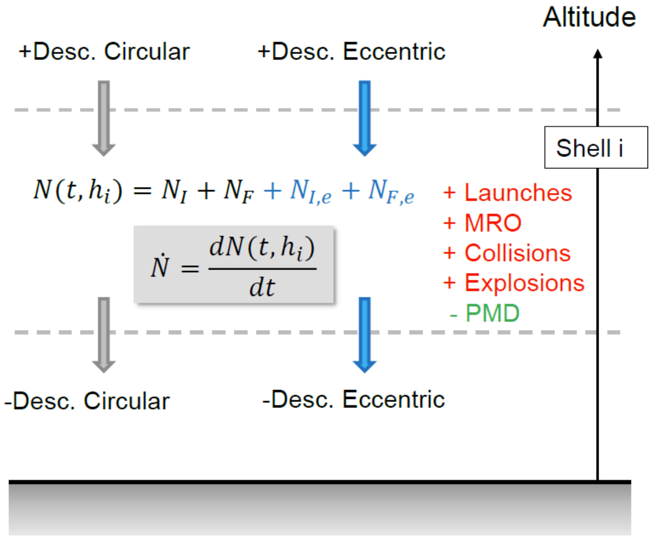

Figure 1-11. Schematics of the source and sink mechanisms of the model developed by Kebschull et al. (Kebschull *et al.*, 2014)

A known drawback of this type of model, resulting from the way the space system is modelled, is the inability to produce a list of the most dangerous objects in space and a reliable collision rate among the objects. Indeed, in PIB models, the collision rate is highly dependent on the considered volume, and the objects are assumed to be uniformly distributed, while in reality collisions are linked to the objects' orbits and relative velocities. Those latter could range from co-planar (e.g. multiple objects in Sun-Synchronous orbits) to opposite or perpendicular (e.g. near Earth's poles where the orbital planes could intersect at different angles). However, this issue can be, at least partially, corrected with the introduction of a corrective factor on the collision rate (as done in Equation (1.1)) obtained for example from a comparison of the collision rate obtained from other models.

The same gas-particle derived approach for computing collisions in PIB models is used with the "Cube" or Cube-derived approach in more traditional models, such as LEGEND (Liou *et al.*, 2003; Liou, 2006), MEDEE and DAMAGE (Lewis *et al.*, 2001; Dolado-Perez, Di Costanzo and Revelin, 2013; Revelin, Di Costanzo and Dolado-Perez, 2015). In these models, however, the volumes considered are much smaller, with the side of the cube usually ranging from 5 to 50 km. In 2014, Blake and Lewis studied the collision rates varying the side of the cube from 1 to 100 km (Blake and Lewis, 2014) using two different models. They highlighted the inverse proportional relationship between the cube size and the collision rate, with the lower average error between theoretical and observed collision rates occurring for the bigger cube tested (and shortest time interval) in one model and consistent rates for cube sizes bigger than 5 km of side in DAMAGE (which use a modified version of the cube approach).

PIB models have advantages when the time or computational resources are limited, the populations are very large, e.g. when considering objects smaller than 10 centimetres (it exists hundreds of thousands of objects bigger than 1 cm and millions bigger than 1 mm), or the projection times are very long, even ten millennia (Eichler, 1998). Indeed, the simplicity of PIB models can be exploited to significantly reduce the run times, while capturing the same major trends of the evolving orbital populations (Lewis *et al.*, 2009b; Kessler, 2016). For example, the Fast Debris Evolution model (FADE), built for educational purposes, can run almost instantly (with custom inputs) on a web page (Lewis *et al.*, 2009b), while the model developed in this thesis take few seconds to run on an average computer (see Section 2.12).

Acknowledging their limitations, PIB models can produce valid results comparable with models that track and propagate objects' orbits (Talent, 2007). Even if often, due to lack of stochasticity and MC-approach, PIB models provide only an indication of possible futures without detailed statistics on their probabilities. However, if modelled correctly, their results can still be representative and similar to the arithmetically averaged results of MC-derived simulations, or they could be set to provide indicative information on best and worst cases.

In addition, not always the most complex model produces the most reliable results . Agreeing with Don Kessler (Kessler, 2016), most models produce a level of accuracy in the orbit propagation that is unnecessary for determining the probabilities of future events or population evolution. This does not mean that it is not important to establish the level of confidence of some results, but that the same objective could be achieved with simpler models. For example, they could provide insight on stability regimes (Figure 1-9, (Talent, 1992)) or very long-term behaviours (Eichler, 1998), swiftly testing a wide range of scenarios when varying key parameters, and test caveats and advantages of different PMD and ADR strategies.

1.4. ADR adaptive strategies

Several studies have investigated the evolution of the debris population when using active removal strategies (Bonnal, Ruault and Desjean, 2013b; Pardini and Anselmo, 2016). However, most of the studies that included ADR selected a priori the annual number of objects actively removed and maintained that rate at a constant level throughout the simulation time span. Different removal rates were then tested so to optimise a function or performance index based on the orbital population at the end time (see Section 2.9) (Liou and Johnson, 2009; White and Lewis, 2014b).

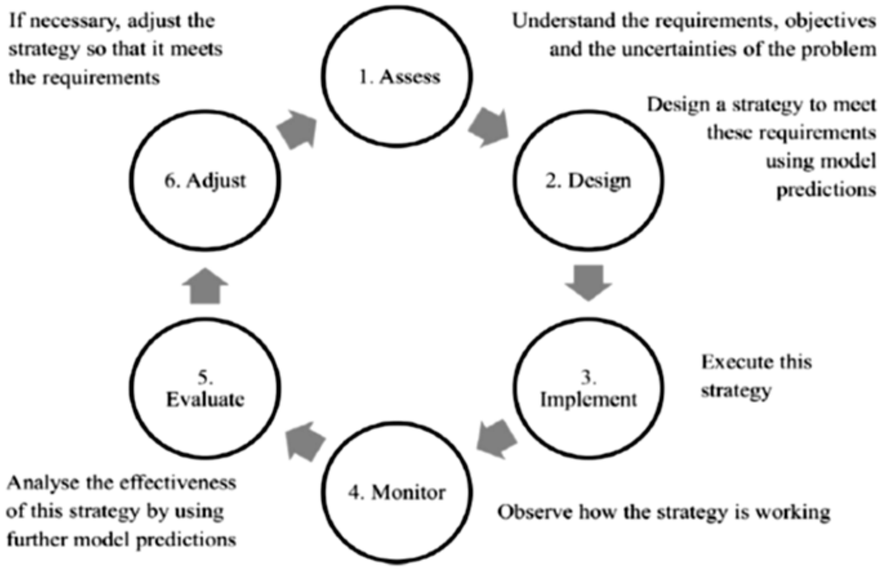

Figure 1-12. The framework for an adaptive strategy (Nyberg, 1999).

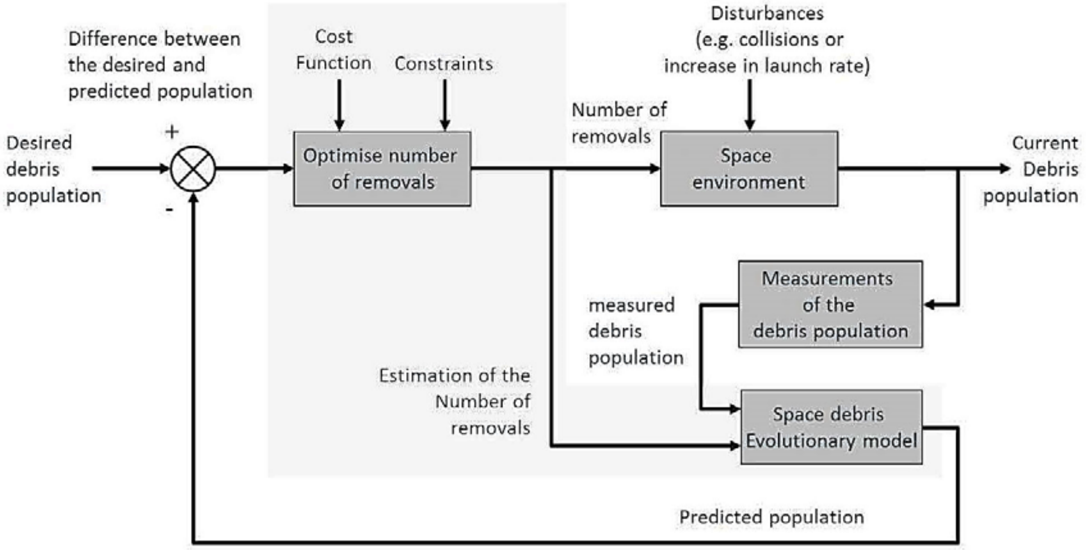

Figure 1-13. Schematics of the model predictive controller for controlling the debris population used by White (White, 2014).

In 2014, a different approach was proposed and used by White and Lewis. They derived a method, called Computational Adaptive Strategy to Control Accurately the Debris Environment (CASCADE), within the DAMAGE model to adjust the number of removals in response to the anticipated evolution of the debris population (White, 2014; White and Lewis, 2014a). In this approach, based on a six-step framework (Figure 1-12), the rate of actively removed objects was not fixed but variable during each simulation. A model predictive control (Figure 1-13) monitored and evaluated the effectiveness of the current strategy and updated the removal rate using an objective function (such as to reach the desired population value). The results of this study demonstrated that an adaptive strategy was more effective compared with a fixed removal rate when the objective was to maintain the current debris population in 200 years (White and Lewis, 2014a).

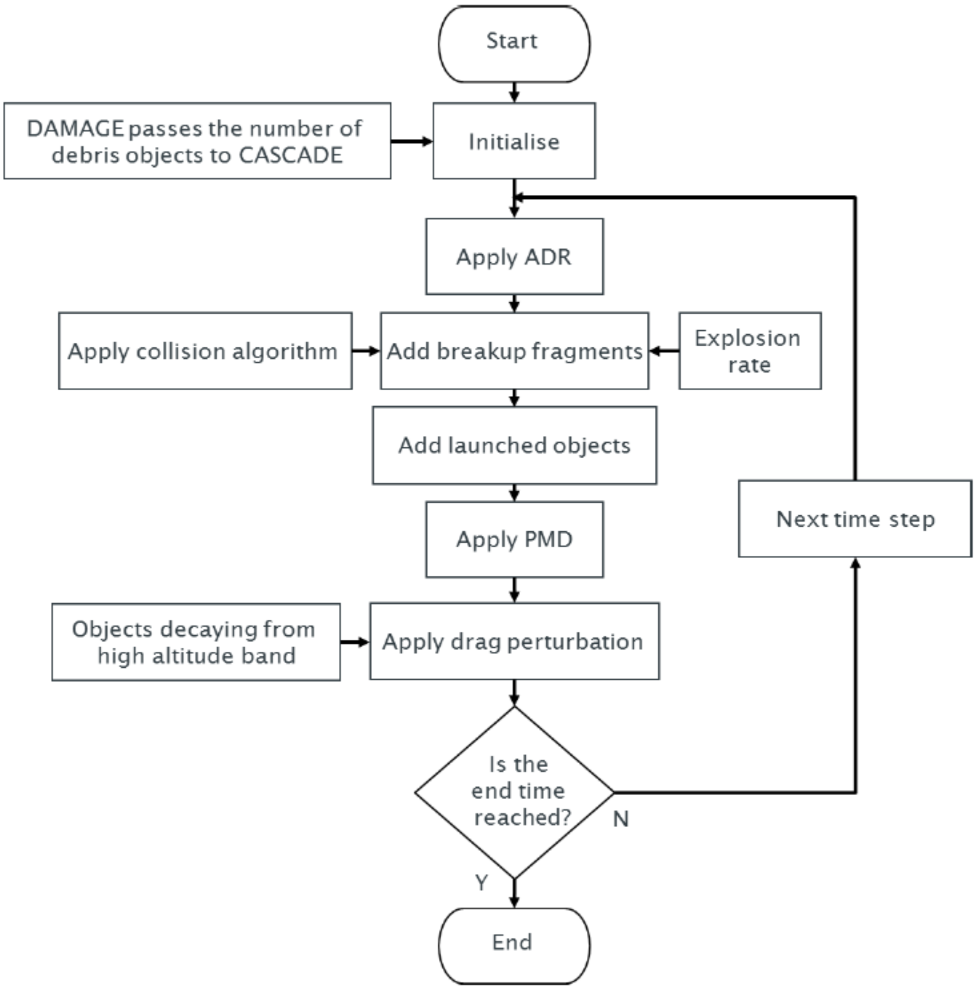

Figure 1-14. A flow diagram of CASCADE model (White, 2014)**.**

1.5. Research scope

In recent years, many works (Emanuelli *et al.*, 2014; Mcknight, 2016; Bonnal and Mcknight, 2017) have focused their attention on ADR as part of the solution to the space debris problem (or as the primary one (DeLuca *et al.*, 2013)). Many options are currently studied, such as (but not limited to) harpoons, nets, tethers, robotic arms, ion shepherd, laser ablation (Bonnal, Ruault and Desjean, 2013b). These researches are trying to address the technical and technological challenges to realise the first successful complete ADR mission. However, from September 2018 to February 2019, an orbital technology demonstrator mission successfully performed experiments with a net capture device, a harpoon, and a visual navigation instrument (Taylor *et al.*, 2018; Surrey Satellite Technology Limited, 2019).

Additional research and funds are needed to make ADR missions feasible, reliable and economically convenient, but the technology readiness level of some of their key components have significantly increased over recent years (Taylor *et al.*, 2018). Waiting for these removal missions to become a reality and common practice, it is possible to theoretically investigate their target and search for removal strategies that would maximise the benefits of ADR strategies on the environment.

Therefore, this thesis aims to answer the following research questions:

- Are there any general rules for increasing the effectiveness of ADR strategies?
- As removing random objects produces only marginal beneficial effects (due to the low collision probability of the majority of objects, compared to those with high mass and collision risk) what species of objects should be actively removed?

The base hypothesis of this thesis is that a Particle-in-a-Box model of LEO with a feedback controller able to act in different ways on different species would be able to answer those questions while providing numerical evidence of the strategies' effectiveness thanks to a performance index.

1.6. Method

In order to fulfil the objectives of this work, a new model of the LEO environment, called Model to Investigate control Strategies for Space Debris (MISSD), was developed in Matlab (Section 2.12 describes its implementation). Embedded within it, a feedback controller regulates how to actively remove a different number of inactive payloads and rocket bodies in various altitude shells based on the selected control law and maximum annual removal rates (Somma, Colombo and Lewis, 2017; Somma, Lewis and Colombo, 2019).

The model uses a source-sink deterministic approach (i.e. stochastic events such as satellite malfunctioning or variation from the assumed solar cycle and are not modelled) with first-order differential equations to compute the evolution of the population for six species of objects: active payloads, inactive payloads, rocket bodies, mission-related objects, collision fragments, and explosion fragments. In every evenly spaced altitude spherical shell in which the LEO region is divided (from 200 to 2,000 km), new objects are created with launches, explosions, and collisions, while removal mechanisms are the natural drag, post-mission disposal (applied at the spacecraft end-of-life), and active debris removal.

The choice of developing a new model removed the limitation due to the adaptation of an existing one to a different purpose and allowed the shaping of an embedded controller. Being built from scratch, MISSD evolved through time, with new components that improved the model and the quality of the results (which were presented on multiple occasions during the doctorate). For example, MISSD evolved in time from a single-shell with three species of objects to a custom number of shells and six object species and introduced only at a later time the solar cycle and the option for objects relocation into lower altitude at the end of their operative life. As a consequence, not all the analyses and results presented in this thesis were carried out at the same time with the same version of the model, resulting in minor differences in the starting conditions or results at the end time. Nevertheless, it was verified that these variations did not influence the overall system dynamics and draw conclusions.

The inspiration for this research came from the work of (White, 2014; White and Lewis, 2014a), where for the first time an adaptive controller was used in the modelling of the space debris problem. The concept of the controller is here investigated more profoundly, with different control laws tested in multiple scenarios. While White focused the attention on adapting the number of removals to be performed, here the focus is on the species to be removed and on the control laws that act differently on them, searching for common rules to increase the overall control effectiveness. Indeed, the developed controller can actively remove a fixed or variable number of objects with different control laws. Differently from White's work, MISSD autonomously selects how many objects to actively remove from each species at different altitudes in LEO based on one among the multiple control laws implemented.

This novel feedback controller is indeed capable of emulating different removal practices, such as (but not limited to) removing only rocket bodies or inactive payloads. The philosophy behind the controller is to reflect the real-life iterative process of reviewing and upgrading the space-related guidelines throughout the years, basing such reviews on the current orbital population and spatial distribution. The feedback controller is a key built-in element of the model which, thanks to the six species implemented, is able to simulate the behaviour and the interactions (e.g. collisions and explosions) within and among each of them based on their characteristics.

1.7. Work structure

This thesis is structured in seven chapters:

- Chapter 1 introduces the works with a literature review on the evolution of the orbital population and environment, mitigation guidelines, space debris models, with a special focus on the PIB method, and adaptive remediation.
- Chapter 2 describes the formulation of the method, with a complete description of the model and the controller, and the selected performance index;
- Chapter 3 illustrates the tuning of the model (with the selection of the integrator time step and number of bands) and a comparative study with other models. Then, it illustrates results from a scenario run with the default parameters before presenting those obtained from sensitivity analysis on PMD compliance and launch rate;

- Chapter 4 presents and discuss analysis performed with the three different control laws. An effectiveness index was used to evaluate the performances of the evolution of the LEO population when subject to different post-mission disposal measures and active debris removal strategies;
- Chapter 5 explores other uses of the model outside its original scope, with the model run without the controller to perform tests on a large synthetic constellation in LEO;
- Chapter 6 summarises the findings and presents a general discussion on the model, assess the importance and impact of the work, and present an outlook of possible future works; finally,
- Chapter 7 draws the conclusions.

Chapter 2. Method

This chapter illustrates the method used to perform the analyses presented in this thesis. The model of the LEO environment is described in detail in Sections 2.1 to 2.7. The different types of controller are listed in Section 2.8, while Section 2.9 presents the effectiveness index used to evaluate the model's performances. Section 2.10 and Section 2.11, describe the initial population and the default model parameters, respectively. Lastly, Section 2.12 reports how the model was implemented in Matlab.

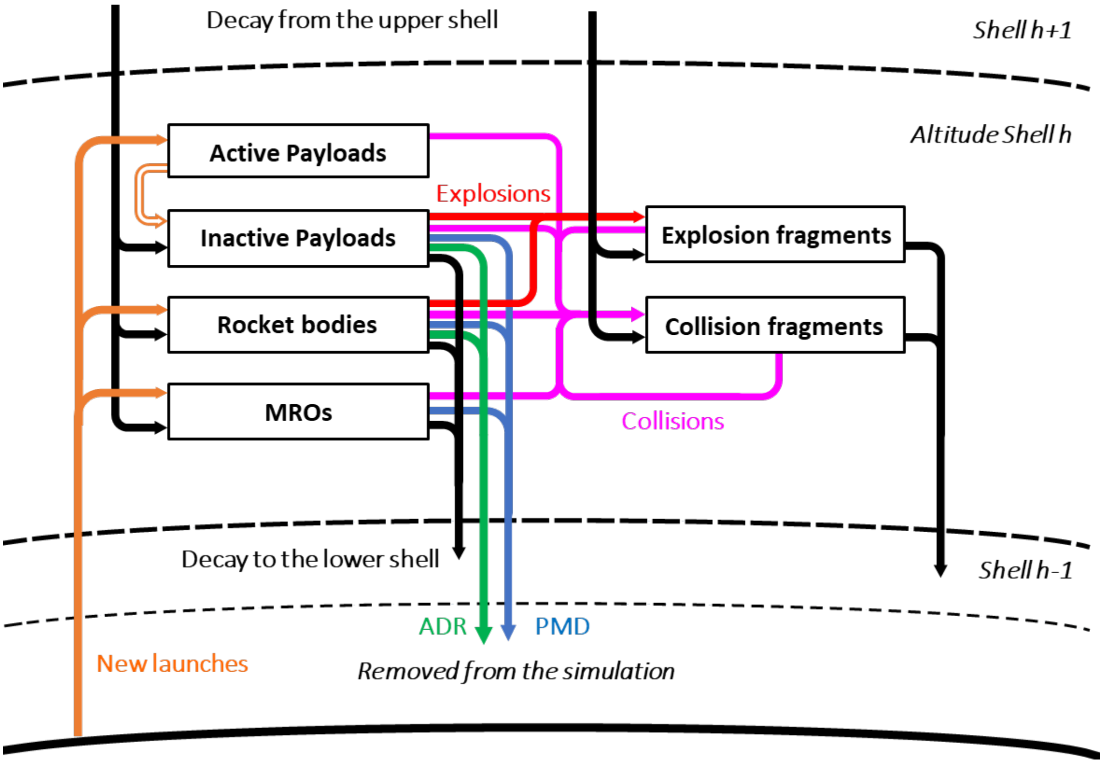

Figure 2-1. Schematic of object species and their interaction in MISSD. Source and sink mechanisms are depicted as inbound and outbound arrows, respectively. New objects are created with launches, explosions, and collisions. Removal mechanisms are natural drag, post-mission disposal, and active debris removal.

2.1. Model description

The analyses presented in this thesis were carried out using the Model for Investigating control Strategies for Space Debris (MISSD), a deterministic source-sink statistical model for the LEO region developed at University of Southampton by the author (Somma, Lewis and Colombo, 2016, 2019; Somma, Colombo and Lewis, 2017). The model can simulate the injection, removal, and interactions of LEO objects from a custom number of evenly spaced spherical altitude shells around the Earth, from 200 to 2,000 km (the default value is 36 shells). Objects are subjects to explosions, collisions, and decay to lower altitude shells due to the atmospheric drag (Figure 2-1).

Differing from other past PIB models of LEO, which often used fewer object species in favour of other physical discretisation (such as area and mass), MISSD implements six object species: active payloads, inactive payloads, rocket bodies, MROs, explosion fragments, and collision fragments. The choice to use these six species was dictated by the goal to simulate the behaviour and the interactions of objects (e.g. the addition, removal, collision) within and among each species based on their characteristics. For example, referring to Equation (2.8) and to the schematics in Figure 2-1 (where inbound and outbound arrows represent the addition or removal of objects from each species), all species are subject to collisions and natural drag, while only inactive payloads and rocket bodies can explode or be actively removed. Even if in recent times there have been some active satellites (i.e. the National Oceanographic and Atmospheric Administration Polar Orbiting Environmental Satellites) that experienced failure and breakups (due to an overcharge in their battery), it was assumed that, in the long-term, the gained experience from such anomalies would improve the reliability of the design. Therefore, the number of those accidental breakup events would decrease in number and neglecting them would have a minimal influence on the orbital population. New launches inject rocket bodies, MROs, and active payloads into the environment, with these latter objects becoming inactive after a set lifetime period. A custom percentage of inactive payloads, rocket bodies and MROs are set to comply with post-mission disposal measures. It was assumed that if a space operator chooses voluntarily or it is mandated to comply with PMD measures, both the satellite, the rocket, and any MRO that might be released, would be subject to the same policy, resulting therefore in the same compliance level for the three types of objects.

A feedback controller (Figure 2-2) is embedded in the model. Following a pre-selected control law who simulates the space policies to be implemented, the controller automatically computes the number and distribution of the objects to be actively removed at each time step from the environment, (Somma, Colombo and Lewis, 2017). At the beginning of each simulation, the user can set different policies to be automatically enforced by the controller. For example, it is possible to remove rocket bodies and inactive payloads each with a fixed or variable rate, with a proportional, linear, or quadratic function of the spatial density in each shell (Section 2.8).

The model does not account for solar radiation pressure. It has, in general, a magnitude lower than other orbital perturbations (such J2 and Luni-Solar perturbation) and has minor effects only on the upper part of LEO, where the satellites have a higher fraction of their orbit not in the Earth’s shadow. Moreover, the resulting variation on the plane orientation and eccentricity would maintain the object in the same spherical shell.

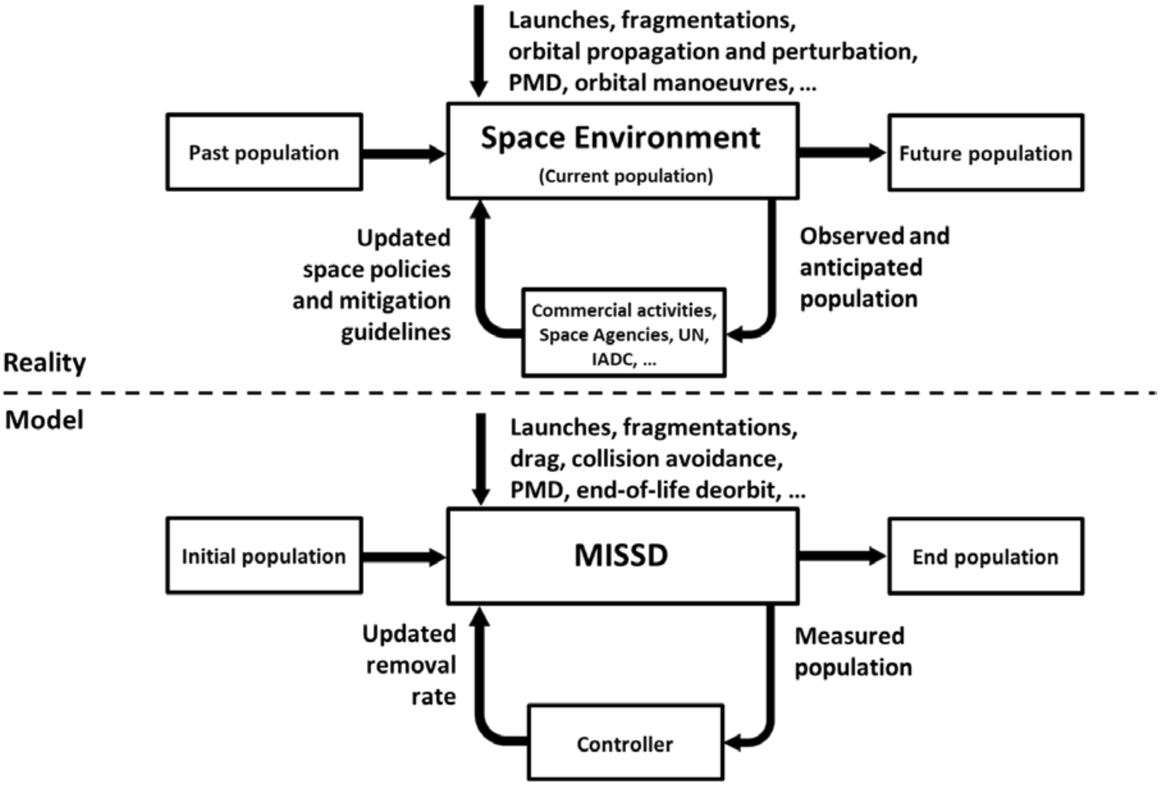

Figure 2-2. Schematics of the interactions among policymakers and stakeholders with the space environment (top) and the model architecture (bottom). The controller simulates the human-driven interaction with the space environment via a feedback loop.

Due to the lack of any geographical and spatial reference of the Earth's surface and gravity (the gravitational potential is assumed to have a spherical symmetry), Earth harmonics, luni-solar and other perturbations were not modelled. This assumption implies that the orbital elements of each object are not subject to variation, except for the semi-major axis, which is reduced by the action of the atmospheric drag. The model does not account for external factors such as the economy (i.e. the cost of remediation measures), politics (i.e., legal responsibility and ownership) or possible future technology.

The lack of perturbations might produce results not accurate enough for some types of study. Indeed, the model is not suitable for specific single-object in-depth investigations (such as the evolution of a collision or explosion debris cloud, or the computation of short-term collision risk for specific objects) due to the statistical approach and the loss of object individuality once injected into the model. These kinds of simulations are instead well suited for 3D orbit propagation models which deal with orbital elements of each specific object in order to propagate in time their orbits.

Requiring a few seconds for a single run on an average computer (see Section 2.12), MISSD can swiftly run several different scenarios, perform sensitivity analysis and parametric studies on initial conditions, and control laws. Test results can be furthermore used to identify unusual single cases to be better investigated later with a more complex model. Furthermore, even if it removes the need for executing Monte Carlo studies to capture basic descriptors of the future environment, this method does not exclude them. If implemented, the total required execution time might be considerably lower compared to other models.

2.2. System governing equations

The model uses a system of nonlinear first-order differential equations to handle the population derivatives (Farinella and Cordelli, 1991; Talent, 1992; Rossi *et al.*, 1994). At every discrete time t, the total population N_T in a specific altitude spherical shell h, is equal to the sum of the six populations:

$$N_T(t,h) = N_{AP}(t,h) + N_{IP}(t,h) + N_{RB}(t,h) + N_{MR}(t,h) + N_{CO}(t,h) + N_{EX}(t,h)\,, \tag{2.1}$$

where the subscripts AP, IP, RB, MR, CO, and EX refer respectively to the object species handled in the model, namely active payloads, inactive payloads, rocket bodies, MROs, collision and explosion fragments. In the same way, the derivative of the total population is expressed by

$$\dot{N}_T(t,h) = \dot{N}_{AP}(t,h) + \dot{N}_{IP}(t,h) + \dot{N}_{RB}(t,h) + \dot{N}_{MR}(t,h) + \dot{N}_{CO}(t,h) + \dot{N}_{EX}(t,h)\,. \tag{2.2}$$

For the whole LEO, Eq. (2.1) and (2.2) become

$$N_T(t) = \sum_h N_T(t,h) \tag{2.3}$$

and

$$\dot{N}_T(t) = \sum_h \dot{N}_T(t,h)\,. \tag{2.4}$$

Each component of Eq. (2.4) can be cross-dependent on the population of other species, as illustrated in Figure 2-1.

To compute the future states, the model uses an explicit Euler method, as done by many other authors (Lewis *et al.*, 2009b; Kebschull *et al.*, 2014; White and Lewis, 2014a):

$$\mathbf{N}(t_{k+1}) = \mathbf{N}(t_k) + \dot{\mathbf{N}}\left(t_k, N\left(t_k\right)\right)\Delta t\,, \tag{2.5}$$

where, for simplicity, only the time dependency is shown, and with

$$t_{k+1} = t_k + \Delta t\,, \tag{2.6}$$

where k is the timestep and Δt is small enough to prevent numerical instabilities. Indeed, the Euler method is a first-order method with a local error at each step of order $O(\Delta t^2)$ and a global error of order $O(\Delta t^1)$. It can be stable only in a specific domain of time, and for this reason, an analysis of the stability region and the selection of the time-step was performed in Section 3.1.1. The use of a higher-order integrator was considered but discarded due to the marginal benefits that could be achieved in exchange for the additional complexity, and a reduction in the time-step was preferred (with minimal effects on the execution time). The choice to implement discrete formulation in time is reflected by the discrete nature of some processes that have been modelled, such as launches, spacecraft lifetimes, removal missions.

Each derivative term in Eq. (2.4) is equal to the sum of six terms (dependencies in the right term were dropped for clarity),

$$\dot{\mathbf{N}}(t,h) = \dot{\mathbf{C}} + \dot{\mathbf{D}} + \dot{\mathbf{E}} + \dot{\mathbf{L}} + \dot{\mathbf{M}} + \dot{\mathbf{U}}, \tag{2.7}$$

where $\dot{\mathbf{C}}(t,h,N(t,h))$ relates to collisions, $\dot{\mathbf{D}}(t,h,N(t,h))$ to drag, $\dot{\mathbf{E}}(t,h)$ to explosions, $\dot{\mathbf{L}}(t,h)$ to launches, $\dot{\mathbf{M}}(t,h,\dot{\mathrm{L}}(t,h))$ to PMD measures, and $\dot{\mathbf{U}}(t,h,N(t,h))$ to the ADR-related control. The drag term depends on the selected and the upper altitude shell (i.e. the object decaying from the upper into the current shell and from the current into the lower one), while the control can be a function of the population in multiple altitude shells.

Rewriting Eq. (2.7) in terms of the six species and applying some assumptions (such as active payloads, MROs and collisions fragments do not explode), a system of six equations is obtained:

$$\begin{cases} \dot{N}_{AP} = +\dot{C}_{AP} + \dot{L}_{AP} + \dot{M}_{AP} \\ \dot{N}_{IP} = +\dot{C}_{IP} + \dot{D}_{IP} + \dot{E}_{IP} + \dot{M}_{IP} + \dot{U}_{IP} \\ \dot{N}_{RB} = +\dot{C}_{RB} + \dot{D}_{RB} + \dot{E}_{RB} + \dot{L}_{RB} + \dot{M}_{RB} + \dot{U}_{RB} \\ \dot{N}_{MR} = +\dot{C}_{MR} + D_{MR} + \dot{L}_{MR} + \dot{M}_{MR} \\ \dot{N}_{CO} = +\dot{C}_{CO} + \dot{D}_{CO} \\ \dot{N}_{EX} = +\dot{C}_{EX} + \dot{D}_{EX} + \dot{E}_{EX} \end{cases}, \tag{2.8}$$

with all the dependencies dropped for clarity. It is not possible to know a priori the sign of some components in Eq. (2.8) since they depend on both the shell and the time. Therefore, all terms are reported with the positive sign to remain consistent with the notation used in Eq. (2.7). For example, the decay terms can be positive or negative depending on the difference in the number of objects decaying from the upper shell and those decaying into the lower one. Conversely all collision and explosion terms, except for $\dot{C}_{CO}$ and $\dot{E}_{EX}$, are always negative (or null) since they remove the objects involved in fragmentation events.

In the model, the variables are assumed to be of the float type (instead of integers). This led to having non-integer values for the object counts and their derivative (e.g. a launch rate of 0.5 objects per year), with these fractional values were not rounded during the simulations. For example, if in a shell there is a launch every two time intervals, the model uses half value in each of the two intervals (from a physical point of view, it could be thought as launching two objects with half the mass). However, this assumption had the repercussion to remove the direct link between the values and their physical meaning as instances of real objects.

2.3. Collisions

The model uses the analytical laws derived from the kinetic theory of gases for computing the collision rate (Houston, 2000), as done by other authors (Farinella and Cordelli, 1991; Talent, 1992; Rossi *et al.*, 1994; Anselmo, Rossi and Pardini, 1999; Ariyoshi and Hanada, 2009), and as presented in Section 1.3.1. A short explanation of the theory is given in Section 2.3.1 to provide background notions on how the collision rate can be computed among particles and how this approach was then adapted for collisions in PIB models (Section 2.3.2) and then in MISSD (Section 2.3.3).

2.3.1. Collision rate in the kinetic theory of gases

The kinetic theory of gases provides an equation for computing the collision rate among multiple species of molecules colliding in a fixed volume V. In particular, the total number of collisions per unit of time and volume of a first species with those of a second one is expressed by (Houston, 2000)

$$C_{R\,1,2} = \pi b^2 v_r \rho_1 \rho_2 \ , \tag{2.9}$$

where v_r is the average magnitude of the relative velocity, ρ_1 and ρ_2 are the densities of molecules of species 1 and 2, and

$$b = r_1 + r_2 \tag{2.10}$$

is the impact parameter, which is the distance below which two object with radii r_1 and r_2 will collide, as depicted in Figure 2-3.

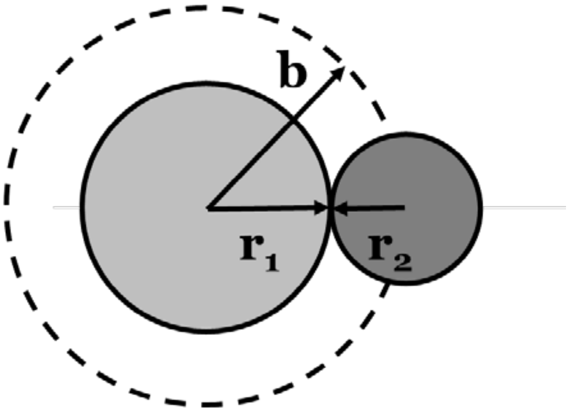

Figure 2-3. A visual representation of the impact parameter: a collision will occur only if the distance is smaller than the impact parameter b equal to the sum of the two radii.

2.3.2. Collision rate in PIB models

The equation (2.9) can also be used for computing the frequency of orbital collisions. Instead of having two molecule species, we have two different species of objects in the space, for example, the intact objects and the debris. The radii are now the equivalent mean objects' radii and can be derived from the object's cross-sectional area A (Rossi *et al.*, 1994) as

$$r = \sqrt{A/\pi} \ . \tag{2.11}$$

Thus, multiplying by the shell volume V, the volume of the considered spherical shell around Earth, the total collision rate per unit of time C_R among species i and j is obtained:

$$C_{R\,i,j} = \pi b^2 v_r \rho_i \rho_j V \ . \tag{2.12}$$

where ρ_i and ρ_j are the densities of objects belonging to species i and j. The average relative speed v_r (in V) can be assumed equal to $\sqrt{2}v_c$, with v_c being the orbital speed at the average population altitude, and equal to about 10 km/s in LEO (Kessler, Reynolds and Anz-Meador, 1989; Talent, 1992; Pardini and Anselmo, 2014). In our problem, the volume is equal to the LEO zone:

$$V = \frac{4}{3}\pi(R_T^3 - R_B^3) \tag{2.13}$$

where R_B and R_T are respectively the bottom and the top radius of the selected spherical LEO shells measured from the centre of the Earth.

In case of a single species or when computing collisions among objects of the same species (in a population with multiple ones), Eq. (2.12) can be rewritten as:

$$C_{R\,i,i} = \frac{1}{2}\pi r_i^2 v_r \rho_i (\rho_i V - 1) . \tag{2.14}$$

The term in brackets corrects the number of pairs of collisions that, for a single species, is equal to $N(N-1)$, with N being the total number of objects of the considered species. A factor of ½ is also introduced in order not to compute each pair of objects twice (Houston, 2000).

Replacing the density in the previous two equations with its definition ($\rho = N/V$), we obtain two expressions with explicit reference to the actual number of objects N_i and N_j:

$$C_{R\,i,j} = \pi b^2 \frac{v_r}{V} N_i N_j \ , \tag{2.15}$$

$$C_{R\,i,i} = \pi r_i^2 \frac{v_r}{V}\frac{1}{2} N_i (N_i - 1) \ , \tag{2.16}$$

where, with a large number of objects, the approximation $N_i(N_i - 1) \simeq N_i^2$ can also be used.

The previous equations can also be expressed via the term

$$p = \pi \frac{v_r}{V}, \tag{2.17}$$

referred to as the intrinsic collision probability per unit of time (Wetherill, 1967). A rough estimate can be obtained for the whole LEO (from 200 to 2,000 km in altitude) assuming a uniform spatial distribution of objects (which is not the case in reality, see Figure 2-14), $v_r = 10$ km/s and $V \approx 10^{12}\,\text{km}^3$, it yields $p \approx 10^{-9}\,\text{m}^{-2}\text{yr}^{-1}$ for the whole LEO . It can also be seen as the collision rate between two bodies for which the sum of the radius is one meter, i.e. $r_1 + r_2 = 1\text{m}$ or, for a single species, $r_1 + r_1 = 1$ m (Rossi and Valsecchi, 2006). Indeed, in more general terms, the number of mutual collision probability per unit of time between two single objects with radius r_1 and r_2, can be expressed as

$$p = \pi \frac{v_r}{V} b^2 = \pi \frac{v_r}{V} (r_i + r_j)^2 \ . \tag{2.18}$$

Therefore, the collision rate can be expressed replacing Eq. (2.18) into Eqs. (2.15) and (2.16):

$$C_{Ri,j} = \frac{p}{(1+\delta_{i,j})} N_i N_j = \frac{p}{(1+\delta_{i,j})} \frac{\rho_i \rho_j}{V}, \tag{2.19}$$

where $\delta_{i,j}$ is a Kronecker's delta, equal to one if both indexes are identical so to have Eqs. (2.15) and (2.16) merged into a single expression.

2.3.3. Collisions in MISSD

At each time step, the model computes a six by six matrix of the collision rates among all object species. Among species i and j it yields:

$$C_{R_{i,j}}(t,h) = p(h)\ f_{i,j}(h)\, b_{i,j} N_i(t,h) \frac{N_j(t,h) - \delta_{i,j}}{2}, \tag{2.20}$$

where $f_{i,j}(h)$ is a corrective factor, $\delta_{i,j}$ is a Kronecker's delta, equal to one if both indexes are identical (N objects can collide only with $N-1$ objects of the same species). For collisions within the same species, having N objects, the number of collision pairs is indeed equal to $N(N-1)/2$, while for different species each term is accounted twice in the $\mathbf{C_R}$ matrix with the $C_{R_{i,j}}$ and $C_{R_{j,i}}$ terms. For example, the mutual collision rate among active spacecraft and collision fragments is equal to $C_{R_{1,5}} + C_{R_{5,1}}$ ($\mathbf{C_R}$ is symmetrical). Therefore, the $1/2$ term is introduced in the Equation (2.20) in order not to count twice the mutual collisions (Houston, 2000).

As mentioned, comparing the movement of orbital objects to the free particle in a gas results in assuming that all the objects can freely move - and therefore collide - in all the available volume. This is not true for the objects in space that are constrained to their orbits, which constitutes only a small portion of all the available space. Therefore, the corrective factor $f_{i,j}(h)$ was implemented to correct the number of collisions to a lower (or equal) compared to the computed one. This factor might be derived from analysis on the objects' orbital eccentricity or, as done in this work, computed empirically assuming initially $f_{i,j}(h)=1$ and then tuning it once collision rates are computed.

The $b_{i,j}$ is the squared sum of the two object radii r_i and r_j,

$$b_{i,j}=(r_i+r_j)^2 \ , \tag{2.21}$$

(sometimes referred to as the square of the impact parameter, see Eq. (2.10), and Figure 2-3), and $p(h)$ is the intrinsic collision probability per unit of time as originally defined in (Wetherill, 1967). It is expressed by

$$p(h)=\pi\frac{v_r(h)}{V(h)} \ , \tag{2.22}$$

where $V(h)$ and $v_r(h)$ are respectively the volume of the altitude shell and the average relative velocity in the same shell. In this case, v_r can be assumed equal to $\sqrt{2}v_c(h)$, with $v_c(h)$ the magnitude of the orbital speed in the middle of the altitude shell h, and equal to about 10 km/s in LEO (Kessler, Reynolds and Anz-Meador, 1989; Talent, 1992; Pardini and Anselmo, 2014). Using Equations (2.21) and (2.22), and neglecting the term $\delta_{i,j}/V$, the collision rate expressed in Equation (2.20) can be rewritten as a function of the shell density ($\rho=N/V$):

$$C_{R_{i,j}}(t,h)=\frac{1}{2}\pi v_r(h)V(h)f_{i,j}(h)b_{i,j}\,\rho_i(t,h)\rho_j(t,h)\,. \tag{2.23}$$

A six by six symmetric $\mathbf{C_R}$ matrix is obtained using Equation (2.23) among each couple of species. Having computed the collision rate, the collision term in Eq. (2.7) indicates the total number of objects involved from collision activities, with objects removed from all species and added only to collision fragments:

$$\dot{\mathbf{C}}(t,h) = -\sum_{j=1}^{6}\begin{bmatrix} C_{R_{1,j}} \\ C_{R_{2,j}}(t,h) \\ C_{R_{3,j}}(t,h) \\ C_{R_{4,j}}(t,h) \\ C_{R_{5,j}}(t,h) \\ C_{R_{6,j}}(t,h) \end{bmatrix} - \begin{bmatrix} C_{R_{1,1}}(t,h) \\ C_{R_{2,2}}(t,h) \\ C_{R_{3,3}}(t,h) \\ C_{R_{4,4}}(t,h) \\ C_{R_{5,5}}(t,h) \\ C_{R_{6,6}}(t,h) \end{bmatrix} + \begin{bmatrix} 0 \\ 0 \\ 0 \\ 0 \\ \sum_{i=1}^{6}\sum_{j=1}^{6} C_{R_{i,j}}(t,h) n_{F_{i,j}}(h) \\ 0 \end{bmatrix}, \qquad (2.24)$$

where $\mathbf{n_F}$ is a six by six matrix of the number of fragments generated in each collision, It is computed a priori using the empirical NASA standard breakup model (Johnson *et al.*, 2001; Krisko, 2011).

In the model, each object is modelled as a points particle with associated physical characteristics. Therefore, three-dimensional representation of forces and momentum during collisions are not considered. As a consequence, it was assumed that all the collisions involved the complete mass of the two objects and took place in their centre of mass (i.e. no appendages such antennas or solar panels are considered). All collisions among payloads and rocket bodies objects were catastrophic and all the others, i.e. intact vs fragments and fragments vs fragment, were damaging ones, with the smaller object being the projectile. Indeed, the collision energy, computed in the centre of momentum reference, for payloads and rocket bodies is likely to exceed the commonly accepted threshold of 40 J/g (Mcknight, Maher and Nagl, 1995), due to their high value of mass. However, having averaged the impact speed equal to $\sqrt{2}v_c(h)$, impacts with low relative velocity were excluded, while conversely these can happen in congested regions were many objects can have similar orbital planes (such as Sun-synchronous orbits). Consequently, the model overestimated the total number of catastrophic collisions in these regions that can, however, be modified by the corrective factor $f_{i,j}(h)$.

The first two terms in Eq. (2.24) refer to the objects removed by collisions at each time step. When a collision between two objects of different species takes place, it removes one object from each population. For a collision within the same species, two objects are removed, with this second additional object accounted by the second term. The third term in Eq. (2.24) refers to the total number of generated collision fragments (at each time step) and contributes only to the fifth row of the collision term, i.e. the fragments are added to the collision fragments species. Rewriting Eq. (2.24) in the species components, it yields

$$\dot{\mathbf{C}}(t,h) = \begin{bmatrix} -\dot{C}_{AP} & -\dot{C}_{AP} & -\dot{C}_{RB} & -\dot{C}_{MR} & +\dot{C}_{CO} & -\dot{C}_{EX} \end{bmatrix}^T . \qquad (2.25)$$

As $\mathbf{C_R}(t,h) \geq 0$, all the collision terms in Eq. (2.8) and (2.25) are always negative (or null) except for $\dot{C}_{CO}$ which includes the fragments generated by collisions among all species.

Lastly, a dimensional analysis yield:

$$\left[\dot{\mathbf{C}}\right]=\left[\mathbf{C_R n_F}(h)\right]=\left[pb\mathbf{N}^2\right]=\left[\frac{1}{\text{year}}\right]. \tag{2.26}$$

In addition, Section 5.2 presents a study on a large synthetic constellation that implemented collision avoidance manoeuvres. Only active payloads, capable of manoeuvring, were allowed to perform collision avoidance, with different percentage of success as a function of the other species, so to represent the different uncertainties linked with the debris identification and orbit determination. For example, spent stages can be more easily tracked than debris, and therefore the resulting manoeuvres were set to have a higher chance of success.

2.3.4. Implementation of the NASA standard break-up model

The number of fragments generated during explosions and collisions is computed via an implementation of the NASA standard break-up model (Johnson *et al.*, 2001; Krisko, 2011). A comparison against a previous study (Krisko, 2011) was performed to test that the number and fragments distribution in breakup events were generated correctly in MISSD.The first scenario reported both catastrophic and damaging collision a projectile of 45 kg which collided with a target of 855 kg (Figure 2-4); while the explosion scenario involved a 1000 kg upper stage (Figure 2-5). In both cases, the implementation is in agreement with the NASA break-up analytical formulation (solid and dashed lines in Figure 2-5 and Figure 2-4, $R^2 > 0.99$), while both differ from the EVOLVE implementation. This latter takes into account a modified law starting from 1 cm in order to take into account the mass distribution in bigger fragments. The more evident example is the remaining “core” of the target object after a non-catastrophic collision. This a single fragment is also the biggest and heaviest one in the non-catastrophic distribution and lies on the x-axis, as depicted in Figure 2-4. Conversely to EVOLVE, the current model does not discretise object in mass classes, and thus it uses the analytical formulation to compute only the number of generated fragments.

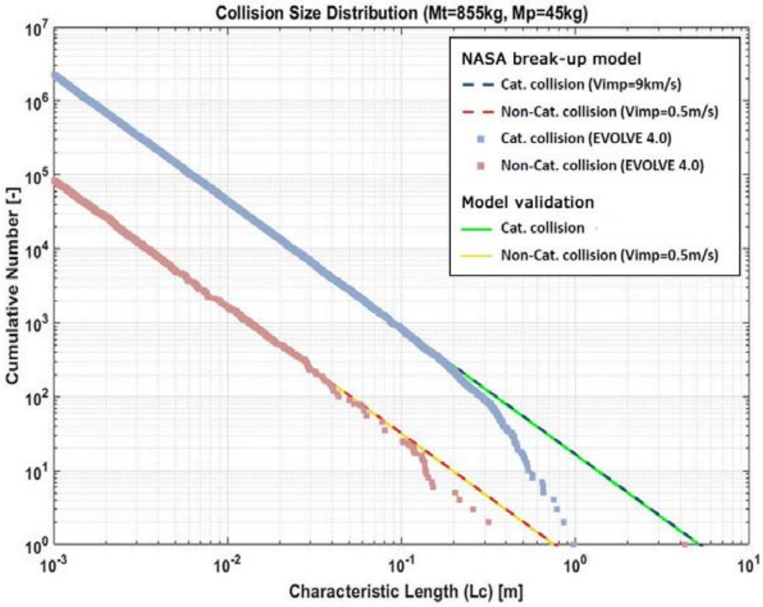

Figure 2-4: Characteristic length vs the cumulative number of fragments produced during both catastrophic and damaging collision in the NASA break-up model (Krisko, Johnson and Opiela, 2001; Krisko, 2011) and in the model implementation.

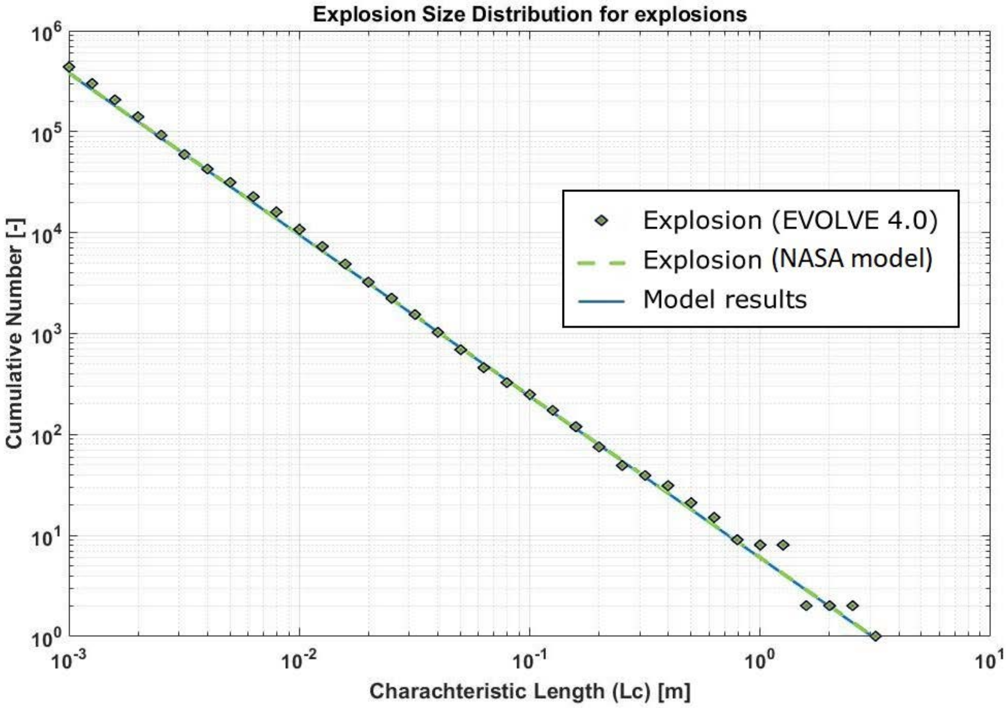

Figure 2-5: Comparison of fragment distribution of a 1000 kg upper stage in the NASA Break-up model with the full power law distribution and the model results.

2.4. Atmospheric model and natural decay

The only natural sink effect modelled is the natural drag. Indeed, the presence of the Earth's atmosphere act on each object in space as a non-conservative force in relation to its cross-sectional area and atmospheric density (with a quadratic relationship). The atmospheric density derives from a piecewise exponential model of the Earth's total atmospheric mass density with an 11-year solar cycle (Committee on Space Research, 1972; King-Hele, 1987; Vallado, 2013). Other variations such as diurnal and seasonal one are not considered. It is also assumed that inactive payloads, rocket bodies and MROs are destroyed by atmospheric re-entry and removed from the simulation within the set amount of time (25 years is the default value).

2.4.1. Atmospheric drag

The atmospheric drag is considered via the decay coefficient

$$\dot{\mathbf{D}}(t) = \begin{bmatrix} 0 & \dot{D}_{IP} & \dot{D}_{RB} & \dot{D}_{MR} & \dot{D}_{CO} & \dot{D}_{EX} \end{bmatrix}^T . \tag{2.27}$$

In the model, the active satellites do not decay ($\dot{D}_{AP} = 0$) as it is assumed that they perform station-keeping manoeuvres, and therefore they remain in the same shell where they were launched. After their operative time, they are moved into the inactive payload species. Two terms constitute each component of the decay rate $\dot{\mathbf{D}}$. The first term refers to the number of objects that decay from the upper altitude shell into the shell of interest, i.e. from $h+1$ to h, while the second term indicates objects decaying from the current into the lower altitude shell, i.e. from h to $h-1$ (Cordelli *et al.*, 1993; Rossi *et al.*, 1994; Somma, Colombo and Lewis, 2017). For each component of Eq. (2.27), it yields:

$$\dot{\mathbf{D}}(t,h) = +\frac{\mathbf{N}(t,h+1)}{\tau(h+1)} - \frac{\mathbf{N}(t,h)}{\tau(h)} , \tag{2.28}$$

where, $\boldsymbol{\tau}$ is the characteristic residence time, which is stored in a look-up table to reduce the simulation's execution time.

2.4.2. Residence time

The residence time represents the time required for an object to decay from the upper to the lower boundary of each altitude shell. For computing it, an expression for the loss in the altitude as a function of the ballistic coefficient was derived. The change of semi-major axis a due to drag as a function of time t can be approximated to the first order under the assumptions that its derivative da/dt is small over one orbit (King-Hele, 1987):

$$\frac{da}{dt} \approx -\left(\frac{c_D A}{m}\right)\zeta\sqrt{\mu_E a}\ , \tag{2.29}$$

where c_D is the drag coefficient, A and m are respectively the object cross-section area and its mass, μ_E is the Earth's gravitational parameter, and ς is the atmospheric density at the corresponding semi-major axis. The same result is obtained from (Vallado, 2013) that enunciates the general case:

$$\frac{da}{dt} = -\left(\frac{c_D A}{m}\right)\varsigma v_r^2\,\frac{\sqrt{1+e^2+2e\cos(\nu)}}{\eta\sqrt{(1-e^2)}}\ , \tag{2.30}$$

where v_r is the relative speed, e the orbit eccentricity, ν the true anomaly and η the mean motion. Assuming circular orbits ($e = 0$) and a non-rotating atmosphere, the velocity term simplify to the circular orbital speed: $v_r = \sqrt{\mu_E / a}$. Replacing these values, and the expression for the mean motion ($\eta = \sqrt{\mu_E / a^3}$) into Eq. (2.30), leads back to Eq. (2.29).

Manipulating Eq. (2.29) and rewriting the semi-major axis explicitly as the sum of Earth radius R_E and object altitude z (under the assumption of circular orbits), the time needed to decay from an initial height z_0 to a final one z_f (with $z_0 > z(t) > z_f$) can be expressed as:

$$\int_0^t dt = \int_{z_0}^{z_f} \frac{dz}{-c_D \frac{A}{m}\varsigma\sqrt{\mu_E(z+R_E)}}\ . \tag{2.31}$$

Replacing in (2.31) the ballistic coefficient, defined as

$$\mathbf{B}(h) = c_D\frac{A}{m}\ , \tag{2.32}$$

with the assumption of a flat plate model (equal for all the species) that gives $c_D = 2.2$ (Vallado, 2013, pp. 551), and taking it out of the integral, (it is not dependent on the density nor the object altitude), it yields:

$$\int_0^t dt = -\frac{1}{B}\int_{z_0}^{z_f} \frac{dz}{\varsigma\sqrt{\mu_E(z+R_E)}}\ , \tag{2.33}$$

which could be rewritten as the residence time

$$\boldsymbol{\tau}(h) = -\frac{1}{\mu_E B}\int_{z_0}^{z_f} \frac{dz}{\varsigma(z)\sqrt{(z+R_E)}}\ . \tag{2.34}$$

Using a numerical integrator for each species and within each altitude shell, and converting the results from seconds to years, the required residential times are obtained and stored in a look-up table. Concerning the generic N/τ term presented twice in Eq. (2.28), a dimensional analysis yields

$$\left[\dot{D}\right]=\left[\frac{N}{\tau}\right]=\left[\frac{\mathrm{m}^0}{\mathrm{kg}^0}\frac{1}{\mathrm{year}}\right]=\left[\frac{1}{\mathrm{year}}\right], \tag{2.35}$$

and thus, as expected, it represents the number of objects decayed per year due to drag.

2.4.3. Density profile and solar cycle

Variation in atmospheric density due to the 11-yr solar cycle are considered with the inclusion of a yearly averaged exospheric temperature (i.e. the asymptotic value of the temperature reached in the higher altitude of exosphere) equal to

$$T_{exo}(t)=1.125(379+3.24F_{10.7}(t))+59.89\,, \tag{2.36}$$

where the $F_{10.7}$ is the solar flux index (Lewis *et al.*, 2011). The last term in Eq. (2.36) represents the long-term average impact of geomagnetic effects on the exospheric temperature and derives from an average of historical values of the planetary geomagnetic index.

Values of the $F_{10.7}$ solar flux index for a mean solar cycle were computed from 44 years of historical data (1973-2016, cycle 20 to 24) (Government of Canada and Natural Resources Canada, 2017). Replacing this latter into Eq. (2.36), monthly and yearly averaged exospheric temperature were then obtained (Figure 2-6).

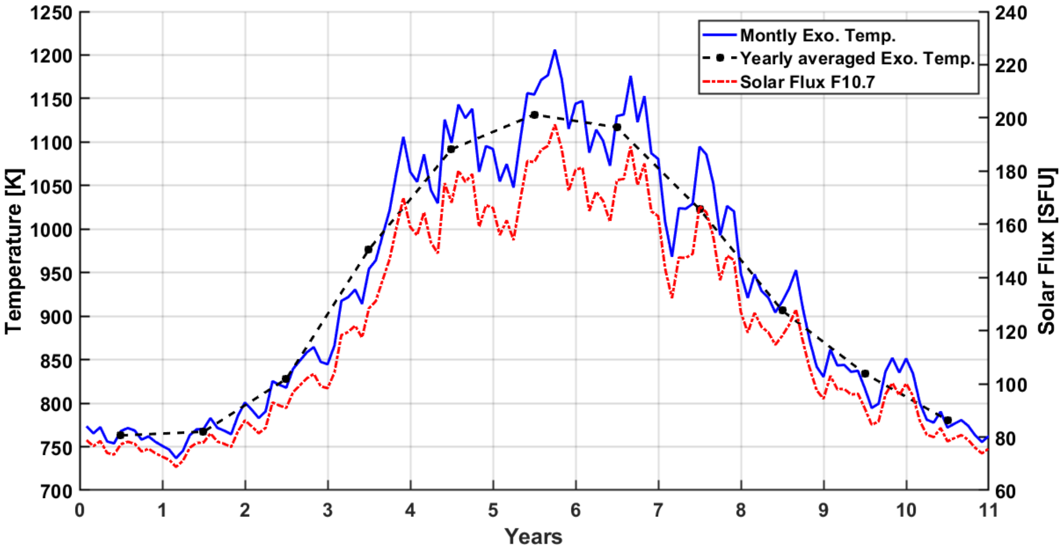

Figure 2-6. The considered 11-years variation of the solar flux, monthly and yearly averaged exospheric temperature. The solar flux is given in solar flux units (SFU) $1\ \mathrm{SFU}=10^{-22}\,\mathrm{m}^{-2}\mathrm{Hz}^{-1}$.

The residence time of each shell was obtained via numerical integration of Eq. (2.34) with an atmospheric density profile from 200 to 2,000 km. The density profile derives from the CIRA-72 (Committee on Space Research International Reference Atmosphere) model with an adjustment in the atmospheric density ς so to have a piecewise-continuous formulation (Committee on Space Research, 1972; Vallado, 2013) with a single value for all latitude and a mean solar activity. It follows:

$$\varsigma(z,T_{exo}) = \varsigma_0(z_0,T_{exo})\exp\left(-\frac{z-z_0}{Z(z_0,T_{exo})}\right), \tag{2.37}$$

where $\varsigma_0(h_0,T_{exo})$ is the atmospheric density at reference altitude z_0, z the altitude and $Z(z_0,T_{exo})$ the scale height. A linear interpolation was used to extract estimates of the exospheric temperature from look-up tables which ranged from 600 to 2,200 Kelvin in temperature and from 110 to 2,000 km in the perigee altitude.

In the few cases in which the solar cycle was not used, the Eq. (2.37) was used without the dependency on the exospheric temperature, computing the density using the base altitude, nominal density, and scale height listed in Table 2-1. Above 1,000 km the density followed a single exponential law with a reference height of 1,000 km. Although a straightforward approach (and thus very fast in execution), this simplified method was reported to produce moderate results for general studies (Vallado, 2013), with no significant differences compared to other models (e.g. less than 1% error on the daily average of the 3-hours geomagnetic index (Saunders, 2012)). A comparison of the model results obtained in MISSD with and without the solar cycle (and against DAMAGE) are presented in Section 3.2.1.

Table 2-1. Values used in the piecewise exponential model of the atmosphere (Vallado, 2013).

Altitude [km]	**Base altitude [km]**	**Nominal density [kg/m3]**	**Scale height [km]**
200-250	200	2.789 10^{-10}	37.105
250-300	250	7.248 10^{-11}	45.546
300-350	300	2.418 10^{-11}	53.628
350-400	350	9.518 10^{-12}	53.298
400-450	400	3.725 10^{-12}	58.515
450-500	450	1.585 10^{-12}	60.828
500-600	500	6.967 10^{-13}	63.822
600-700	600	1.454 10^{-13}	71.835
700-800	700	3.614 10^{-14}	88.667
800-900	800	1.170 10^{-14}	124.640
900-1,000	900	5.245 10^{-15}	181.050
>1,000	1,000	3.019 10^{-15}	268.000

Qualitative comparison of the density profile without the solar cycle was carried out to verify the correct implementation of the atmospheric model. The first comparison was against the MSIS-E90 model (Figure 2-7) (Hoedin, 1987; Vallado, 2013). The two models showed similar density profile, but over 400 km the difference rose up to 43.8%, resulting in different decay times at higher altitudes. These differenced were due to the different type of model used, with the atmospheric model implemented in MISSD not accounting for seasonal and diurnal variations, Earth oblateness, and relative wind.

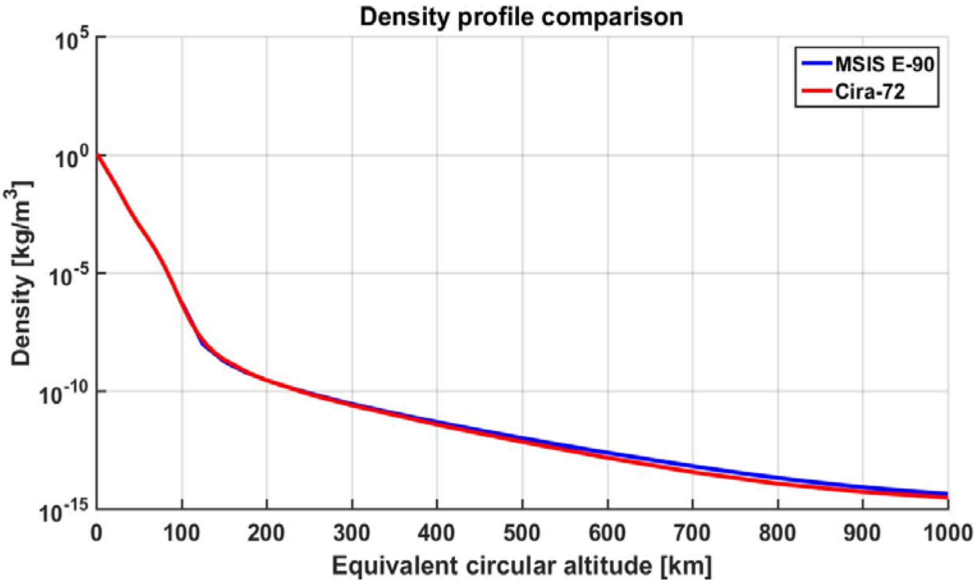

Figure 2-7: Density comparison of the atmospheric models MSIS E-90 and CIRA-72 from 100 to 1,000 km of altitude. MSIS E-90 is computed at 12:00 01/06/2000, null latitude and longitude, daily F10.7=140, 3-month average F10.7=140, daily Ap=15.

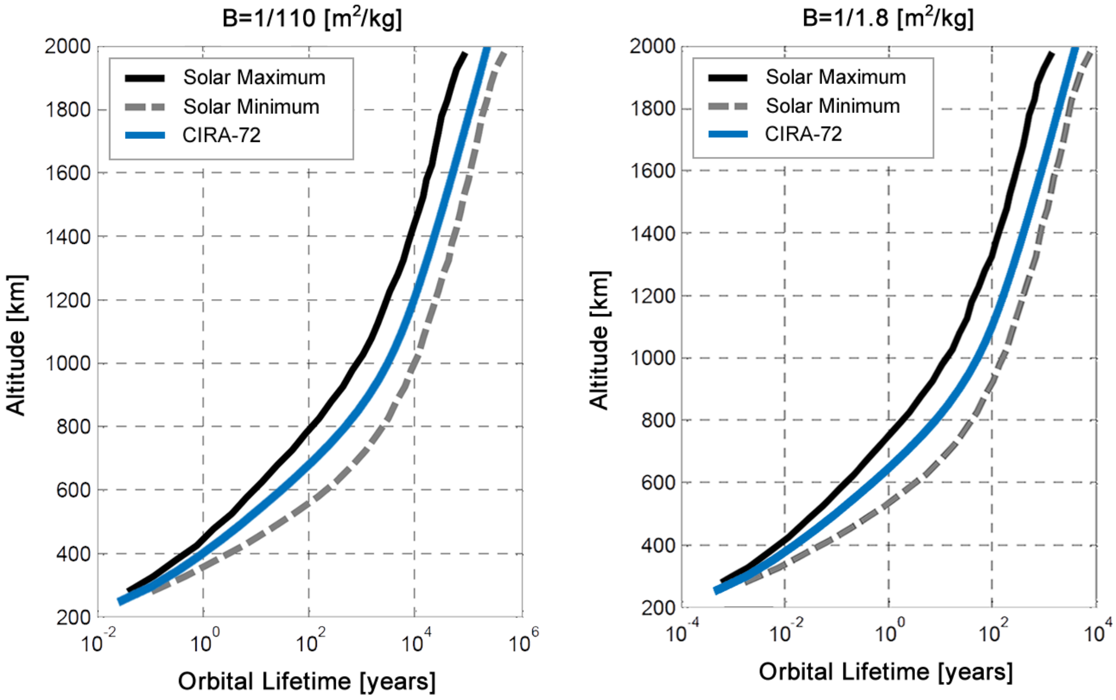

Figure 2-8: Density profile comparison with maximum and minimum solar activity from (Lafleur, 2011) and the CIRA-72 model for two values of the ballistic coefficient.

A second comparison has been carried out on the orbital lifetime against an implementation of the MSIS-86 model (Lafleur, 2011), which includes the solar activity (Hoedin, 1987; Larson and Wertz, 1999). Numerical values were not available, and therefore, only qualitative analysis was possible. The density profile used in MISSD produced orbital lifetimes that lied between those obtained with the maximum and minimum solar activity (Figure 2-8).

2.5. Explosions

A six-component term expresses the explosion rate:

$$\dot{\mathbf{E}}(t) = \left[-\dot{E}_{AP} \quad -\dot{E}_{IP} \quad -\dot{E}_{RB} \quad -\dot{E}_{MRO} \quad -\dot{E}_{CO} \quad \dot{E}_{EX} \right]^T . \tag{2.38}$$

It was assumed that MROs objects and fragments would lack components prone to explode (e.g. batteries or propellant tanks), leading to $\dot{E}_{MR} = 0$ and $\dot{E}_{CO} = 0$. In addition, even if currently some active satellite experienced breakups events, (due mainly to battery failure), it was assumed that, in the long-term, the rate of these events would decrease in number due to an increase in experience and design reliability and their influence would be minimal in future. Therefore, the model accounts only for inactive payloads and rocket bodies as a source of explosion fragments, yielding:

$$\dot{\mathbf{E}}(t) = \left[0 \quad -\dot{E}_{IP} \quad -\dot{E}_{RB} \quad 0 \quad 0 \quad \dot{E}_{EX} \right]^T , \tag{2.39}$$

where $\dot{E}_{IP}$ and $\dot{E}_{RB}$ are respectively the annual explosion rate of inactive payloads and rocket bodies. While $\dot{E}_{IP}$ and $\dot{E}_{RB}$ account for objects that are removed from the environment due to explosions (each explosion involve one single object), the last component $\dot{E}_{EX} \geq 0$ represents the fragments generated during those collisions, and is expressed by

$$\dot{E}_{EX} = \dot{E}_{IP} n_{E,IP} + \dot{E}_{RB} n_{E,RB} , \tag{2.40}$$

with $n_{E,IP}$ and $n_{E,RB}$ indicating the number of objects generated during each explosion involving respectively inactive payloads and rocket bodies. The value of the generic n_E term is computed a priori using the NASA standard break-up model (Johnson *et al.*, 2001; Krisko, 2011):

$$n_E(L_C) = 6 S L_C^{-1.6} , \tag{2.41}$$

where the minimum size of fragments L_C is equal to 0.1 m and S is a species-dependent unit-less scaling factor. Finally, replacing Eq. (2.40) into the Eq. (2.39), yields

$$\dot{\mathbf{E}}(t) = \left[0 \quad -\dot{E}_{IP} \quad -\dot{E}_{RB} \quad 0 \quad 0 \quad \dot{E}_{IP} n_{E,IP} + \dot{E}_{RB} n_{E,RB} \right]^T \tag{2.42}$$

2.6. Launches

New objects are injected into different altitude shells via the launch term in Eq. (2.7). Based on the selected launch profile (stored in an external text file) new active payloads, rocket bodies and MROs are added at every time step as a function both of altitude shell and time (see Eq. (2.8)), yielding

$$\dot{\mathbf{L}}(t,h) = \begin{bmatrix} \dot{L}_{AP} & 0 & \dot{L}_{RB} & \dot{L}_{MR} & 0 & 0 \end{bmatrix}^T . \tag{2.43}$$

Indeed, inactive payloads, collision and explosion fragments are not produced and injected in the environment during launches. The default value for the launch rate and profile is reported in Section 2.11.

2.7. Post-mission disposal

Post-mission disposal is implemented assuming that inactive satellites remained in the same shell in which they were launched for a time equal to the set residual lifetime and are then removed accordingly with the PMD compliance level (from 0% to 100%). However, this simplification has the drawback of overestimating the number of inactive objects that remain for a more extended period in the original launch shell instead of being manoeuvred into elliptic orbits or decaying in lower ones, varying therefore the collision rates in these shells. An alternative approach which includes re-orbiting manoeuvres was also implemented and is presented in Section 5.2.

The post-mission disposal is implemented with

$$\dot{\mathbf{M}}(t_{PMD},h) = -\boldsymbol{\lambda} \circ \dot{\mathbf{L}}(t,h) , \tag{2.44}$$

where $\circ$ is the Hadamard product (i.e. $(\mathbf{A} \circ \mathbf{B})_{i,j} = A_{i,j} \cdot B_{i,j}$), $\boldsymbol{\lambda} \in [0;1]$ is the percentage level of compliance with the guidelines and t_{PMD} is a future time, corresponding to when the objects (launched at the time t) will be removed from the simulation. Therefore, Eq. (2.44) indicates that after a selected amount of time, a percentage of the launched objects will be subject to PMD.

The future time t_{PMD}, which is expressed in years, is equal to

$$t_{PMD} = t + \Delta t_{SRL} + \Delta t_{SOL} , \tag{2.45}$$

where t is the current time, Δt_{SOL} the species operative life, and Δt_{SRL} the residual lifetime established by the mitigation guideline (and equal to 25 years by default; Figure 2-9).

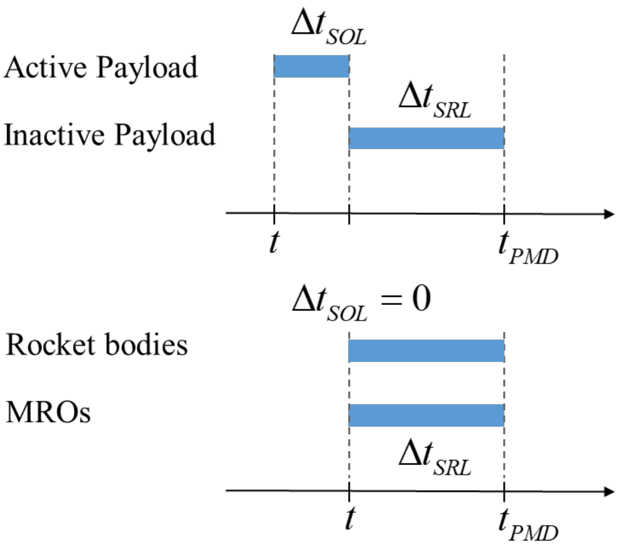

Figure 2-9. Visual representation of t_{PMD}: Δt_{SOL} after being launched, an active payload become inactive, and after an additional Δt_{SRL} this is removed from the environment. Rocket bodies and MROs instead have a null operative life.

$\dot{M}$ is equal to zero for collision and explosion fragments, (since they are not controllable), and always negative for rocket bodies and MROs. Indeed, rewriting Eq. (2.44), yields:

$$\dot{\mathbf{M}}(t_{PMD},h) = \left[\dot{M}_{AP} \quad \dot{M}_{IP} \quad \dot{M}_{RB} \quad \dot{M}_{MR} \quad 0 \quad 0\right], \tag{2.46}$$

with

$$\dot{M}_{RB}(t+\Delta t_{SRL},h) \quad = -\lambda_{RB}\dot{L}_{RB}(t,h), \tag{2.47}$$

$$\dot{M}_{MR}(t+\Delta t_{SRL},h) \quad = -\lambda_{MR}\dot{L}_{MR}(t,h). \tag{2.48}$$

The operative lifetime of rocket bodies (i.e. upper stages) and MROs is null, as they terminate their mission just after their launch, and they are removed from the environment after Δt_{SRL} years (Figure 2-9). Active payloads (launched at the time t) are instead moved to the inactive payload species after their operative life:

$$\dot{M}_{AP}(t+\Delta t_{SOL},h) = -\lambda_{AP}\dot{L}_{AP}(t,h) \ . \tag{2.49}$$

For inactive payloads, two terms are considered:

$$\begin{cases} \dot{M}_{IP}(t+\Delta t_{SOL},h) & = +\lambda_{ip}\dot{L}_{ip}(t,h) \\ \dot{M}_{IP}(t+\Delta t_{SRL}+\Delta t_{SOL},h) & = -\lambda_{ip}\dot{L}_{ip}(t,h) \end{cases}, \tag{2.50}$$

where the first represents the spacecraft that become inactive (and indeed is equal in absolute value to $\dot{M}_{AP}$), while the second defines the time after which these defunct payloads are finally removed from the simulation (Figure 2-9).

At last, a simple dimensional analysis provides, as expected, that $\dot{M}$ is inversely proportional to time, as it represents the number of objects removed per year:

$$\left[\dot{\mathbf{M}}\right]=\left[\boldsymbol{\lambda}\,\dot{\mathbf{L}}\right]=\left[\frac{1}{yr}\right]. \tag{2.51}$$

Known limitations of this method are the assumptions of all objects having circular orbits and the incapability of the spacecraft to perform end-of-life manoeuvres that re-orbit objects into other shells. Indeed, the formulation presented in Eq.(2.44) does not move objects into a lower shell (or re-orbit above LEO) and does not let them decay due to drag, but instead keeps the objects in the same shell and then removes them after a specific time based on the Eq. (2.45).

For investigating the impact of these assumptions, the residence times of the objects in each shell were computed using the semi-major axis and eccentricity of each object in the initial population and launch profile. Results showed, as expected, differences in the objects spatial distribution. However, they were not sufficient to affect the conclusions drawn from the performed studies. In addition, to improve the model for future studies, it was recently implemented (Section 5.2) the option to reposition of payloads and rocket bodies at the end of their operative life (8 yr for satellites and just after launch for rockets) in lower orbits with the selected residual time (25 years by default).

2.8. The adaptive controller

A feedback controller simulates the application of remediation practices adjusting the active debris removal rate. The basic idea is to evaluate at every timestep one or more parameters linked with the current population and adopt a user-selected strategy (Figure 2-2). The model can use different control laws based on the selected control strategy; for example, active removals can specifically target inactive payload or rocket bodies as a function of the shells' orbital densities.

Several control laws were developed and tested over time. Section 2.8.1 presents the first one: a simple proportional control law on the total density, while Section 2.8.2 illustrates a linear control which takes into account the partial population densities. The latest addition to the model was a more complex quadratic control law with three control gains and is reported in Section 2.8.3. While the linear control law was the first to be developed and acted as a testbed for the method, the other laws were built so to have the same quadratic dependence on the spatial density that is present in the collision rate formula.

The choice to investigate the spatial density instead of the orbital population (with which is linked by the volume) was driven by the fact that, in the model, the orbital collision rate has a quadratic dependence on the spatial density. In addition, the same density is equivalent to the same collision risk independently from the volume, while the same number of objects in a bigger volume had a lower density and a lower collision probability. Having multiple evenly spaced altitude shells, MISSD has a different volume for each shell and therefore is more convenient to use the density to act consistently in different regions against the same collision risk thresholds.

Moreover, even if the total number of debris is an important metric of the health of the space environment, more relevant is the collision risk that they pose. Therefore, the spatial densities could give better indications on the current and future health of each region in space. Indeed, the peaks in the density reflect the higher collision probabilities and thus collision fragments, which are likely to be the predominant species in LEO between 50 and 100 years in the future.

However, the total population or total density gives a single overall information, and the same level of importance is given to all the species of objects, while in reality, this is not true. Indeed, active payloads should be allowed to grow, while not the same could be said for fragments or inactive spacecraft. Therefore, two of the three versions of the control law (i.e. the linear and the quadratic one) had a differential action based both on the total and partial densities in each shell, reflecting and reacting both to the global health of the environment, i.e. to the total density, and to the key species that are likely to cause the major number of fragments, i.e. to the partial densities of inactive payloads and rocket bodies.

The controller enforces the active removal of objects instantaneously, taking out the selected number of objects from the simulations at the end of each time step. In reality, a time delay would be present between the measure of the population, the selection of the target and its removal. For example, if it takes five years to implement an ADR mission, based on a measurement of the current population, then it may not be a sufficient interval by the time it reaches orbit – or it might not be needed at all. Moreover, depending on how the time delay is modelled, different number of removals can be obtained for the same situation

MISSD do not produce a priority list of the most dangerous objects to be removed, with every object removed affects the collision probability of an equal amount. In reality some objects are more dangerous than others due to their mass (i.e. number of generated fragments), cross-sectional area and object flux in the object’s region (collision probability). These objects are relatively rare and possess each different level of risk; therefore, once the top ones in the priority list are removed, there is a rapidly diminishing effect on the effectiveness.

2.8.1. Proportional control law on the total population

Proportional controllers are a form of control loop feedback mechanisms widely used in control systems, where the controller observes an output value from a system and compares it to a specific set point . The obtained error is then used to compute a control that is passed to an actuator interfaced with the system.

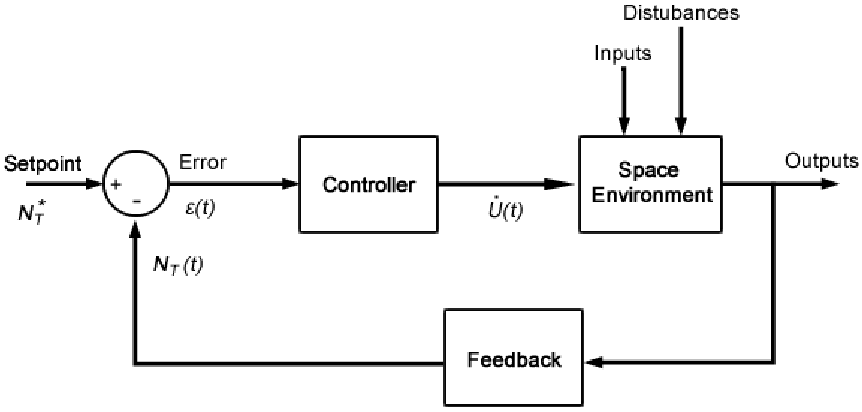

Figure 2-10. Schematic of the proportional feedback controller.

In the MISSD model, the system is the space environment, and the outputs are the populations of the six species of objects (Figure 2-10). The error $\varepsilon(t)$ is expressed as the difference between the current population $N_T(t)$ and the user-selected setpoint N_T^* (representing a population target), with

$$\varepsilon(t) = N_T(t) - N_T^* . \tag{2.52}$$

Having a fixed volume, Eq. (2.52) can be rewritten in terms of the orbital density $\rho = N/V$:

$$\varepsilon(t) = (\rho_T(t) - \rho_T^*)V , \tag{2.53}$$

where $\rho^* = N^*/V$ is the target orbital density.

The controller output $\dot{U}(t)$ defines how many objects are actively removed at each time, and it is defined as

$$\begin{cases} \dot{U}(t) = 0 & with \;\; \varepsilon(t) \le 0 \\ \dot{U}(t) = \dfrac{u_{\max}}{\varepsilon_{\max}} \varepsilon(t) & with \;\; 0 < \varepsilon(t) < \varepsilon_{\max} \\ \dot{U}(t) = u_{\max} & with \;\; \varepsilon(t) \ge \varepsilon_{\max} \end{cases} \tag{2.54}$$

with $\varepsilon_{\max}$ the maximum error possible above which the maximum control $u_{\max}$ is used (i.e. the maximum number or removal is reached), and. the controller is saturated (Figure 2-11).

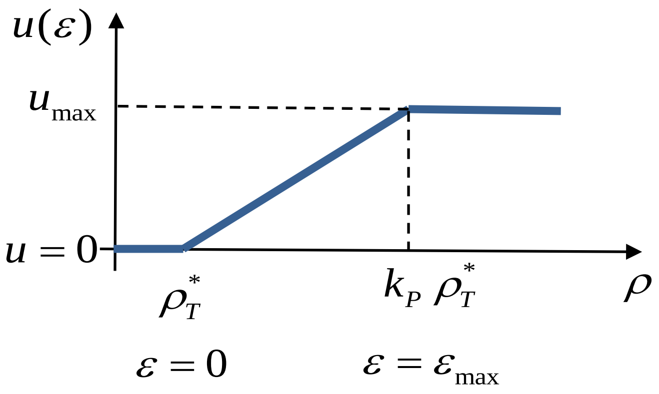

Figure 2-11. Visual representation of the proportional control law.

The maximum error is expressed either by

$$\varepsilon_{\max}=k_p N_T^*\,, \tag{2.55}$$

or

$$\varepsilon_{\max}=k_p \rho_T^*\,V\,, \tag{2.56}$$

where $k_P>1$ is a multiplier of the population set point, which marks the upper boundary of the unsaturated proportional controller.

When the controller is active and not saturated, the number of removals is therefore proportional to the error $\varepsilon(t)$, with a gain equal to $u_{\max}/\varepsilon_{\max}$. Replacing Eq. (2.52) in (2.54) yields

$$\begin{cases} \dot{U}(t)=0 & with\ \ \rho_T(t)\le\rho_T^* \\ \dot{U}(t)=\dfrac{u_{\max}}{k_p\,\rho_T^*V}\varepsilon(t) & with\ \ \rho_T^*<\rho_T(t)<k_p\rho_T^*u \\ \dot{U}(t)=u_{\max} & with\ \ \rho_T(t)\ge k_p\rho_T^* \end{cases}\,. \tag{2.57}$$

Note that the lowercase u is used here and in the following paragraph for denoting the annual active removal limits, while uppercase $\dot{\mathrm{U}}(t)$ is used for the actual removal rate generated by the controller.

This simple proportional law is used to determine a removal rate from a minimum value of zero with a linear law up to the selected maximum value (Figure 2-11). This ensures that the number of removals per year can be modelled with a realistic limit. Without this limit, the controller would have the possibility to reach unrealistic (and limitless) high values for annual removals in order to achieve its objective.

2.8.2. Linear control law on the partial population densities

Another control law was developed as a function of the orbital densities $\rho(t,h)$ and the populations of rocket bodies and inactive payloads. For each time and shell, the controller computes a value for the number of objects to be removed with

$$\begin{cases} \dot{\mathbf{U}}_{\mathbf{IP}}(t,h)=0 \\ \dot{\mathbf{U}}_{\mathbf{RB}}(t,h)=0 \end{cases} \qquad \text{with} \quad \rho_T(t,h)<\rho_{\min}$$

$$\begin{cases} \dot{\mathbf{U}}_{\mathbf{IP}}(t,h)=u_{IP}\dfrac{\rho_{IP}(t,h)}{\rho_{IP}(t,h)+\rho_{RB}(t,h)}\dfrac{\rho_T(t,h)}{\rho_{max}} \\ \dot{\mathbf{U}}_{\mathbf{RB}}(t,h)=u_{RB}\dfrac{\rho_{RB}(t,h)}{\rho_{IP}(t,h)+\rho_{RB}(t,h)}\dfrac{\rho_T(t,h)}{\rho_{max}} \end{cases} \qquad \text{with} \quad \rho_{\min}\le\rho_T(t,h)\le\rho_{\max}\ , \tag{2.58}$$

$$\begin{cases} \dot{\mathbf{U}}_{\mathbf{IP}}(t,h)=u_{IP}\dfrac{\rho_{IP}(t,h)}{\rho_{IP}(t,h)+\rho_{RB}(t,h)} \\ \dot{\mathbf{U}}_{\mathbf{RB}}(t,h)=u_{RB}\dfrac{\rho_{RB}(t,h)}{\rho_{IP}(t,h)+\rho_{RB}(t,h)} \end{cases} \qquad \text{with} \quad \rho_T(t,h)>\rho_{\max}$$

where u is the maximum yearly removal rate, and subscript IP and RB refers to inactive payloads and rocket bodies, respectively. Similarly, to the proportional controller (Section 2.8.1), a minimum and a maximum threshold were set. However, this time the boundaries are on the total density, i.e. the density of all the object species, in a shell volume. If the total density in a shell is below the minimum threshold, the control is null, with the rationale of giving priorities to other, more congested shells, which have therefore a higher collision risk. In case there are no inactive payloads or rocket bodies in a specific shell, the control law in Eq. (2.58) also ensures that no active removals are performed on that specific shell and species.

The controller automatically manages how to split the number of removals among all the altitude shells proportionally to each shell total density $\rho(t,h)$ and within the shells between inactive payloads and rocket bodies with the partial densities ratio and the fixed u_{IP} and u_{RB} upper limits. When the control is active, the sum of the two control terms over all the shells are normalised not to exceed the set maximum annual removal rate defined by

$$u=u_{IP}+u_{RB}\ . \tag{2.59}$$

2.8.3. Quadratic control law on the partial population densities

A quadratic control law was defined as a particular case of an n-grade control law (Eq. (2.60)). When the controller is active, i.e. after a set start year for ADR and when above the minimum threshold, it automatically computes three gain coefficients, $\mathbf{k}_{\boldsymbol{\rho}}(t,h)$, $\mathbf{k}_{\mathbf{IP}}(t,h)$, and $\mathbf{k}_{\mathbf{RB}}(t,h)$, which can assume any values between 0 and 1.

The first gain, $\mathbf{k}_{\boldsymbol{\rho}}$, is related to the spatial density and regulates how many removals should be assigned at each shell based on their total density (i.e. the density of all the object species). Minimum and maximum thresholds for the total density were set in each shell to bound the controller gain. When the total density in a shell is below the minimum threshold, the gain is set to zero, while above the maximum threshold, it is equal to one (i.e. the control gain is saturated). For intermediate values of the density, k_ρ is a continuous function of the density (Figure 2-12):

$$\begin{cases} \mathbf{k}_{\boldsymbol{\rho}}(t,h) = 0 & \text{with} \quad \boldsymbol{\rho}(t,h) < \rho_{\min} \\ \mathbf{k}_{\boldsymbol{\rho}}(t,h) = \left(\dfrac{\rho(t,h) - \rho_{\min}}{\rho_{\max} - \rho_{\min}} \right)^{k_q} & \text{with} \quad \rho_{\min} \le \boldsymbol{\rho}(t,h) \le \rho_{\max} \\ \mathbf{k}_{\boldsymbol{\rho}}(t,h) = 1 & \text{with} \quad \boldsymbol{\rho}(t,h) > \rho_{\max} \end{cases}, \tag{2.60}$$

where $k_q = 2$ was used to have a quadratic dependence on the density like in the equation used to compute the collision rate (both in MISSD and in other models as well , e.g. (Farinella and Cordelli, 1991; Talent, 1992; Rossi *et al.*, 1994; Anselmo, Rossi and Pardini, 1999; Ariyoshi and Hanada, 2009)).

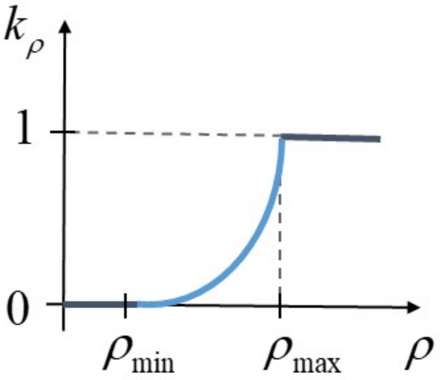

Figure 2-12. Graphical representation of the k_ρ gain in the quadratic control law.

The other two gains, $\mathbf{k}_{\mathbf{IP}}$ and $\mathbf{k}_{\mathbf{RB}}$, adjust the removal rate in each shell based on the ratio of inactive payloads and rocket bodies densities (i.e. their relative partial shell densities):

$$\begin{cases} \mathbf{k}_{\mathbf{IP}}(t,h) = \dfrac{\boldsymbol{\rho}_{\mathbf{IP}}(t,h)}{\boldsymbol{\rho}_{\mathbf{IP}}(t,h) + \boldsymbol{\rho}_{\mathbf{RB}}(t,h)} \\ \mathbf{k}_{\mathbf{RB}}(t,h) = \dfrac{\boldsymbol{\rho}_{\mathbf{RB}}(t,h)}{\boldsymbol{\rho}_{\mathbf{IP}}(t,h) + \boldsymbol{\rho}_{\mathbf{RB}}(t,h)} \end{cases}, \tag{2.61}$$

where the subscripts IP and RB refers to inactive payloads and rocket bodies, respectively. Multiplying both the numerator and denominator by the shell volumes, the same formula can be expressed with the partial populations.

Once the three gains are computed for each shell, the controller normalises them and defines the removal rates in each shell with

$$\begin{cases} \dot{\mathbf{U}}_{\mathbf{IP}}(t,h) = \dfrac{\mathbf{k}_{\boldsymbol{\rho}}(t,h)\mathbf{k}_{\mathbf{IP}}(t,h)}{\sum\limits_{h}\left[\mathbf{k}_{\boldsymbol{\rho}}(t,h)\mathbf{k}_{\mathbf{IP}}(t,h)\right]} u_{IP} \\ \dot{\mathbf{U}}_{\mathbf{RB}}(t,h) = \dfrac{\mathbf{k}_{\boldsymbol{\rho}}(t,h)\mathbf{k}_{\mathbf{RB}}(t,h)}{\sum\limits_{h}\left[\mathbf{k}_{\boldsymbol{\rho}}(t,h)\mathbf{k}_{\mathbf{RB}}(t,h)\right]} u_{RB} \end{cases}, \tag{2.62}$$

where u_{IP} and u_{RB} are the inactive payload and rocket body annual removal rates defined at the beginning of each simulation. This normalisation ensures that the set annual removal rates are performed at each time step in which the controller is active without exceeding the maximum number of allowed annual removals (i.e. $u = u_{IP} + u_{RB}$).

To summarise, the controller splits the selected inactive payloads and rocket bodies annual removal rates (u_{IP} and u_{RB}) among and within the altitude shells as a function of the square of the shells' total densities (via $\mathbf{k}_{\boldsymbol{\rho}}$, Eq. (2.60)) and local partial densities (via $\mathbf{k}_{\mathbf{IP}}$ and $\mathbf{k}_{\mathbf{RB}}$, Eq. (2.61)).

2.9. Effectiveness index

The reduction of the population per object removed can be quantified via the Effective Reduction Factor (ERF) that measures then the reduction of the population per object removed (Liou and Johnson, 2009):

$$ERF(t) = \frac{N^{*}(t) - N(t)}{u_{cum}(t)}, \tag{2.63}$$

where $N^{*}(t)$ is a reference population obtained with no removals, and $u_{cum}(t)$ is the number of cumulative removals. Some space debris models rank the objects to be removed based on a risk index that derives for example from the mass, the collision probability, or the product of more entities (such the collision probability and the number of generated fragments). Once the most dangerous objects (i.e. those with the highest index) are removed, each additional removal has a lower impact on the environment (Liou and Johnson, 2009; White and Lewis, 2014b). Following this reasoning, it appears that not all objects removed contribute in the same way to the lowering of the future collision risk, with the initial removals being the most effective (i.e. have the highest ERF). However, aiming for a high efficiency might not be enough to reach a specific target level on the future orbital population, which instead decreases when more objects are removed, and corresponds to lower ERF values. For addressing this issue, a Normalised Effective Reduction Factor (NERF) was defined in (Lewis *et al.*, 2009a; Lewis, White and Stokes, 2012). Some of the analysis presented in this thesis uses the NERF performance index to numerically compare the effectiveness of each strategy (i.e. the different practices applied) against a worst- and best-case scenario.

The NERF is defined as

$$NERF(t) = \frac{N_{worst}(t) - N(t)}{N_{worst}(t) - N_{best}(t)} \ , \tag{2.64}$$

where N_{worst} indicates the population in a reference worst-case scenario with 0% PMD compliance and no objects actively removed, and N_{best} is an ideal reference best-case scenario, e.g. with 100% compliance and no collisions. The introduction of this normalised and dimensionless performance index allows a more straightforward comparison among scenarios with different conditions (e.g. varying the removal rates or the mitigation compliance levels) against a reference best-case (with NERF=1) and worst-case (with NERF=0). In some cases (e.g. for a high number of removals), the population $N(t)$ can be null or lower than the reference best-case (i.e. $N(t) \le N_{best}$), producing effectiveness bigger than 1. In any case, the NERF is bounded by

$$0 \le NERF \le \frac{N_{worst}(t)}{N_{worst}(t) - N_{best}(t)} \ , \tag{2.65}$$

with the lower (i.e. zero) and upper values occurring with $N(t) = N_{worst}$ and $N(t) = 0$, respectively. However, this latter case is not a value to aim for, since a null total population at end time also implies no active satellites.

2.10. Initial population and launch profile

An initial population file generates the average physical characteristics (area, mass, and radius) for each species in each altitude shell and provides the object distribution at the beginning of each simulation. After this stage, every object loses its identity (i.e. data on single objects is not stored) and becomes part of the data set with mean characteristics. In the same way, the mean physical features and altitude profile for launched objects are obtained from a file containing data on historical launches. The default numerical values are reported in Section 2.11.

Values of the initial population were derived from the European Space Agency (ESA) Meteoroid and Space Debris Terrestrial Environment Reference (MASTER) 2009 database created in October 2013 by the Institute of Aerospace Systems (Oswald *et al.*, 2005; Flegel *et al.*, 2011). The initial population is valid for objects equal to or larger than 10 cm and with perigee in LEO (Figure 2-13).

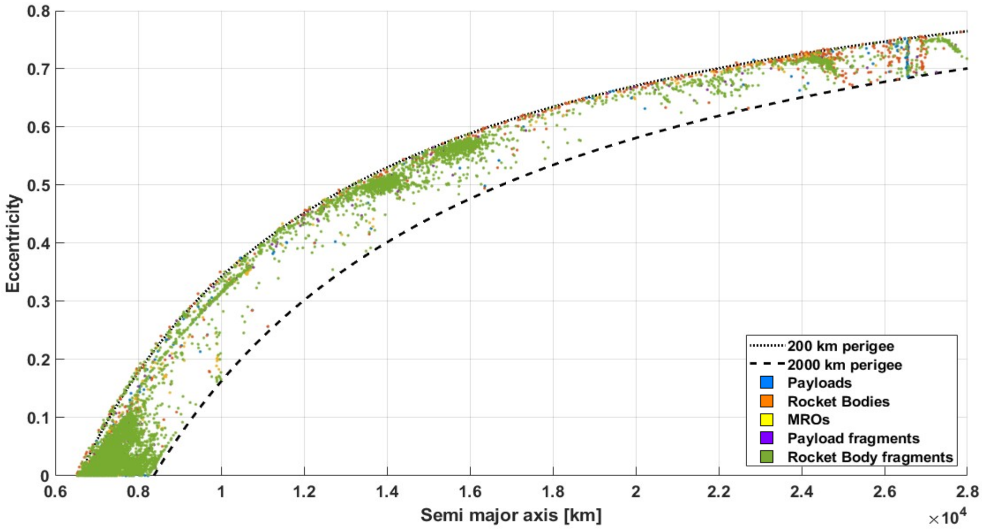

Figure 2-13. Distribution of the LEO crossing objects from MASTER 2009 as a function of the objects' semi-major axis and eccentricity.

A subset of LEO crossing objects was extracted because the model used in this study lacks the ability to compute drag on eccentric orbits (the LEO volume was discretised in concentric spherical shells). Below 200 km only a few objects with a short residual lifetime were excluded, while the other objects excluded reside primarily above 2,000 km due to the altitude of their apogee (Figure 2-13). For example, a spacecraft with a=26,600 and e= 0.74 (Molniya orbit) would reside for 99.7% of his orbit out of LEO; having a=14,000 and e=0.5 this percentage is 98.6%, and with a=10,000 and e=0.3 it decreases to 94.5% (note that a circular orbit at the higher limit of LEO would have a≈8370 km). This assumption results in having a smaller population compared to the original database and different spatial distribution, but these excluded objects would not have contributed in a significant way to the total collision risk.

The LEO-residing objects were computed as follows. The apogee and perigee altitude of an object in orbit is obtained by

$$\begin{aligned} h_A &= a(1+e)-r_E \\ h_P &= a(1-e)-r_E \end{aligned}, \tag{2.66}$$

where a is the semi-major axis, e the eccentricity and r_E the Earth radius (≈ 6370 km). For circular orbits ($e=0$) these two quantities are the same:

$$h_E = a - r_E\,, \tag{2.67}$$

and is here called equivalent circular height. For each object in MASTER 2009, only the objects with an equivalent circular height in LEO were selected, i.e. with

$$200\text{ km} \le h_E \le 2000\text{ km}\,. \tag{2.68}$$

A different approach was also tested. For each object, the fraction of the orbit spent in each shell was computed and used as weighting factor to assign the corresponding fraction of the object to each shell (excluding those above 2,000 km), i.e. if a satellite spent 40% of his time in shell A and 60% in shell B, 0.4 objects were assigned to A and 0.6 to B. Afterward, the total population in each shell was computed as the sum of all the object's fractions.

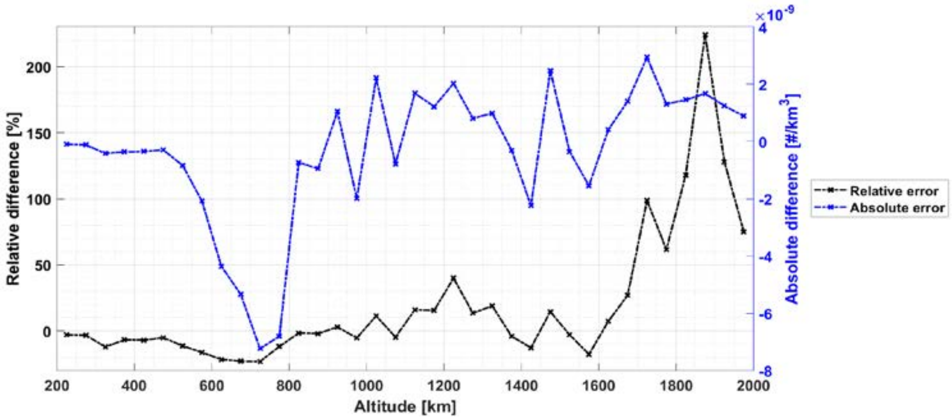

Figure 2-14. The absolute and relative error in the LEO-residing total population resulting from considering or not the objects' eccentricity.

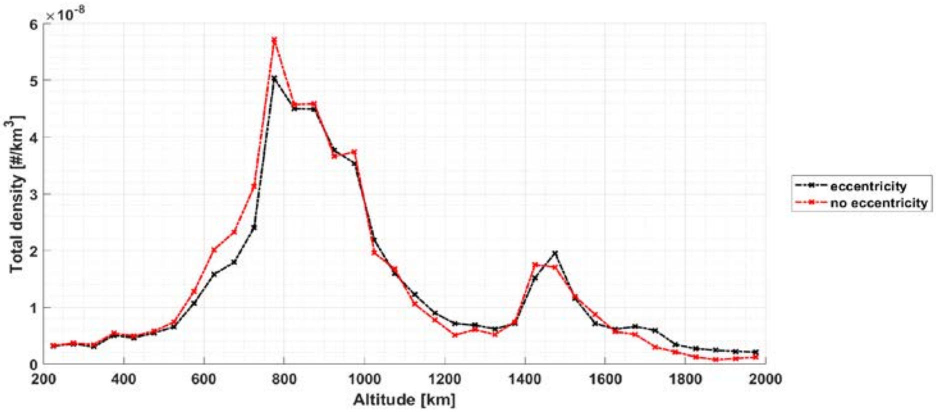

Figure 2-15. The total density of the LEO-residing population when considering or not the objects' eccentricity. The overlap of the two distributions is 93%.

The difference in the total LEO population obtained with the two methods was 1.67% after 200 years. Comparing the two sets, absolute and relative errors on spatial density were obtained (Figure 2-15). The relative error achieved different values, with the highest value in the upper part of LEO, where fewer objects were present. However, the absolute error remained below $3 \cdot 10^{-9}$ objects/km^3 except between 600 and 800 km, where the population computed without the eccentricity was higher. In addition, some of the errors are explained by a different distribution of the objects with the altitude, that might be assigned to different (close) shells depending on the eccentricity and on the shell boundaries. The spatial distribution was, as expected, also affected (Figure 2-14). Nevertheless, the two distributions were very similar overall, with an overlap of 93% (Figure 2-14). Results obtained in several scenarios, with different level of PMD compliance and removal rates showed, as expected, variation in the total number and distribution of the population, but not in the draw conclusions on the efficiency of the applied strategies.

When including the eccentricity, the physical behaviour of the objects will greatly differ from the reality, with a fraction of objects located in different altitudes shells, and therefore those in the lower ones would decay much faster than those at the upper ones, instead of having them circularised with a lowering of the apogee first. Therefore, acknowledging the limitations and consequences of the approach, it was preferred to modify the initial population so to have the equivalent circular height, as presented in Eq. (2.67), and have a real physical behaviour (i.e. the decay of circular objects).

Similar reasoning was used for the launch traffic and led to similar conclusions. The difference in object launched with the two approaches was minimal (1 object in the 8-yr profile), and the objects altitude distribution had an overlapping of 92% (Figure 2-16).

The typical values for key physical characteristics, such as mass, area and diameter are listed in Table 2-2. Depending on the species and altitude shell, the value used might greatly differ from the median (the mean or the mode), since some objects, especially in the payload species, can have very different characteristics. Visual representations of the distribution of the objects contained in the LEO residing subset of MASTER by physical characteristics and species are given in Figure 2-17, Figure 2-18, Figure 2-19, and Figure 2-20.

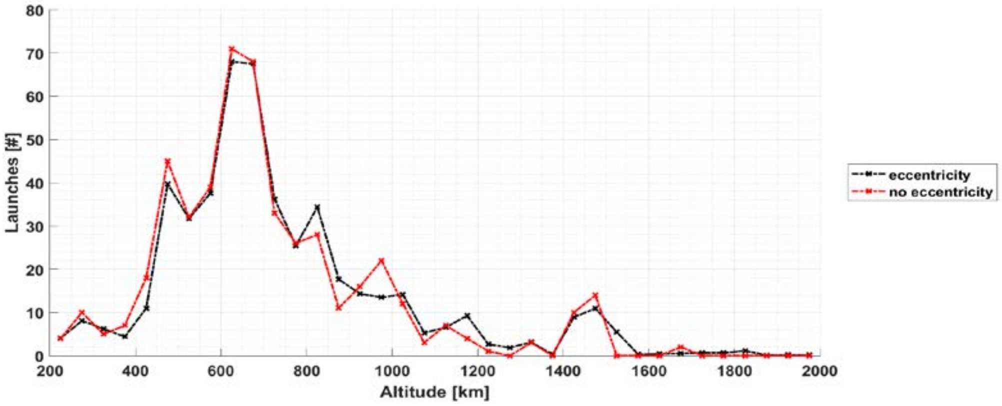

Figure 2-16. The number of LEO-residing in the 8-years launch profile when considering or not the objects' eccentricity. The overlap of the two distributions is 92%.

Table 2-2. Summary of statistics on mass, area and diameter by object species.

Object Species	Count	Mass [kg]			Area [m^2]	Diameter [m]
		Total		Median	Median	Median
Payloads	1,869	1,581,628	55.46 %	223	1.741	1.490
Rocket Bodies	835	1,157,993	40.60%	1,421	7.419	3.070
MROs	638	27,780	0.97%	25.96	0.120	0.390
Collision frag.	656	5,190	0.18 %	0.640	0.020	0.180
Explosion frag.	12,814	79,406	2.78 %	0.640	0.021	0.180
Total	16,812	2,851,999	100 %	1.082	0.033	0.220

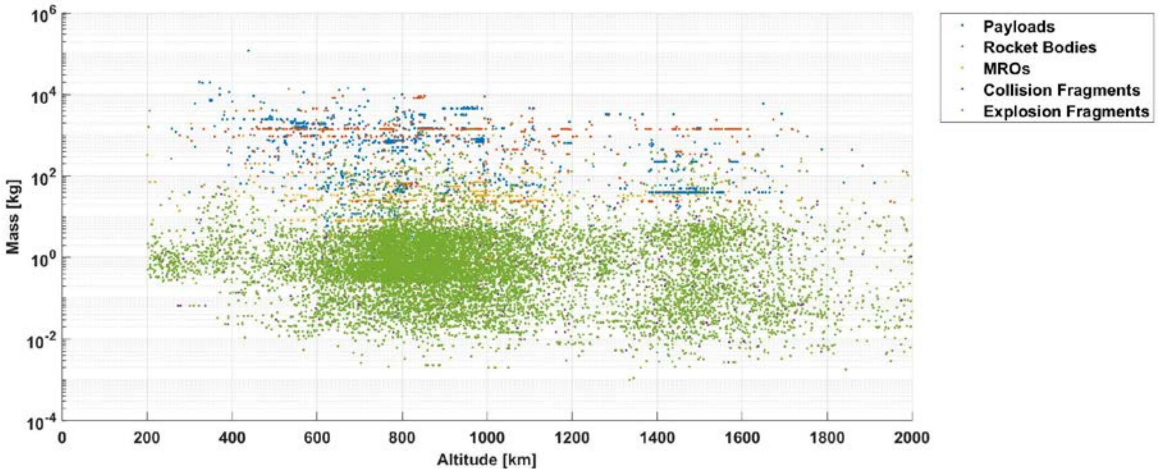

Figure 2-17. Distribution of objects' mass by species.

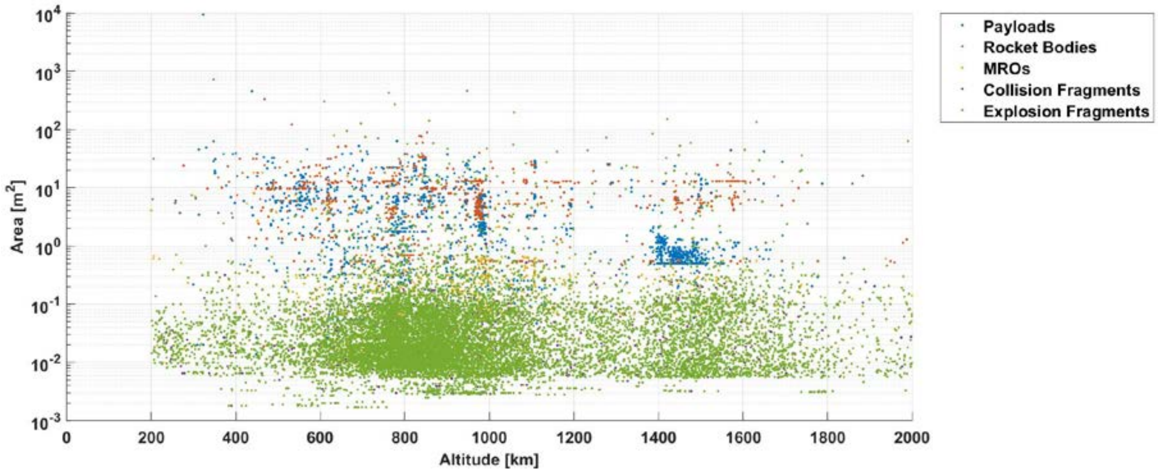

Figure 2-18. Distribution of objects' area by species.

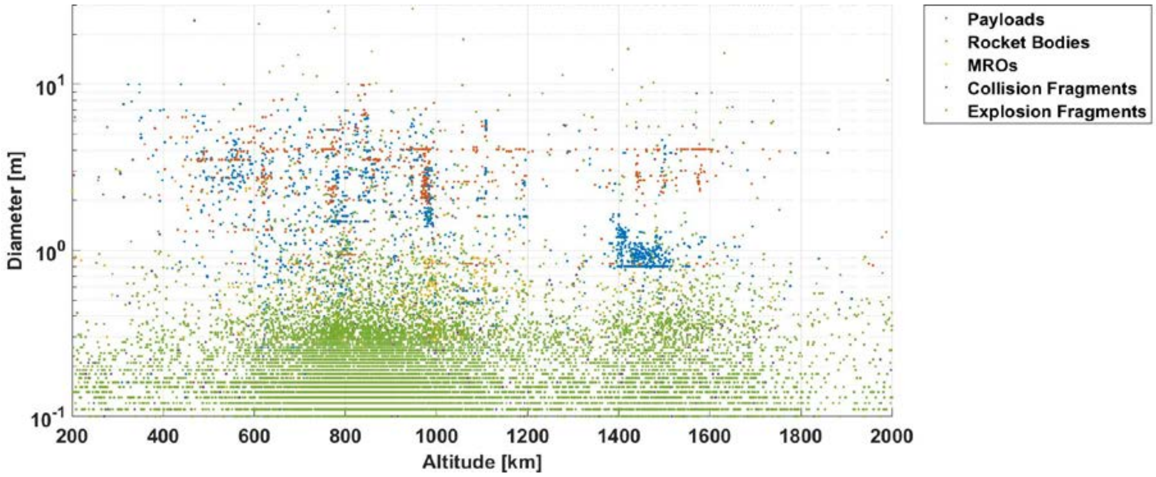

Figure 2-19. Distribution of objects' diameter by species.

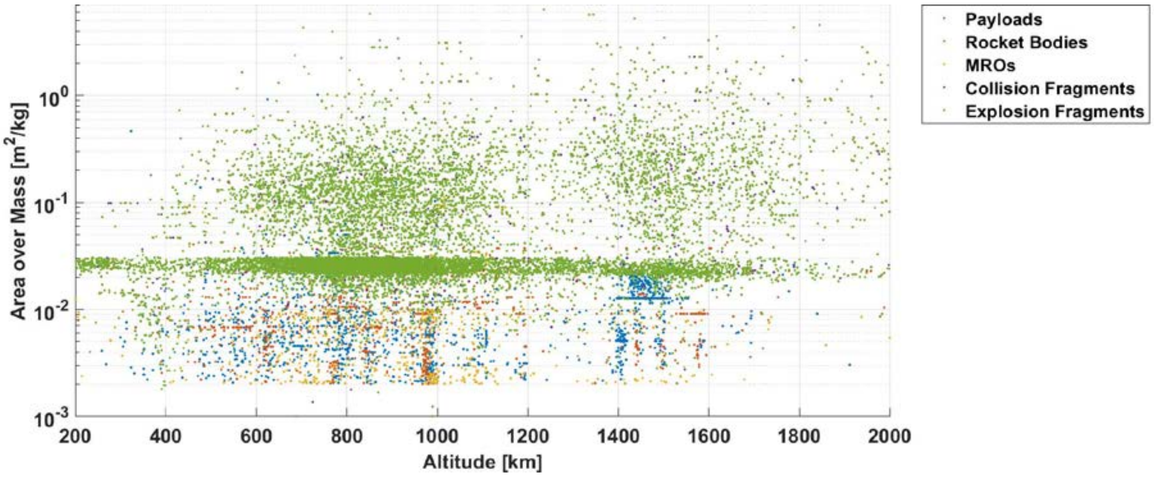

Figure 2-20. Distribution of objects' area over mass ratio by species.

2.11. Default parameters

The parameters used by the model can be varied by the user before the start of each simulation. However, if not specified, the default values listed in Table 2-3 are assumed. Other parameters were set equal to those used for the tuning of the model or derived from sensitivity studies (see Section 3.4).

The initial population (and the average physical characteristics of the objects within it) was computed from 16,812 LEO-residing objects extracted from the MASTER 2009 with a reference epoch of 1 May 2009 (Table 2-4, and Table 2-5) (Oswald *et al.*, 2005; Flegel *et al.*, 2011), assuming 10% of the payloads as active and launched just prior of the beginning of each simulation, thus with a complete 8-yr of operative life ahead. This value was obtained using a conservative approach from known data on active and inactive payloads (Flegel *et al.*, 2011; Bonnal and Mcknight, 2017). The model considered only objects bigger than 10 cm. This threshold corresponds to the historical detection limit of the Space Surveillance Network sensor and accounts for approximately 97% of the total mass in LEO (White and Lewis, 2014a).

Due to the continue evolution of the model and the available data, different initial population were used in the simulation presented in this thesis. For this reason, some analysis might appear as repeated, while there were maintained in order to compare the results obtained with the corresponding reference case. Unless stated otherwise, the default initial population and parameters were used.

A mean yearly launch profile was also obtained from a subset of the launches in the 2002-2009 time-frame (both years included), with 491 selected LEO launches (Figure 2-21, Table 2-4 and Table 2-6). Satellites were active for 8 years before becoming inactive. Then they were removed after 25 years with a PMD compliance of 90%. In addition, no explosions were allowed.

Table 2-3. Summary of the model default parameters.

Parameter	Value(s)
Projected period	2009 - 2209
Time-step	0.1 years
Minimum object size	0.1 m
Shells	36 (50 km thickness)
Initial population	Subset of Master 2009 (Table 2-5)
Launch traffic model	Annual launch rate based on Table 2-6
Explosions	No
Solar cycle	11-yr cycle
Satellite operational time	8 years
Satellite residual lifetime	25 years
PMD compliance level	90%

Table 2-4. Composition of the default initial population and launch profile.

Object species	$N(t_0)$	Total launches (8-yr)
Total intact objects	*3,342*	*491*
- **Active payloads**	187	301
- **Inactive payloads**	1,682	
- **Rocket bodies**	835	110
- **MROs**	638	80
Total fragments	*13470*	*0*
- **Collision fragments**	656	0
- **Explosion fragments**	12,814	0
Total	**16,812**	**491**

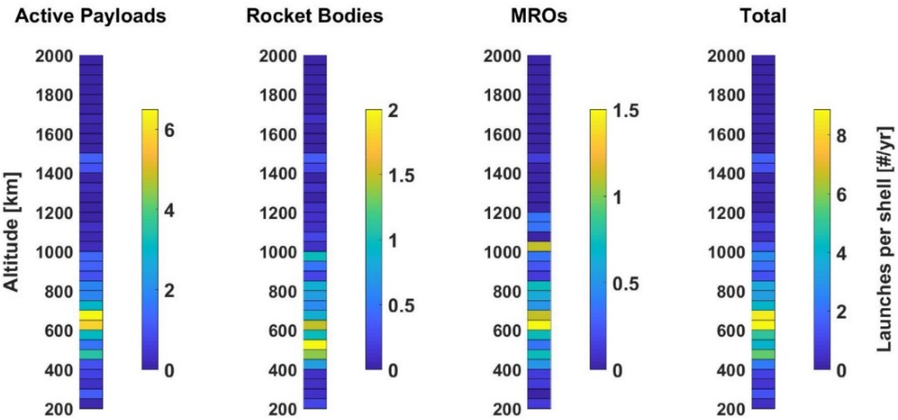

Figure 2-21. Distribution of the annual launch rate as a function of the altitude shell and species.

Table 2-5. The default initial population.

Altitude [km]	**Total Payloads**	**Rocket Bodies**	**MROs**	**Collision Fragments**	**Explosion Fragments**	**Total**
200-250	0	2	5	6	76	89
250-300	3	2	4	6	87	102
300-350	10	3	1	3	80	97
350-400	15	6	0	6	128	155
400-450	16	8	9	5	106	144
450-500	39	19	6	6	100	170
500-550	35	23	14	4	145	221
550-600	69	33	20	12	254	388
600-650	75	73	30	24	419	621
650-700	90	25	43	25	544	727
700-750	63	21	57	38	813	992
750-800	237	84	53	72	1,392	1,838
800-850	110	58	35	57	1,230	1,490
850-900	48	40	27	61	1,340	1,516
900-950	71	31	45	50	1,029	1,226
950-1000	190	167	97	50	766	1,270
1000-1050	22	16	34	29	573	674
1050-1100	28	26	45	25	461	585
1100-1150	58	16	28	14	257	373
1150-1200	22	25	16	11	205	279
1200-1250	2	5	3	7	168	185
1250-1300	7	3	3	9	200	222
1300-1350	10	8	5	10	161	194
1350-1400	41	11	8	12	208	280
1400-1450	314	29	16	15	294	668
1450-1500	218	22	8	21	393	662
1500-1550	42	16	8	18	383	467
1550-1600	12	43	7	16	268	346
1600-1650	7	6	4	16	196	229
1650-1700	9	4	1	9	189	212
1700-1750	0	3	3	9	108	123
1750-1800	3	3	0	2	81	89
1800-1850	1	0	0	2	49	52
1850-1900	1	0	1	3	27	32
1900-1950	1	1	1	0	39	42
1950-2000	0	3	1	3	45	52
Total	**1,869**	**835**	**638**	**656**	**12,814**	**16,812**

Table 2-6. Distribution of launched objects by altitude and species in the 8-yr reference period.

Altitude [km]	**Intact Payloads [#/yr.]**	**Rocket Bodies [#/yr.]**	**MROs [#/yr.]**	**Total launches [#/yr.]**
200-250	1	2	1	4
250-300	9	1	0	10
300-350	3	1	1	5
350-400	5	1	1	7
400-450	8	6	4	18
450-500	28	11	6	45
500-550	13	16	3	32
550-600	25	8	6	39
600-650	47	12	12	71
650-700	52	7	9	68
700-750	24	5	4	33
750-800	15	6	5	26
800-850	15	7	6	28
850-900	8	2	1	11
900-950	10	4	2	16
950-1000	11	8	3	22
1000-1050	2	1	9	12
1050-1100	1	2	0	3
1100-1150	3	1	3	7
1150-1200	0	1	3	4
1200-1250	0	1	0	1
1250-1300	0	0	0	0
1300-1350	2	1	0	3
1350-1400	0	0	0	0
1400-1450	8	2	0	10
1450-1500	10	3	1	14
1500-1550	0	0	0	0
1550-1600	0	0	0	0
1600-1650	0	0	0	0
1650-1700	1	1	0	2
1700-1750	0	0	0	0
1750-1800	0	0	0	0
1800-1850	0	0	0	0
1850-1900	0	0	0	0
1900-1950	0	0	0	0
1950-2000	0	0	0	0
Total	**301**	**110**	**80**	**491**

2.12. Model implementation

The MISSD model was developed and implemented in Matlab. It uses a modular approach with multiple files and functions dedicated each to a specific task, such as computing the control, performing the integration, displaying and saving figures and logs (Figure 2-22). In addition, MISSD is also able to automatically perform a series of test (e.g. for sensitivity analysis) thanks to a batch module that recursively runs the model until all the scenarios are executed (Figure 2-23).

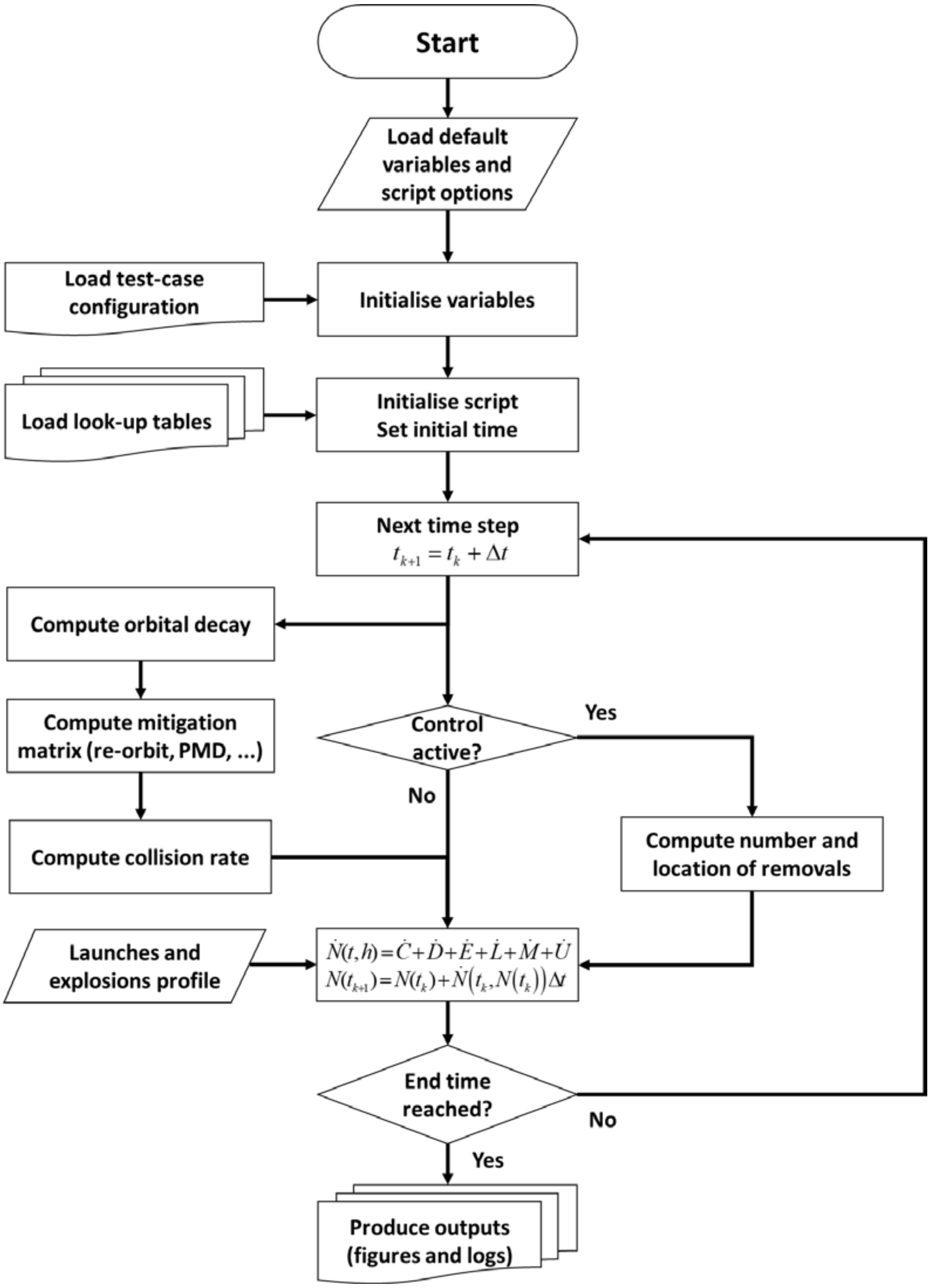

Figure 2-22. Schematics of the implementation of MISSD.

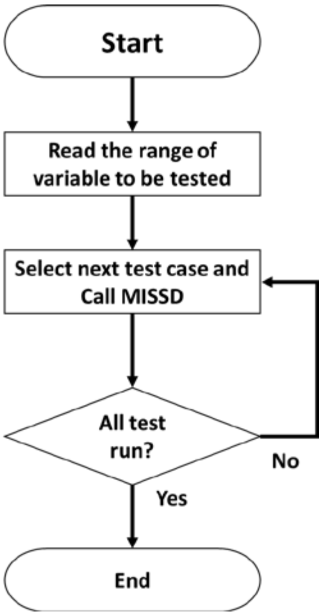

Figure 2-23. Schematic of how the MISSD model executes multiple tests in batch.

Referring to the schematics in Figure 2-22, during each test, the software starts by loading the default parameters (e.g. Earth radius, gravitational constant), variables (e.g. input files, launch profile) and options (e.g. which plots to display or save). These values also can be overwritten by those specified in the test-case configuration file. The script then loads external look-up tables (which path is defined in a variable as well) and initialise additional variables and matrix based on the previous data and options. At this point, a loop is run for each time step until the end time. For each iteration, the system of Equations (2.8) are solved after each component have been computed (i.e. collisions, drag, explosions, launches, mitigation, control). Lastly, several different plots might be displayed and saved depending on the set options. An output log is also written. It contains both the results and all the information needed to reproduce the simulation, i.e. the value of the parameters, variables, options, and the version of the used input files and Matlab scripts.

Concerning the execution time, a relationship also exists between the execution time and both the selected time step and the number of shells (see Figure 2-24 and Figure 2-25). However, compared to previous versions of the software, thanks to code refactoring, the scripts performances were improved of about a factor of ten. As result, in normal simulations (Figure 2-26), each run takes about 2-4 seconds to run depending on the settings and the required output to be written on disk (using a Toshiba Satellite Pro P855-10K with i7-3610 @2.4 GHz with 8GB DDR3 RAM @1,600 MHz).

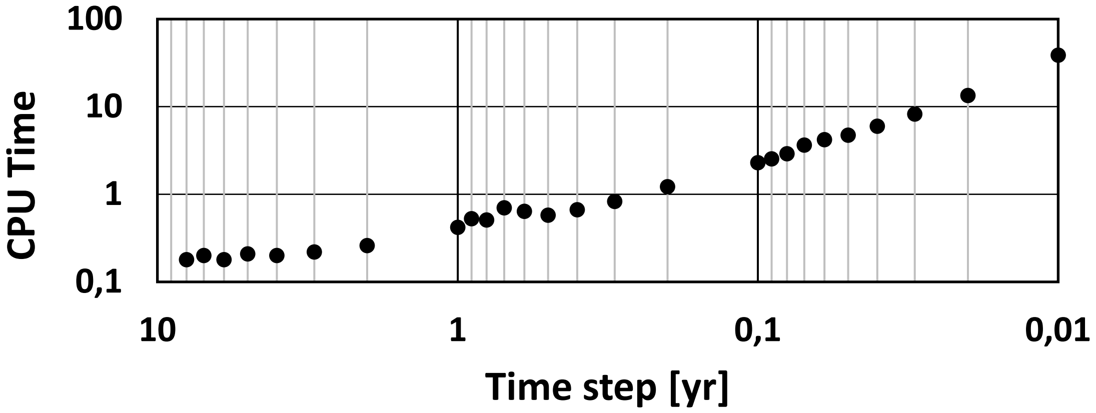

Figure 2-24. Variation of the computational time with the integration time step (Section 3.1.1).

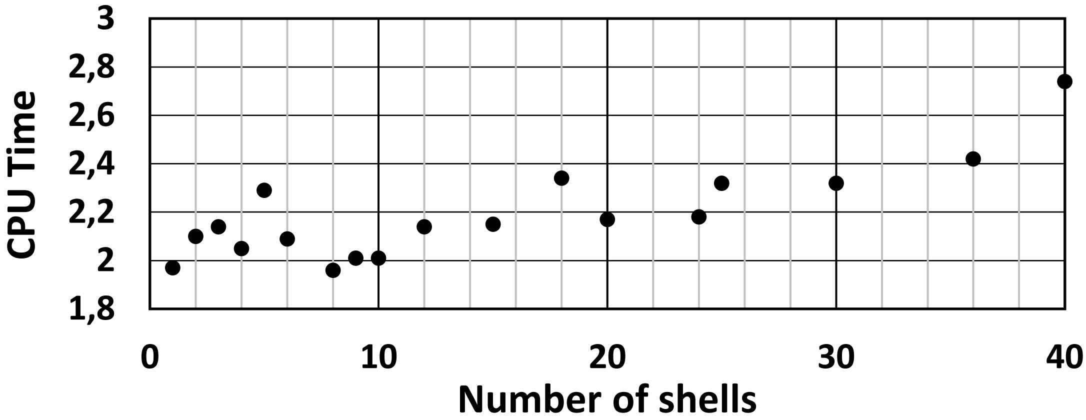

Figure 2-25. Variation of the computational time with the number of altitude shells (Section 3.1.2).

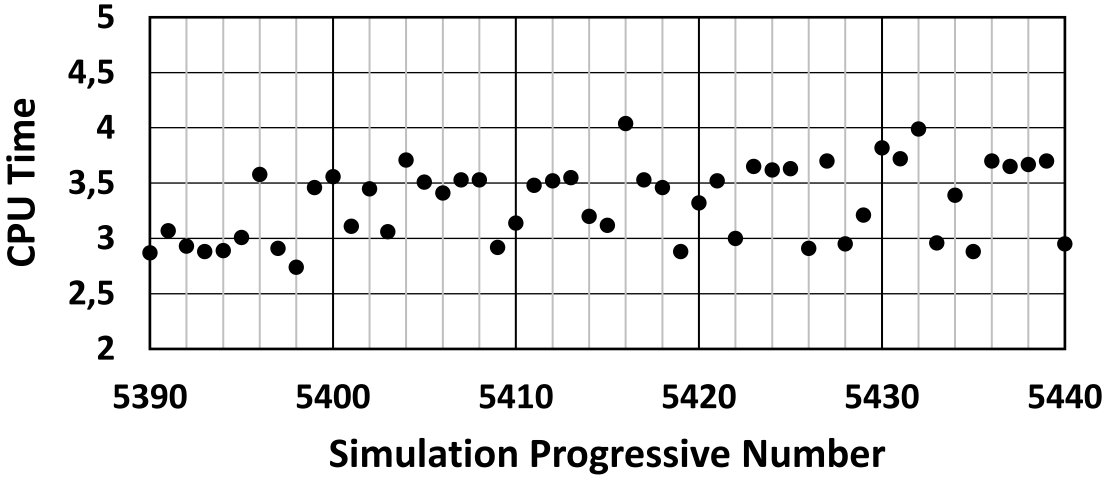

Figure 2-26. The computational time during 50 consecutive simulations.

Chapter 3. Model tuning

Many simulation parameters have significant uncertainty or may not be predictable or controllable at all by their nature (e.g. the solar cycle) but can, however, influence the simulation outcomes (Dolado-Perez, Pardini and Anselmo, 2015).

In fact, there are many uncertainties related to the space debris problem, and we are not even able to know exactly the current situation of the orbital environment. Indeed, there are many unknown debris, some of which we are incapable of locating and tracking due to their small size, position, or surface properties. Conversely, other debris are trackable but since they have unknown or classified origins, are not included in all the public catalogue. For example, the Space Surveillance Network tracks but does not contain in their catalogue several thousand objects belonging to the US military or related to defence and intelligence, making the catalogue 40% incomplete overall (Pardini and Anselmo, 2014).

Other than the initial debris environment, some other variables are only under partial control of the modellers, i.e. their precision can be improved with more knowledge or with more complex models. Falling into this category are the model of the atmospheric density, the break-up models, the collision probability estimation, the long-term trajectory estimation and the energetic and geometric configuration that lead to catastrophic break-up (Dolado-Perez, Pardini and Anselmo, 2015). Moreover, when the quantities are strictly related to future events, they will never be precisely predicted (even with very accurate models) due to their stochastic nature. Among these variables, completely outside the control of modellers, there are the solar and geomagnetic activity, the future launch traffic (number of satellites, masses, date of launches, ...), technology evolution, quality of adopted mitigation and their compliance, accidents (such propellant leak, explosions and collisions) and irresponsible deliberate actions, such ASAT tests (Dolado-Perez, Pardini and Anselmo, 2015).

Therefore, it is essential to perform sensitivity analysis to test the response of the model to the variation of the input parameters. For this reason, tests were performed to select the appropriate number of altitude shells and the integrator timestep (Section 3.1). The model results were also compared against the IADC study of 2013 (Liou *et al.*, 2013) both with and without the revised version of the break-up law used by some of the models in the original study (Section 3.2). After analysing the results from a scenario run with the default parameters (Section 3.3), the model response to the variance of input parameters was tested with sensitivities analysis on the level of PMD adoption and the launch rate (Section 3.4).

3.1. **Model tuning**

3.1.1. Selection of the integrator time step

This study investigated the sensitivity of the model outputs to the time step used in the Euler integrator and selected the most appropriate one to be used in the following simulations. The analysis used the default parameters listed in Section 2.11 and tested the 26 timesteps from 0.01 to 8 years. This latter value is the maximum one the model can test without editing a series of parameters which will invalidate the results. For example, the satellites, which have a default operational time of eight years, would be removed in the same time step in which they were being added, resulting in no new intact sources. Moreover, wider timestep would provide a too coarse representation of the real dynamics of the system.

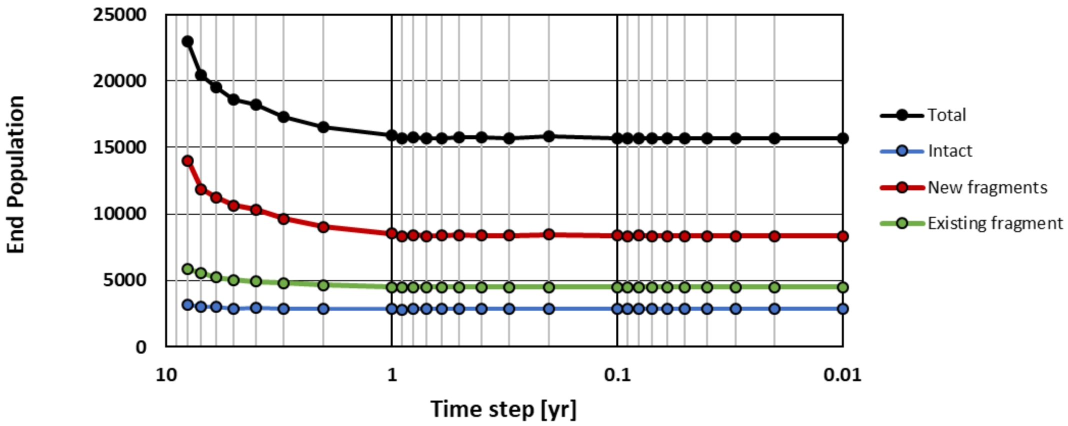

Figure 3-1. The composition of the end population as a function of the integrator time step.

The variation of the end population converged to asymptotic values when reducing the time step, with a more prominent effect on collisions and thus newly generated fragments (Figure 3-1). For time steps equal to or over one year, the error on the end population compared to the smallest time step tested (0.01 years), ranged between 1,18% and 41,49%, while was always less than 0.76% and 0.04% for time steps in the range of 0,1-0,9 and 0,01-0,09 years, respectively.

To conclude, the model results were proven to be dependent on the time step used in the Euler integrator. However, for a time step smaller than one year, the errors are less than 1% compared to using a very small time step (0.01). Reducing the time step below 0.1 years proved to have minimal benefits while increasing the computational time required to run the simulations (see Figure 2-24). The time step of 0.1 years was chosen as the default value as a result of a trade-off between the time step utilised and the residual error, and the lack of need to model discrete daily events.

3.1.2. Number of altitude shells

An analysis was performed to check the sensitivity of the results with respect to the number of altitude shells using the default parameters listed in Section 2.11. The model was tested with 18 different sets of altitude shells, listed with their altitude thickness in Table 3-1. The shell thickness had an integer value in order not to interpolate the decay lookup table (which has a 1 km resolution). The maximum number of shells was set to 40. Indeed, this upper limit was required because a higher value would have produced very sparse decay, area and mass lookup tables (obtained from the initial population), and in some shells, it would not have produced any reference values, or they would have resulted from the average of a very few samples. The 40-shell case is a limit case and is here reported for completeness, but it was decided a priori not to use more than 36 shells.

Table 3-1. Altitude shell thickness as a function of the number of shells.

Number of shells	Thickness [km]	Number of shells	Thickness [km]
1	1800	**12**	150
2	900	**15**	120
3	600	**18**	100
4	450	**20**	90
5	360	**24**	75
6	300	**25**	72
8	225	**30**	60
9	200	**36**	50
10	180	**40**	45

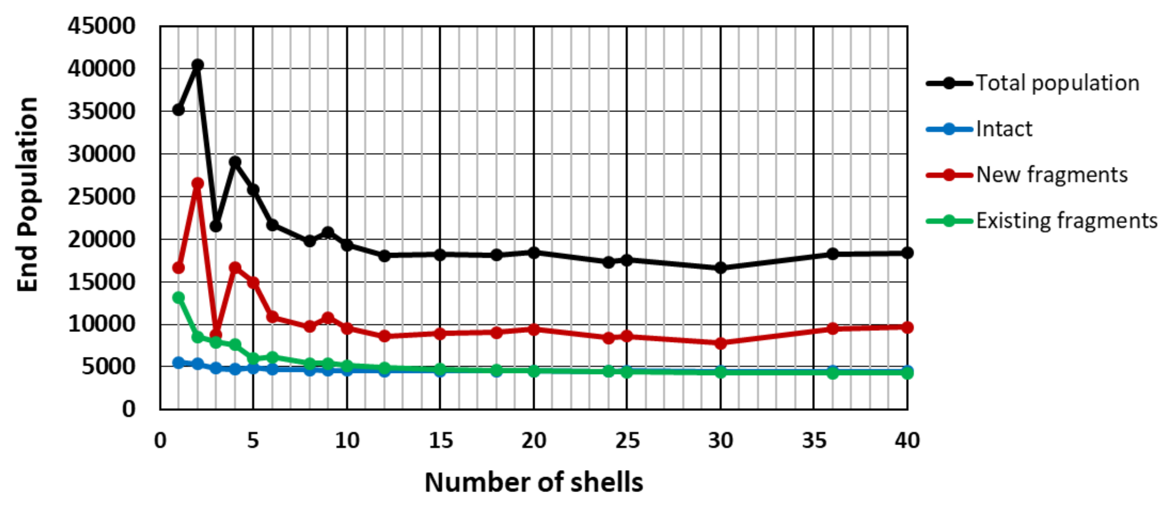

Figure 3-2. The end populations as a function of the number of shells.

Table 3-2. Results at the end time when varying the number of altitude shell.

Number of shells	**Intact objects**	**New collision fragments**	**Existing fragments**	**Total**	**Total collisions**
1	5,504	16,548	13,057	35,109	38
2	5,338	27,850	8,947	42,135	79
3	4,867	9,394	8,098	22,359	35
4	4,751	17,617	8,030	30,399	64
5	4,900	16,007	6,206	27,112	62
6	4,753	11,731	6,456	22,939	51
8	4,647	10,617	5,678	20,942	51
9	4,644	11,673	5,671	21,988	57
10	4,618	10,322	5,430	20,369	48
12	4,575	9,305	5,178	19,058	44
15	4,571	9,647	4,970	19,188	47
18	4,545	9,785	4,844	19,174	49
20	4,517	10,235	4,777	19,528	51
24	4,512	9,129	4,669	18,310	45
25	4,515	9,423	4,650	18,588	49
30	4,509	8,518	4,558	17,585	45
36	4,492	10,371	4,499	19,362	52
40	4,493	10,560	4,467	19,519	50

Table 3-3. Percentage variation of the results at the end time compared to the 36-shell case.

Number of shells	**Percentage variation on**				
	Intact objects [%]	New collision fragments [%]	Existing fragments [%]	Total [%]	Total collisions [%]
1	22.5	59.6	190.3	81.3	-27.4
2	18.8	168.5	98.9	117.6	51.9
3	8.4	-9.4	80.0	15.5	-32.6
4	5.8	69.9	78.5	57.0	22.8
5	9.1	54.3	37.9	40.0	20.5
6	5.8	13.1	43.5	18.5	-0.8
8	3.5	2.4	26.2	8.2	-2.5
9	3.4	12.5	26.1	13.6	9.5
10	2.8	-0.5	20.7	5.2	-8.2
12	1.8	-10.3	15.1	-1.6	-14.6
15	1.8	-7.0	10.5	-0.9	-9.9
18	1.2	-5.7	7.7	-1.0	-5.7
20	0.6	-1.3	6.2	0.9	-2.5
24	0.4	-12.0	3.8	-5.4	-12.8
25	0.5	-9.1	3.4	-4.0	-6.4
30	0.4	-17.9	1.3	-9.2	-12.7
36	0.0	0.0	0.0	0.0	0.0
40	0.0	1.8	-0.7	0.8	-3.1

Results showed a dependency of the outcome of the simulations on the number of shells. When selecting less than five shells, the trend in the orbital populations was highly variable (Figure 3-2). However, increasing the number of shells, a clear trend appeared for the number of intact and existing fragments (Table 3-2), for which the residual when errors compared to 36 shells dropped steadily (Table 3-3). For the number of collisions and newly generated collision fragments, the errors varied by several percentage points, for cases with less than five shells being particularly affected by the discretisation process. With few shells, the residential times in each band were computed using a single decay parameter over a wide range of altitude, with the extreme case of 1 shell in which all objects decayed at the same rate despite their altitude. The total number of collisions is highly depended on the number of shells (Figure 3-3).The total collisions remained between 44 and 52 in 12 out of 18 cases, 10 of which when selecting more than ten shells. A different number of objects were assigned to different shells depending on their initial position and launch profile, varying, therefore, the collision rates at the initial time and also afterwards. In addition, increasing the number of shells improved the decay accuracy (as demonstrated by the reducing error on the existing fragments) but led to computing the mean characteristics based on fewer objects.

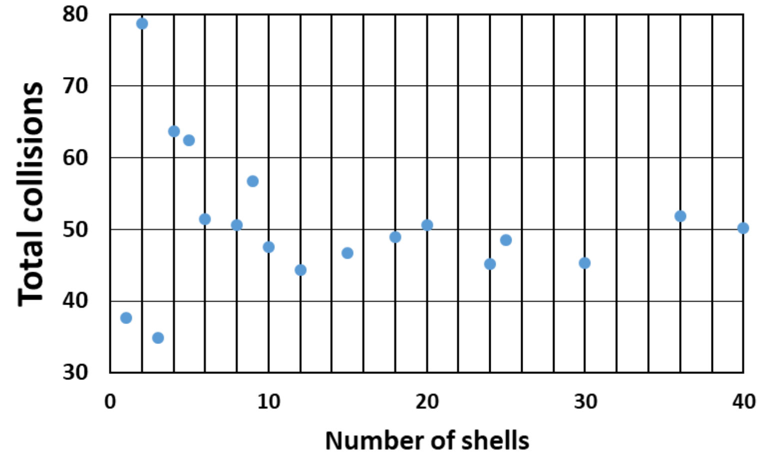

Figure 3-3. The number of collisions as a function of the number of shells.

To conclude, with less than 10 altitude shells there was high variability in the model output, while results followed an asymptotic trend increasing the number of shells for intact objects and existing fragments. Collisions had a variable trend, but, if needed, they can be tuned with a corrective parameter (see Eq. (2.20)). It was decided to select 36 shells as default value since the residual error of the end time population of intact and existing fragments decreased with the number of shells. The population of new fragments at end time swept a wide range of values, but for the 36-shell case had similar values with 8, 10, 18, 20, and 40 shells, in these cases with a maximum error of 5.7%. In addition, others author in the literature often used 50, 100 or 200 km as shell thickness (Cordelli *et al.*, 1993; Rossi *et al.*, 1994; Bennett and Sang, 2011; Kebschull *et al.*, 2013), and therefore, the selection of 36 shells (corresponding to a 50-km thickness) allowed to generate outputs easily comparable (in term of altitude) when grouping together results from adjacent shells.

3.2. Comparison with the IADC 2013 study

In 2013, the IADC performed a study with several evolutionary models, including the SDM, DELTA, KS Canonical Propagation model (KSCPROP), Low Earth Orbital Debris Environment Evolutionary Model (LEODEEM), LEGEND and DAMAGE (Inter-Agency Space Debris Coordination Committee *et al.*, 2013; Liou *et al.*, 2013). This study suggested that, regardless of the mitigation measures currently adopted, the mean number of debris will likely increase in the next 200 years (Figure 3-4). As a result, ADR was proposed as a possible additional strategy.

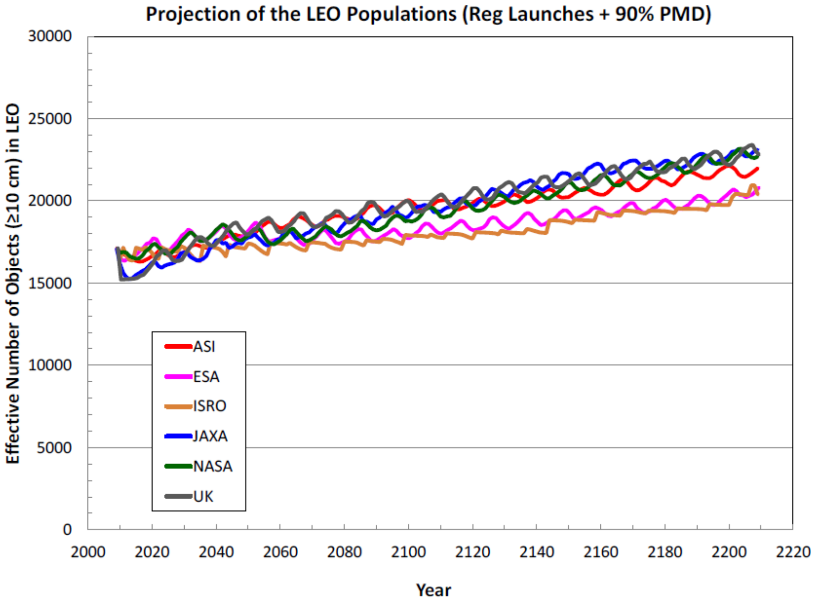

Figure 3-4. The effective number of objects larger than 10 in LEO obtained in the IADC study with six different models (Inter-Agency Space Debris Coordination Committee *et al.*, 2013).

The analysis presented here ran for 200 years and used the same (optimistic) assumptions of the original study: no new explosions (passivation effectiveness equal to 100%, and existing debris objects did not explode), with 90% of satellites decaying in 25 years after an operational lifetime of 8 years.

Other model parameters were set to the default ones (Section 2.11). In the results, rocket bodies, payloads (both active and inactive), and MROs were combined into the intact object category so to compare with the same object species used in the original work (i.e. intact objects, existing fragments, and new collision fragments).

MISSD uses a subset of the MASTER database and has, thus, a lower initial population. Therefore, to avoid this bias in the initial population (and in its evolution), it was scaled up to the same initial population used in MASTER. This, however, had the caveat of changing the overall objects distribution of a few percentage points.

Several models in the IADC study used the standard NASA breakup model with a misleading implementation for the mass conservation during collisions (Johnson *et al.*, 2001), that was later clarified two years before the IADC study (Krisko, 2011). The same formula was then utilised here to ensure consistency in the comparison of numerical results.

The end population from the six models used in the IADC study increased on average by 30%, fitting with the 30.1% value obtained with MISSD. It must be noted that the solar cycle caused periodic ripples in the population. Therefore, the measured values might not assume the maximum (or the minimum) value at the end time (see the periodic variations in Figure 3-5). This effect also occurred in the following results and will be further omitted.

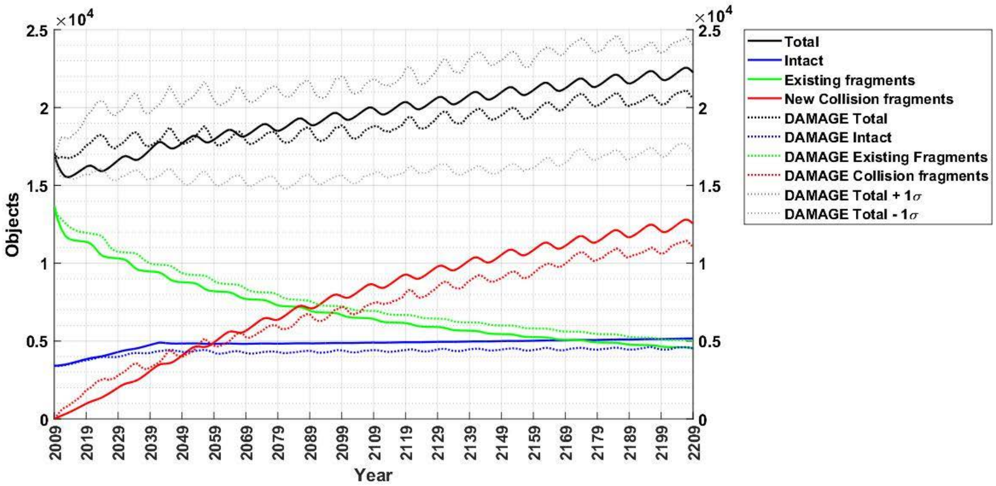

Figure 3-5. Comparison of the LEO population evolution between DAMAGE (dotted lines) and MISSD (solid lines).

The UK Space Agency's model DAMAGE (Lewis *et al.*, 2001) was selected to perform a more complete comparison. The two models are very different: DAMAGE includes perturbations (like the Earth's oblateness) and propagates all the orbital elements, while MISSD uses a statistical source-sink approach with spherical symmetry in both Earth and orbits (therefore value and variations in e, i, Ω, and ω are not considered). Even with such differences, MISSD achieved results for all object species within 14% of DAMAGE (Table 3-4), but more importantly, similar conclusions can be drawn. In both models, existing fragments tended to reach a dynamic equilibrium toward the end of the simulation (Figure 3-5), with new collision fragments becoming the dominant population after the year 2100. The total number of intact objects and new fragments at end time were higher in MISSD (Table 3-4), while the total number of collisions was 70.14 compared with 63.37 for DAMAGE. MISSD results did not fit perfectly with those from DAMAGE, but they were inside its one sigma standard deviation (which reached up to 3,703 objects on the total population at end time), and therefore among those more likely to occur (Figure 3-5).

Table 3-4. The population at the end time (and its percentage variation with respect to the initial one) with MISSD and DAMAGE models. The last column indicates the percentage variation of MISSD compared to DAMAGE.

Object species	$N(t_0)$	**End population**	**DAMAGE**	**% Variation**
Intact objects	3,410	5,143 (+51.4%)	4,540 (+33.14%)	+13.7%
New fragments	0	12,538 (-)	11,060 (-)	+13.4%
Existing fragments	13,697	4,549 (-66.8%)	4,979 (-63.65%)	-8.6%
Total	**17,107**	**22,250** **(+30.1%)**	**20,579** **(+20.30%)**	**+8.1%**

3.2.1. Influence of the solar cycle

The same parameters of the simulations run in Section 3.2 were used as a base to perform a comparison analysis without the implementation of the 11-yr solar cycle study, here replaced with a long-term mean value of the solar activity (see Section 2.4.3). The results from this latter case can be seen as the sum of a base trend with an 11-yr periodic function. The results are similar, but they do not entirely overlap due to the difference between the long-term average of the solar activity (used when the solar cycle is not considered) and the mean action of the solar cycle, which is linked to the variation of the exospheric temperature (Figure 3-6, and Section 2.4.3).

At the end time, where the differences were greater, the number of intact objects varied by 0.4% (Table 3-5). The different atmospheric density profile had a greater repercussion on both the existing and the newly generated fragments due to their higher area over mass ratio (compared to intact objects), with differences of -4.3% and -5.7%, respectively (Table 3-5), resulting also in a 3.2% difference in the total number of collisions (67.89 vs 70.14). The removal of the solar cycle changed the absolute values of the outputs but did not change the overall dynamics of the system.

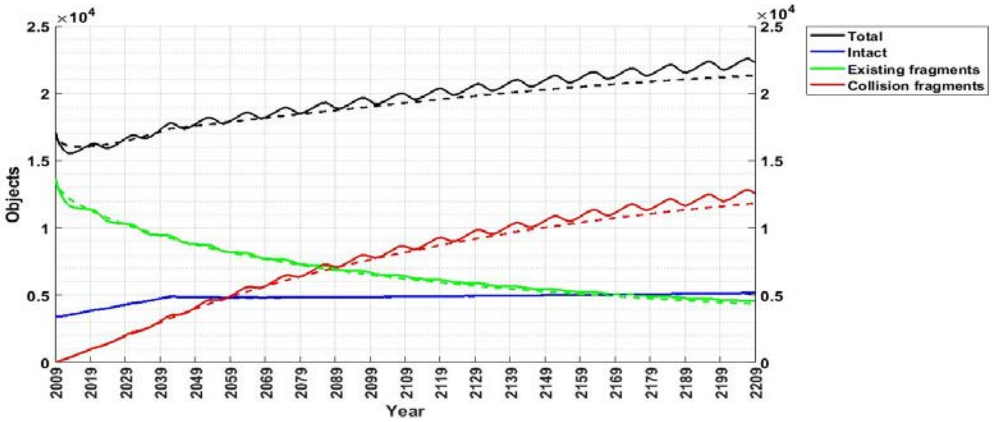

Figure 3-6. Evolution of the population in the scenario with solar cycle (solid lines) and without it (dashed lines).

Table 3-5. The population with and without the solar cycle at the end time (and its percentage variation with respect to the initial one).

Object species	$N(t_0)$	**End pop. no solar cycle**	**Variation w.r.t. with solar cycle [%]**	**Variation w.r.t. DAMAGE [%]**
Intact objects	3,410	5,163 (+50.8 %)	+0.4%	+13.3%
New fragments	0	11,823 (-)	-5.7%	+6.9%
Existing fragments	13,697	4,355 (-68.2 %)	-4.3%	-12.5%
Total	**17,107**	**21,322** **(+24.6%)**	**-4.2%**	**+3.6%**

3.2.2. Comparison with the revised break-up model

A test similar to the one carried out in Section 3.2 was performed using the same settings, except for the collision fragments, here computed with the proper implementation of the breakup formula that corrects for the kinetic energy of the impacting objects (Krisko, 2011). Except for the comparison test in Section 3.2, all simulations in this thesis used the revised version of the formula.

As expected, the number of intact objects at the end time was lower compared to the case without the revised formula, due to the higher number of collisions (Table 3-6), while collision fragments increased by 23.6%. (with respect to. the wrong formula, see Table 3-4)

Table 3-6. Results obtained with the revised formula of the NASA breakup model.

Object species	**Initial population**	**End population**	**Variation [%]**
Intact objects	3,410	4,123	+ 20.91
New fragments	0	16,894	-
Existing fragments	13,697	4,651	- 66.04
Total	**17,107**	**25,669**	**+ 50.05**

3.3. Analysis of a scenario with default parameters

A scenario which used the default parameters (Section 2.11) was selected to define baseline results and trends and to distinguish the effects caused by the variation of the tested parameters from other behaviours that are always present in the model.

The total end population increased by 43.6%, and it was composed mainly by collision fragments (Figure 3-7, Table 3-7). The explosion fragments decreased by 66.8% due to the effect of drag and to the assumption of no new explosions during the simulations.

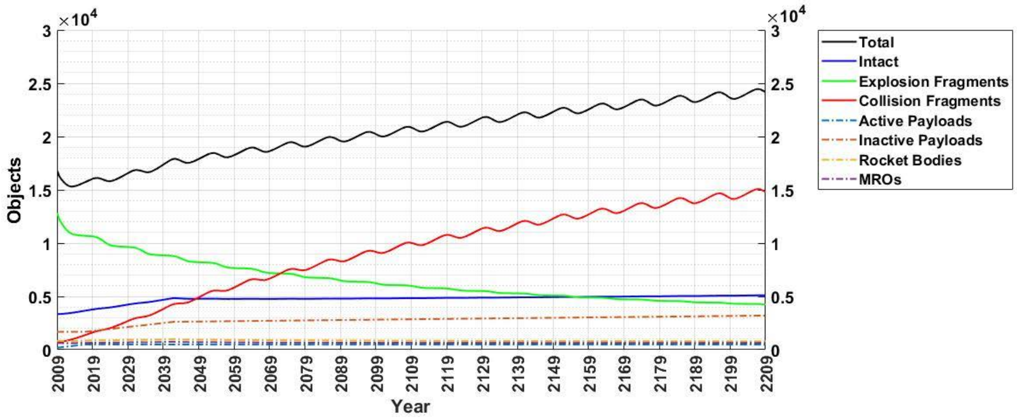

Figure 3-7. The evolution of the number of objects in LEO for each species in the reference case.

Table 3-7. The orbital populations in the reference case at the initial and end time. Newly generated collision fragments were the main contributor to the total population at the end time.

Object species	**Population at the end time**	**Variation w.r.t the initial population [%]**
Intact objects	5,103	+52.7
- Active Payloads	480	+156.7
- Inactive Payloads	3,203	+90.4
- MROs	789	-5.5
- Rocket Bodies	631	-1.1
New collision fragments	14,793	+2,155
Explosion fragments	4,243	-66.8
Total	**24,139**	**+43.6**

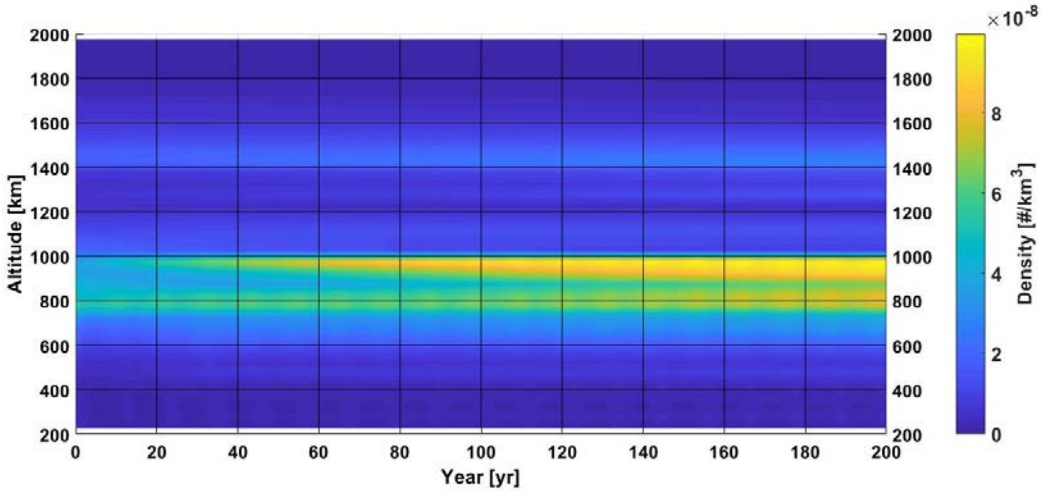

Figure 3-8. The evolution of the total spatial density (i.e. computed across all species) in the reference case.

For altitudes lower than 600 km, the beneficial effect of the atmospheric drag was able to counteract the initial high value of mass, limiting the increase in the orbital population over time. The major density peak at the beginning of the projection period occurred at the altitude of 750-800 km (Figure 3-8). With time, it increased in magnitude to a plateau that extended upwards to the 850-900 km shell.

The total density in the 900-1,000 km region increased over time, reaching an absolute maximum value of 1.02×10^{-7} objects/km^3. Here the beneficial effect of the atmospheric drag was weaker than at lower altitudes. The composition of the initial population and the continuous launches to the 900-1050 km region contributed to the formation of a new high-density-peak region (Table 2-5, Table 2-6), with the 950-1,000 km shell having at the initial time the highest number of rocket bodies (167) and was the 4th most crowded for payloads (190). The initial and launched objects remained in the environment for a longer period but eventually decayed, forming a high-density region that scattered objects to lower altitudes toward 900 km, almost merging with the previous region. Compared to altitudes down to 750 km, in this region resided more intact objects (payloads and rocket bodies) with high cross-section area and mass, two factors that contribute to the increase of collision probability and the number of generated fragments.

A third high-density region was found at 1400-1550 km (Figure 3-8). Here, in addition to Earth's observation and communication satellites (e.g. Globalstar), in the mid-1970s, three second stages of Delta rockets exploded producing several clouds of debris, which remained at the same altitude due to the negligible effect of drag. Similar critical regions were found by Kessler studying the 1999 catalogued population, as depicted in Figure 3-9 (Kessler *et al.*, 2010). The differences in the values and peaks of spatial densities where due to the difference in the catalogued population (see also the plot of the total spatial density depicted in Figure 2-14).

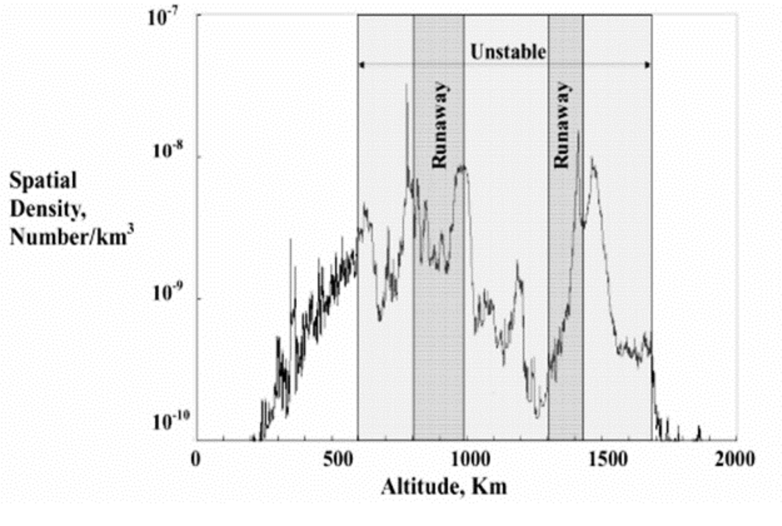

Figure 3-9. Instability regions in LEO compared to the 1999 catalogued population of intact objects (Kessler *et al.*, 2010).

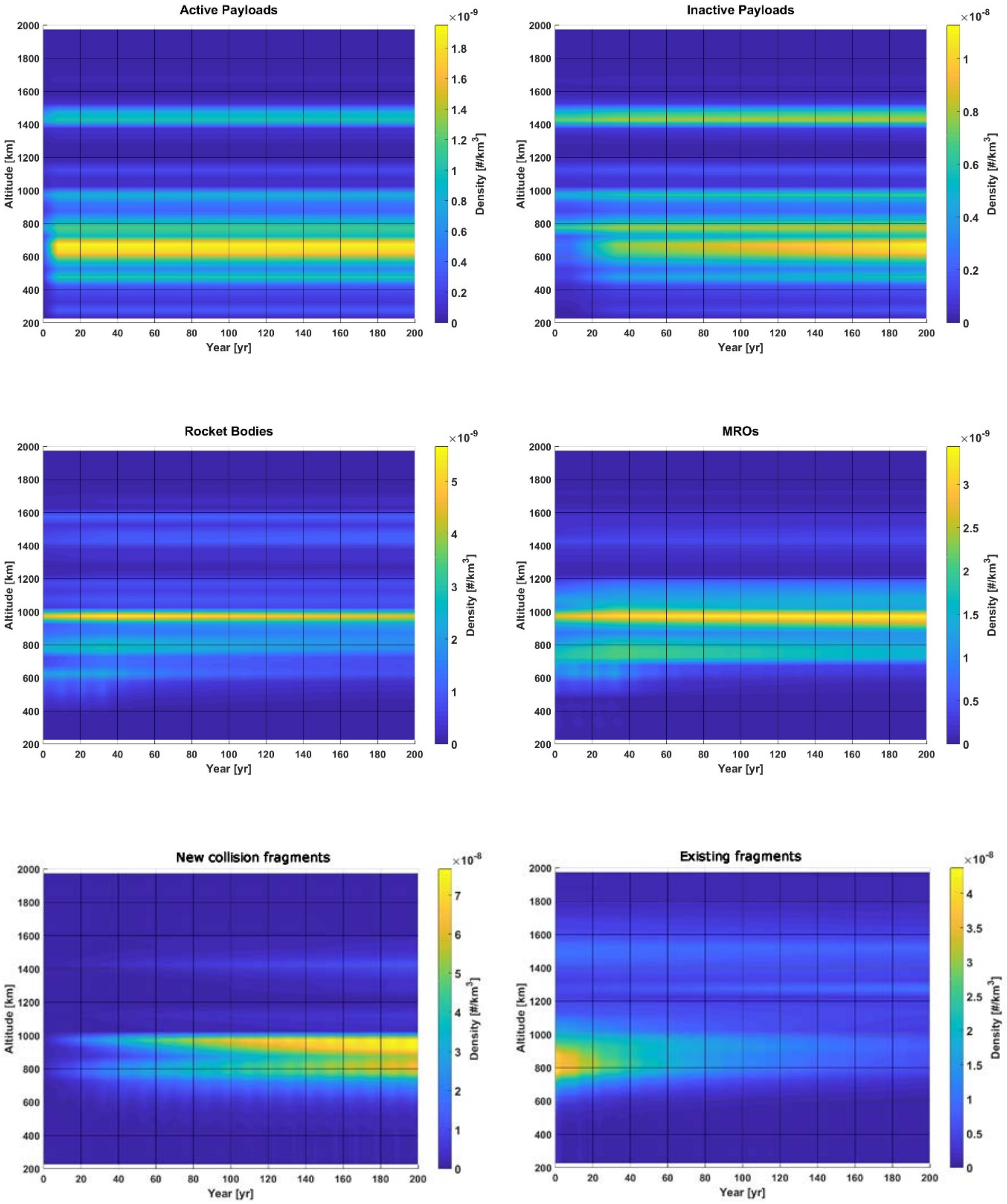

Figure 3-10. The evolution of orbital density for each species. Values were linearly interpolated from those computed at the middle point of each shell. Different scales are used to enhance the visibility of species-related trends.

An insight into the evolution of the spatial density of each species is given in Figure 3-10. Each graph has a different density scale to enhance the trends present in each species. In general, the values are one or two orders of magnitude smaller than the total spatial density (Figure 3-8). Comparing Figure 2-21 with Figure 3-10, it can be seen that payloads, rocket bodies and MROs accumulated in shells where there were more launches. The dynamics of the total density was dictated by newly generated collision fragments and, in a minor way (approximately one order of magnitude), by inactive payloads, which accumulated over time at various altitudes.

Rocket bodies and MROs had a similar evolution; their density remained in both cases almost constant during the whole simulations due to the quasi-equilibrium of new launches performed with decayed objects. The active payloads also evolved similarly; however, their amount increased in the first eight years of the simulation due to the newly launched active payloads. This increase ceased when the first payloads were moved into the inactive species, reaching a new equilibrium with the new payloads launched. The same accumulation phenomenon occurred in the inactive species. In this case, the process started only after the first payloads became inactive (i.e. after 8 years) and continued for 25 years. Then the rate reduced due to the inactive payloads being removed from the simulations. However, 10% of them were not compliant with PMD measures and accumulated over time.

Existing and newly formed fragments had different trends. The former decayed over time due to the cleansing action of the atmospheric drag, while the latter increased due to new fragmentation events that took place among the increasing number of objects in orbits. Indeed, their orbital density peaked between 800 and 1,000 km, where new launches were more frequent, and the cleansing effect of the drag was limited. The approach used for post-mission disposal generated inactive objects (that would thus produce additional collision fragments) that remained in the same shell of launch for a longer period instead of scattering over multiple shells at lower altitudes. Consequently, this approach generates errors in the population distribution, with an overestimation of the number of collision fragments at higher altitudes, which have a longer residual orbital life. For solving this issue, a different approach was also tested (and is presented in Section 5.2), with the implementation of the spacecraft relocation in lower orbits at the end of their operative life.

3.4. Sensitivity analysis

Space debris models are based on several assumptions, which influence the model behaviours and results. Sometimes even a change of a few percentage points in the simulation variables can lead to important variation in the evolution of the orbital population. Some variables might have a wide uncertainty (e.g. the uncatalogued space debris population and the objects’ cross-sectional areas) or just cannot be accurately predicted due to their stochastic nature (Dolado-Perez, Pardini and

Anselmo, 2015). Some of these variables, mostly linked to physical parameters or behaviours, can be improved at least partially by increasing our knowledge of the subject. For example, the solar and the atmospheric density models can be revised to enhance (but not to completely forecast) the solar activity and re-entry predictions, or more observing campaigns can be performed to increase the knowledge and evaluation accuracy on the size of the actual debris population. A second group of variables relates directly to the simulation assumptions and are, for example, the future launch rate, the satellite operational life, the Post Mission Disposal (PMD) compliance level and the residual orbital lifetime (i.e. the time needed by the object to re-enter the atmosphere after the end of its mission to adhere to mitigation guidelines). The analysis presented in this section will focus on the influence of some of the variables in this last group: the PMD compliance and launch rates.

3.4.1. Sensitivity to PMD compliance

Eleven simulations were performed to investigate the sensitivity of the model outcome to the adoption of post-mission disposal. They used the default model parameters (listed in Section 2.11) and a variable PMD compliance level, ranging from 0% to 100% (in steps of 10%).

Table 3-8. Summary of results for the sensitivity test on PMD compliance.

PMD compl. [%]	Intact objects	Existing Fragments	New Fragments	Total	Cumulative collisions
0%	11,718	4,495	35,223	51,436	176
10%	10,923	4,496	31,462	46,880	155
20%	10,126	4,496	27,961	42,582	137
30%	9,326	4,496	24,716	38,538	120
40%	8,525	4,497	21,722	34,744	105
50%	7,722	4,497	18,975	31,194	92
60%	6,917	4,497	16,471	27,885	80
70%	6,110	4,498	14,205	24,813	69
80%	5,302	4,498	12,173	21,973	60
90%	4,492	4,499	10,371	19,362	52
100%	3,680	4,499	8,795	16,974	45

The total number of objects at the end of the projection period varied depending on the PMD compliance, with a non-linear trend (Figure 3-11, and Table 3-8). As expected, the number of existing fragments at the end time was almost constant, since they are not subject to any mitigation rule. Their small variations (few units), was due to the variable number of collisions involving them (higher PMD compliance resulted in fewer collisions). The number of intact objects at the end time, composed by active and inactive payloads, rocket bodies and MROs, decreased linearly with the PMD compliance due mainly to the increased number of decayed spacecraft. Concerning the total spatial density, results and conclusions were similar to those presented in Section 3.3, with the level of compliance influencing the magnitude of the peaks (Figure 3-12).

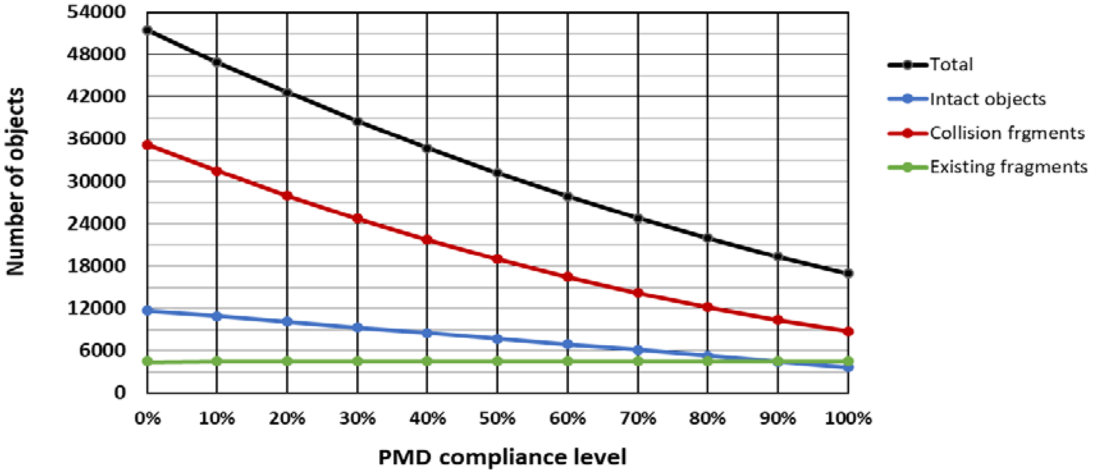

Figure 3-11. The total end populations as a function of the PMD compliance.

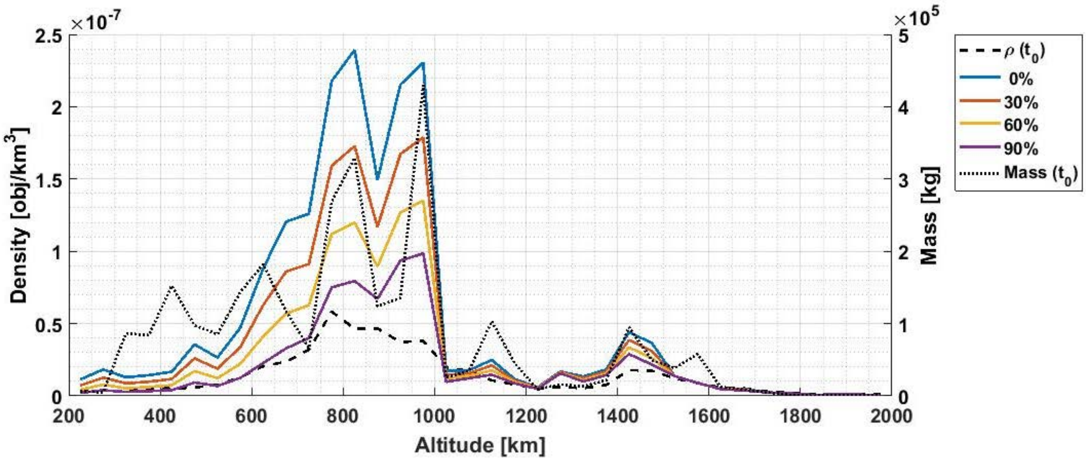

Figure 3-12 The total spatial density after 200 years as a function of PMD compliance level. The initial densities and mass distributions are also reported.

Lastly, as expected, the collision fragments had a quadratic relationship with the PMD compliance, given that the collision rate is proportional to the square of the number of objects in each shell (see Equation (2.20) in Section 2.3). The quadratic relationship with the collision probability is seen (approximately) in the real world as well, but this result should be further verified independently with different models .

It is possible to enunciate mathematical formulas that approximate the relationship between the intact, explosion and collision fragments and PMD compliance (with a coefficient of determination $R^2 > 0.99$).

For the explosion fragments this formula was found:

$$N_{EX}(t_{end},\lambda) = (7.7\cdot 10^{-4}\lambda + 1)N_{EX}(t_{end},0)\,, \tag{3.1}$$

where $\lambda \in [0;1]$ is the level of compliance with PMD (from 0 to 1) and $N_{EX}(t_{end},0)$ is the collision fragment population at the end time with a 0% compliance. The partial derivative along λ yields

$$\frac{\partial N_{EX}(t_{end},\lambda)}{\partial \lambda} = 7.7\cdot 10^{-4} N_{EX}(t_{end},0)\,, \tag{3.2}$$

and gives a direct measure of the variation on how the explosion fragments vary with the compliance level. As highlighted by the coefficient of N_{EX} and as visible in Figure 3-11 (i.e. the green curve), the existing fragments are almost not sensible to the variation of the PMD compliance, since they are objects launched in the past. However, this term is not null, and its very small value is caused by a few objects that are prevented from getting involved in collisions when there is higher compliance.

A similar expression could be found for the intact objects, i.e. rocket bodies, active and inactive payloads (with $R^2 > 0.99$):

$$N_I(t_{end},\lambda) = (-0.68\lambda + 1)N_I(t_{end},0)\,, \tag{3.3}$$

$$\frac{\partial N_I(t_{end},\lambda)}{\partial \lambda} = -0.68 N_I(t_{end},0)\,, \tag{3.4}$$

In this case, intact objects have a direct relationship with PMD compliance: an increase in the compliance will result in a decrease in the end population. For example, if $N_I(t_{end},0) = 10000$, for every 10% increase in PMD compliance, the end population will decrease by about 680 objects.

Lastly, concerning the number of collision fragments and its partial derivative along λ, more complex relationships were found:

$$N_{CO}(t_{end},\lambda) = (0.35\lambda^2 - 1.10\lambda + 1)N_{CO}(t_{end},0) \tag{3.5}$$

$$\frac{\partial N_{CO}(t_{end},\lambda)}{\partial \lambda} = (0.70\lambda - 1.10)N_{CO}(t_{end},0)\,. \tag{3.6}$$

In this case, the collision fragments also have a positive quadratic relationship with λ (i.e. the PMD compliance). Eq. (3.6) tells us that the benefits from increasing the PMD compliance are not constant but decreases with higher λ. Even if not constant, being $\lambda \in [0;1]$, the coefficient of $N_{CO}(t_{end},0)$ remains always negative, i.e. there is always a decrease in the end population of collision fragments when increasing the PMD compliance.

Lastly, the same analysis can be carried out on the total end population ($R^2 > 0.99$) and its derivative along λ:

$$N_T(t_{end},\lambda) = (0.24\lambda^2 - 0.91\lambda + 1)N_T(t_{end},0)\,, \tag{3.7}$$

$$\frac{\partial N_T(t_{end},\lambda)}{\partial\lambda} = (0.47\lambda - 0.91)N_T(t_{end},0)\,. \tag{3.8}$$

Alternatively, Eq. (3.7) can be expressed as the sum of Eqs.(3.1), (3.3) and (3.5), as a function of the initial population of the single species, while the derivative in Eqs. (3.2), (3.4), and (3.6) can be used to individuate the influences of each population.

Similarly, it was found that the number of total collisions at the end time and its variation can be expressed by ($R^2 > 0.99$):

$$\mathrm{n}_c(\mathrm{t}_{end},\lambda) \; = \; (0.439\lambda^2 - \; 1.179\lambda + 1)\cdot \mathrm{n}_c(\mathrm{t}_{end},0)\,, \tag{3.9}$$

and

$$\frac{\partial n_c(t_{end},\lambda)}{\partial\lambda} = \; (0.877\lambda - \; 1.179)\cdot \mathrm{n}_c(\mathrm{t}_{end},0)\,. \tag{3.10}$$

The same conclusions drawn from Eq. (3.6) and (3.7) are valid also for Eq. (3.10) and (3.11): a decrease in the total number of collisions is always present when increasing the PMD compliance.

3.4.2. Sensitivity to the launch rate

This section investigates the influence of different launch rates in LEO to understand their long-term effect on the evolution of the orbital population. A part of this study was recently published in *Acta Astronautica*, where analysis on the launch profile were also reported (Somma, Lewis and Colombo, 2019). The focus on various launch rates is also of interest considering recent proposals by several private companies (e.g. Boeing, OneWeb, Planet Labs, Samsung, SpaceX) to deploy new large constellations in LEO. Therefore, different launch rates and distributions may simulate the build-up and the replenishment of such orbital constellations (see Chapter 5).

In this analysis, four scenarios were compared to a reference case that used the default launch rate (Section 3.3) here re-defined as $\dot{L}^* \triangleq \dot{L}(t,h)$. The four cases were: no-launches, half the reference launch rate, i.e. $0.5\dot{L}^*$, one-and-one-half times the launch rate, i.e. $1.5\dot{L}^*$, and twice the launch rate, i.e. $2.0\dot{L}^*$. The other simulation parameters were the same as the reference in Section 3.3, including the PMD compliance, which was set to 90%.

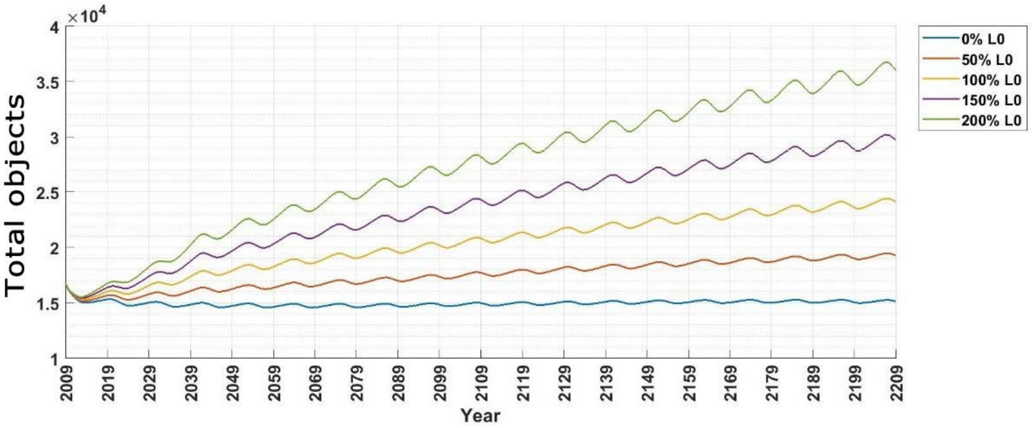

Figure 3-13. Comparison of the total end population for various multipliers of the reference launch profile $\dot{L}^*(h)$. The population decreases only with no new launches ($0\%\dot{L}^*$)

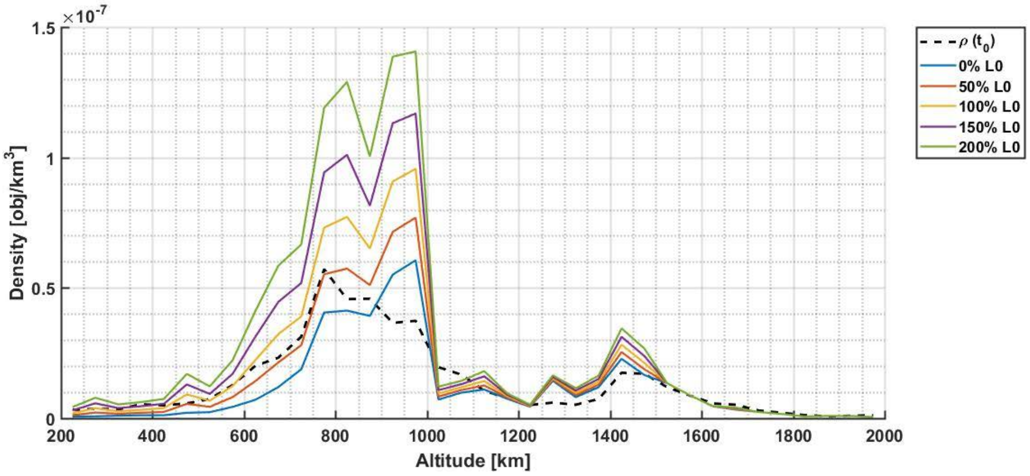

Figure 3-14. The spatial density at initial and end time as a function of altitude and of the multipliers of the reference launch profile $\dot{L}^*$.

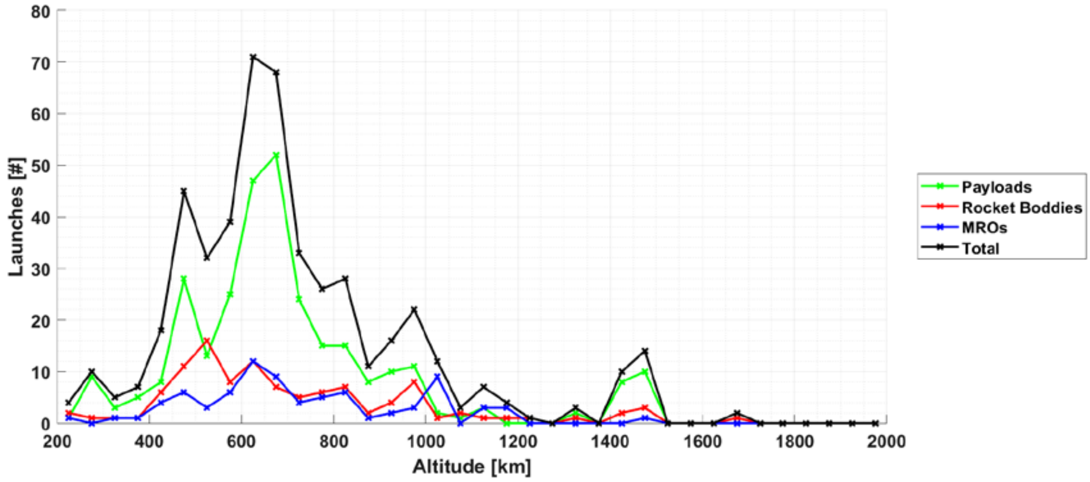

Figure 3-15. Spatial distribution of the reference 8-yr launch profile $\dot{L}^*$.

The no-launches scenario was the most optimistic case, and it revealed a peak in spatial density in the 900-1,000 km region. Indeed, even though this was the only case in which the total end population was smaller than the initial population (-9.9%, Figure 3-13), the spatial density reached values higher than the initial one in several shells (Figure 3-14). A behaviour similar to the reference case with $\dot{L}^*$ was also observed in the other cases, with increasing density values, with local maxima in the 750-850 km region and attaining the absolute maximum value in the 950-1,000 km region. In the region of 1400-1500 km, the maximum spatial density increased with the launch profile multiplier as well, but it always assumed values smaller than 0.5×10^{-7} objects/km^3.

The results, confirming the findings reported in Section 3.3, suggested that three regions are particularly critical within LEO. The first one lied at 750-850 km, where today's debris population causes a future increase in spatial density. The lowest part of this region reached a population size and spatial density lower than the initial ones only in the extreme case of completely stopping the launch activity and using for all the existing intact objects a 90% compliance with post-mission mitigations guidelines. The second region lied at 900-1,000 km, where a high number of big and massive objects resided at the initial time and launched objects accumulated over time (Figure 3-15). In this region, drag was not sufficient to maintain a balance between injected and decaying objects, even in the no-launch scenario. Moreover, the spatial density of this region increased over time, becoming the highest in LEO. The third region extended from 1400 to 1500 km. Here the initial population was low, but the launch profile had a relative peak, and the effect of drag was negligible. Therefore (presuming that no additional measures were taken) any additional object that reached orbit in this region contributed to the build-up of the orbital population.

The effects of the so-called Kessler syndrome (Kessler and Cour-Palais, 1978) were present with the breakup fragments becoming, in the long-term the major flux in specific LEO region (and exceeding the natural meteoroid flux) even in the case of no-future launches (Kessler and Anz-Meador, 2001).

Table 3-9. The numerical results of the sensitivity study on the launch rate, with the third case corresponding to the reference one. The maximum density (achieved among all altitude shell) always happened in the 950-1,000 km shell.

Multiplier of $\dot{L}^*$	$N(t_{end})$	**Total collisions**	$\rho_{\max}$ **[#/km^3]**	$t(\rho_{\max})$ **[yr.]**	$\rho_{\max}(t_{end})$ **[#/km^3]**
0	15,147	35	6.91 10^{-8}	2107	6.06 10^{-8}
0.5	19,295	51	8.20 10^{-8}	2140	7.69 10^{-8}
1.0	24,139	74	9.87 10^{-8}	2173	9.57 10^{-8}
1.5	29,713	103	1.20 10^{-7}	2206	1.17 10^{-7}
2.0	36,050	141	1.44 10^{-8}	2207	1.41 10^{-7}

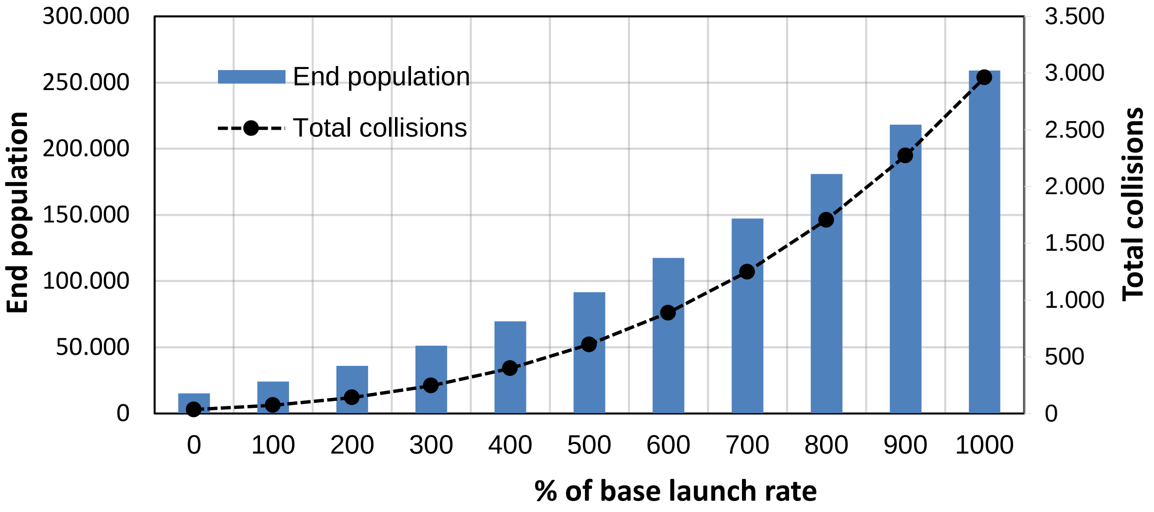

Figure 3-16. The non-linear relationship among the launch rate, the end population, and the total cumulative number of collisions for an extended set of simulations (up to a ten-fold increase in the launch activity).

A not linear relationship resulted between the number of objects in the end population and the number of collisions with the launch rate (Table 3-9). Indeed, when extending the simulations up to a ten-fold increase in the launch activity ($10\dot{L}_0$), a quadratic trend is visible due to an increasing number of both targets and newly generated fragments that act as projectiles (Figure 3-16).

In particular, the following relationships were found (both with $R^2 > 0.99$):

$$\mathrm{n}_c(\mathrm{t}_{end},\mathrm{k}_L) = (1.01\mathrm{k}_L{}^2 - 1.46\mathrm{k}_L + 1)\cdot \mathrm{n}_c(\mathrm{t}_{end},0), \tag{3.11}$$

$$N_T(\mathrm{t}_{end},\mathrm{k}_L) = (0.118\mathrm{k}_L{}^2 + 0.424\mathrm{k}_L + 1)\cdot N_T(\mathrm{t}_{end},0), \tag{3.12}$$

where $\mathrm{n}_c(\mathrm{t}_{end},\mathrm{k}_L)$ is the total number of collisions at the end time, $\mathrm{N}_T(\mathrm{t}_{end},\mathrm{k}_L)$ the total end population, and k_L is the multiplier of the reference launch rate. The variation of the two quantities was obtained deriving along k_L:

$$\frac{\partial n_c(t_{end},\mathrm{k}_L)}{\partial k_L} = (2.02\mathrm{k}_L - 1.46)\cdot \mathrm{n}_c(\mathrm{t}_{end},0), \tag{3.13}$$

$$\frac{\partial N_T(t_{end},\mathrm{k}_L)}{\partial k_L} = (0.236\mathrm{k}_L + 0.424)\cdot N_T(\mathrm{t}_{end},0). \tag{3.14}$$

In this case, the equation found were similar to Eq. (3.8) and (3.10). However, in this case, we have k_L always positive since we are injecting new objects in the environment. Therefore, as expected, the number of collisions and total end population tend to increase with it.

The used a 2nd order polynomial curve fit the collisions has a $R^2 = 0.9966$. Nevertheless for $\mathrm{k}_L \leq 0.72$ from Eq. (3.14) it results $\partial n_c(t_{end},\mathrm{k}_L)/\partial k_L \leq 0$. From a mathematical point of view, this indicates the threshold for which the number of collisions decreases as a function of the launch activity. However, we know from previous results that this is not true (Table 3-9). This issue can easily be solved using a higher polynomial fit, such as a 3rd degree polynomial ($R^2 > 0.9999$), where, as expected, all the coefficients are positive:

$$\mathrm{n}_c(\mathrm{t}_{end},\mathrm{k}_L) \; = \; (0,315\mathrm{k}_L{}^3 + 0.183\mathrm{k}_L{}^2 + 0.996\mathrm{k}_L + 1)\cdot \mathrm{n}_c(\mathrm{t}_{end},0)\,, \tag{3.15}$$

Indicating therefore that the number of collisions always increases when injecting new objects in the environment.

3.5. Conclusions

Several studies were performed using the MISSD model to tune the model and test the sensitivity of the LEO population to the number of altitude shells, integrator time step, launch rate and launch profile. Based on the results of the test performed, the default value for the integrator timestep was set to 0.1 years, while the default number of shells was set to 36.

The results highlighted the importance of adopting high level of compliance with PMD since even a small increase in their adoption could benefit the whole space environment, as demonstrated by its quadratic relationship with the collision fragments, which became the predominant species in the majority of simulations after 75 to 100 years (depending on the compliance level). A quadratic relationship was also derived to link the end total population and the number of collisions with the multiplier of the launch rate and the PMD compliance. Concerning these two quantities, both were expressed in the form of

$$y = ax^2 + bx + c = \left(\frac{a}{c}x^2 + \frac{b}{c}x + 1\right)c\,, \tag{3.16}$$

and

$$y' = \left(\frac{2a}{c}x + \frac{b}{c}\right)c = 2ax + b\,. \tag{3.17}$$

Computing the terms $2a$ and b, it is, therefore, possible to compare the effects of the multiplier of the launch rate and of the PMD compliance on the total population and the number of collisions at the end time (Table 3-10).

Table 3-10. The coefficients of the quadratic formula obtained for the end total population and the number of collisions as a function of the PMD adoption and launch rates multiplier.

Entity	**Case**	**2a/c**	**b/c**	**c**	**2a**	**b**
Total end pop.	PMD	0.474	-0.907	51463	24,404.0	-46,654.0
Total end pop.	Launches	0.237	0.424	15147	3,584.8	6,419.2
Cumul. collisions	PMD	0.877	-1.179	175.9	154.3	-207.4
Cumul. collisions	Launches	2.020	-1.462	35.2	71.0	-51.4

The performed sensitivity analysis demonstrated that in MISSD the variation of the LEO population in response to changes in PMD compliance and launch rates (which are two of the major sources of uncertainty in LEO) affected only the magnitude of the LEO population but not the overall dynamics of the environment.

Chapter 4. Increasing the ADR effectiveness

This chapter illustrates analysis performed with the proportional, linear and quadratic control laws described in Section 2.8 (Somma, Lewis and Colombo, 2017, 2018a).

The model and the controller are used to evaluate the evolution of the LEO population in different scenarios and to measure the effectiveness of different level of PMD compliance and active debris removal rates. Section 4.1 and 4.2 present respectively the analysis with the proportional and the linear control laws, with the removal rates that varied through time and were bounded to a maximum rate set at the beginning of each simulation. A deeper analysis with the more recently developed quadratic control laws is also illustrated in Section 4.3. Lastly, a summary is reported in Section 4.4, while an additional discussion of the results is given in Chapter 6.

4.1. Proportional control law

This section presents the analysis performed with a proportional control law on the total population presented in Section 2.8.1. This was the first control law developed, and the derived experience was used as a base for the other ones. Even if the performances are lower than with the other laws, it presents useful insights into the development process of the controller and its functioning.

The equation (2.57) was used, with 2020 as the starting year for ADR, and 25 removals as its maximum annual value. This value might appear high at the current time; however, it was assumed that as soon as the ADR technology would progress, multiple mission could be accomplished in the same year or multiple removals can be performed by a single removal platform (Barea, Urrutxua and Cadarso, 2019). Previous studies demonstrated that a lower value limit (usually below 10) would be sufficient to prevent the exponential growth of the LEO population, with values up to 20 annual removals also tested (Liou and Johnson, 2009; Liou, Johnson and Hill, 2010; White and Lewis, 2014a). Setting up a higher value, allowed to simulate a wide range of scenarios with different (sub-optimal) strategies, while at the same time maintaining a finite upper limit for the controller before reaching its saturation point. The maximum annual removal rate was automatically used when the total number of objects reached 120% of the value in the starting ADR year. The initial population and the launch traffic from the MASTER 2009 database (Oswald *et al.*, 2005; Flegel *et al.*, 2011) were projected to 2013, the start year of this 200-yr simulation, and a 90% compliance with PMD was used. This analysis did not implement the solar cycle and did not use the default initial population, being performed earlier with different data available with respect to the other presented analysis on the controller. However, it was decided to include it to present an example of the possible analysis and results that can be carried out with the proportional controller. Even if numerically affected (in the order of few percentage points), the outputs would show the same dynamics, and therefore the draws conclusions would remain valid (compare Figure 4-1with Figure 3-7 in Section 3.3).

A scenario with no controller was run as a benchmark case (Table 4-1, Figure 4-1). Results reported that, after an initial rise, the number of intact objects reached a plateau, thanks to the high level of PMD compliance, even though this measure acted from 2046. This date is equal to the starting date, 2013, plus eight years of operative lifetime and 25 years needed for the first object to decay. The number of existing fragments decreased during all the simulation due to drag, while collision fragments became the dominant species after 80 years (as already seen in Section 3.3).

Table 4-1. The composition of the end time population and percentage variation in the benchmark case.

Object species	Initial population	End population	Variation [%]
Intact objects	3,503	4,188	+ 19.56
Existing fragments	12,275	4,169	- 66.04
New fragments	0	15,253	-
Total	**15,778**	**23,610**	**+ 49.64**

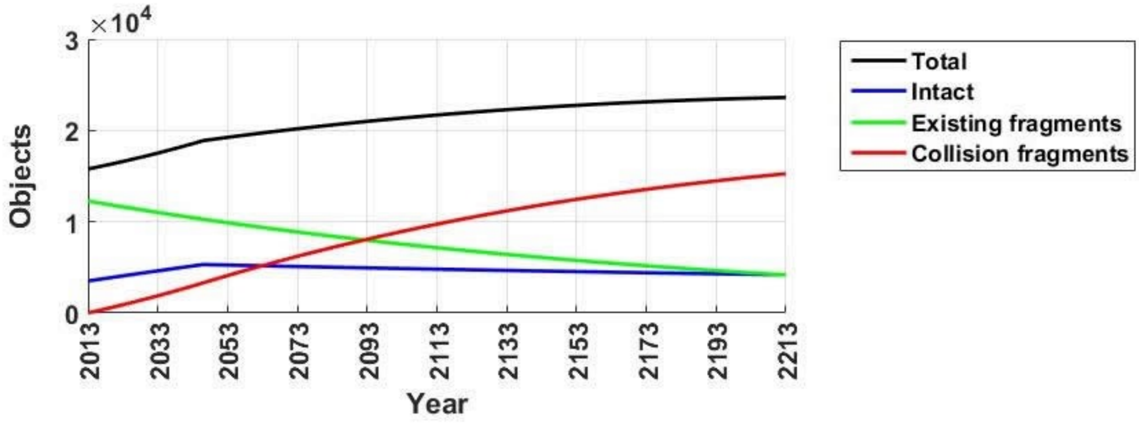

Figure 4-1. LEO population projection with population breakdown for the benchmark case.

In the simulation with ADR, starting in 2020, the controller adjusted the removal rate as a function of the total population (Figure 4-2). Having a linear increase in the number of objects, the controller commanded an increasing number of removals. The number of intact objects peaked 33 years after the starting of the simulations (8 years of which are operative time) when the PMD-compliant objects launched at the initial times were completely removed from the environment. At this time, the number of annual removals keep increasing, but with a slower pace, with the controller never saturated. After peaking in the 2080s, it slowly reduced its action, indicating an improvement in the total population. Ultimately, it automatically turned off the removals near the end of the simulation when the total population returned below the initial value. Thanks to the additional benefits of the ADR strategy, the newly generated collision fragments slowly reduced their rise to a dynamic equilibrium around 9,000, while the intact population benefited from the high level of PMD compliance. Toward the end of the simulations, the trends for the collision rate and for the number of each species objects had a plateau (Figure 4-2), while the total population at the end time was close to the initial one, with a decrease of -0.71% (Table 4-2).

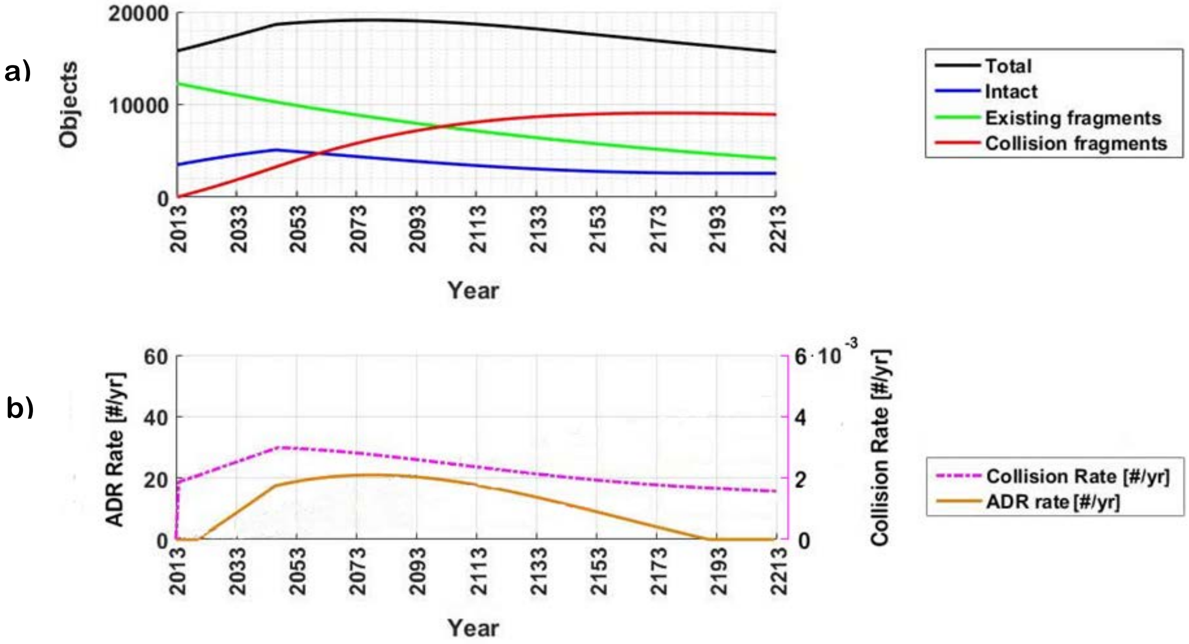

Figure 4-2. The evolution of the LEO population (top image), collision rate and removal rate (bottom) in the simulations with the proportional control law.

Table 4-2. Results of the simulations with the proportional control law.

Object species	Initial population	End population	Variation [%]
Intact objects	3,503	2,574	- 26.51
Existing fragments	12,275	4,169	- 66.04
New fragments	0	8,922	-
Total	**15,778**	**15,665**	**- 0.71**

Results highlighted that, as expected, the use of ADR reduced both the number of intact objects and new collision fragments while existing fragments were not affected because their presence depends mainly on the atmospheric drag.

The controller actively removed a total of 2,263 objects, achieving a total number of collisions equal to 45. The maximum annual removal rate was never achieved (i.e. the control never saturated) with a yearly average of 11.3 removals; a high value compared to other studies (White, 2014; White and Lewis, 2014a). This behaviour was most likely due to the lack of selection of the most dangerous object in the controller (i.e. those with the highest collision risk) from the environment, and to the very simple control law implemented that is not able to remove objects effectively. Indeed, results that used the other control law achieved better results with fewer removals.

4.2. Linear control law

The linear control law presented in Section 2.8.2 was used to test 52 scenarios with different combinations of PMD compliance levels, and of the maximum annual removal rates for inactive payloads and rocket bodies (u_{IP} and u_{RB}), ranging from zero to 25 removals/year. The threshold densities used in the control to set the maximum and minimum values for the controller were equal to $\rho_{\min} = 10^{-8}$ and $\rho_{Max} = 10^{-7}$ objects/km^3. This last value was selected as it was very close to the maximum density achieved in a single shell at the end time of the no ADR case (Figure 4-5). The initial population derived from the MASTER 2009 database (Oswald *et al.*, 2005; Flegel *et al.*, 2011), and PMD compliance levels were assumed equal to 0%, 30%, 60%, and 90%. The NERF effectiveness index was computed using 100% and 0% PMD compliance as the best and worst cases.

Because in this analysis one of the focus was to investigate how to achieve an end population similar but not extremely lower than the initial one, it was chosen to test a subset of all possible combinations of maximum removals depending on the PMD compliance level, with the initial hypothesis of about 5 less removal needed for every 30% increase in the compliance to reach similar end population. In following simulations, presented in Section 4.3, it was preferred to perform all the possible combination of removal rate for each PMD compliance level, in order to have a more complete set of results and a better big picture.

Table 4-3. Composition of the population at the end time and its percentage variation with respect to the initial time in the cases without ADR. The last row reports the NERF value at the end time.

PMD compliance	**0%**	**30%**	**60%**	**90%**
Intact objects	12,275 (+260%)	9,922 (+191%)	7,548 (+121%)	5,158 (+51%)
New fragments	43,012 (-)	31,428 (-)	22,153 (-)	15,040 (-)
Existing fragments	4,546 (-67%)	4,547 (-67%)	4,548 (-67%)	4,549 (-67%)
Total	59,833 (+250%)	45,897 (+168%)	34,250 (+100%)	24,747 (+45%)
NERF	**0.00**	**0.37**	**0.68**	**0.93**

The orbital population increased in all four scenarios that did not use ADR (Table 4-3). However, even with a 90% PMD compliance, the end population was still above the initial one, with a NERF of 0.93 (Table 4-3).

The total populations at end time for the 52 run scenarios are shown in Figure 4-3 with a colour map that helps to visualise the trends. This latter was obtained drawing a triangular mesh of the simulations results and then linearly interpolating values at the vertices. The four plots show triangular shapes due to the fixed sum of the maximum removal rate for rocket bodies and inactive payloads. Indeed, results with the same maximum annual removal rate lie on a line with 45-degree orientation, which could also represent external constraints, due for example to logistic (e.g. launch opportunities) and economic factors (e.g. the yearly-allowed budget and thus the number of missions).

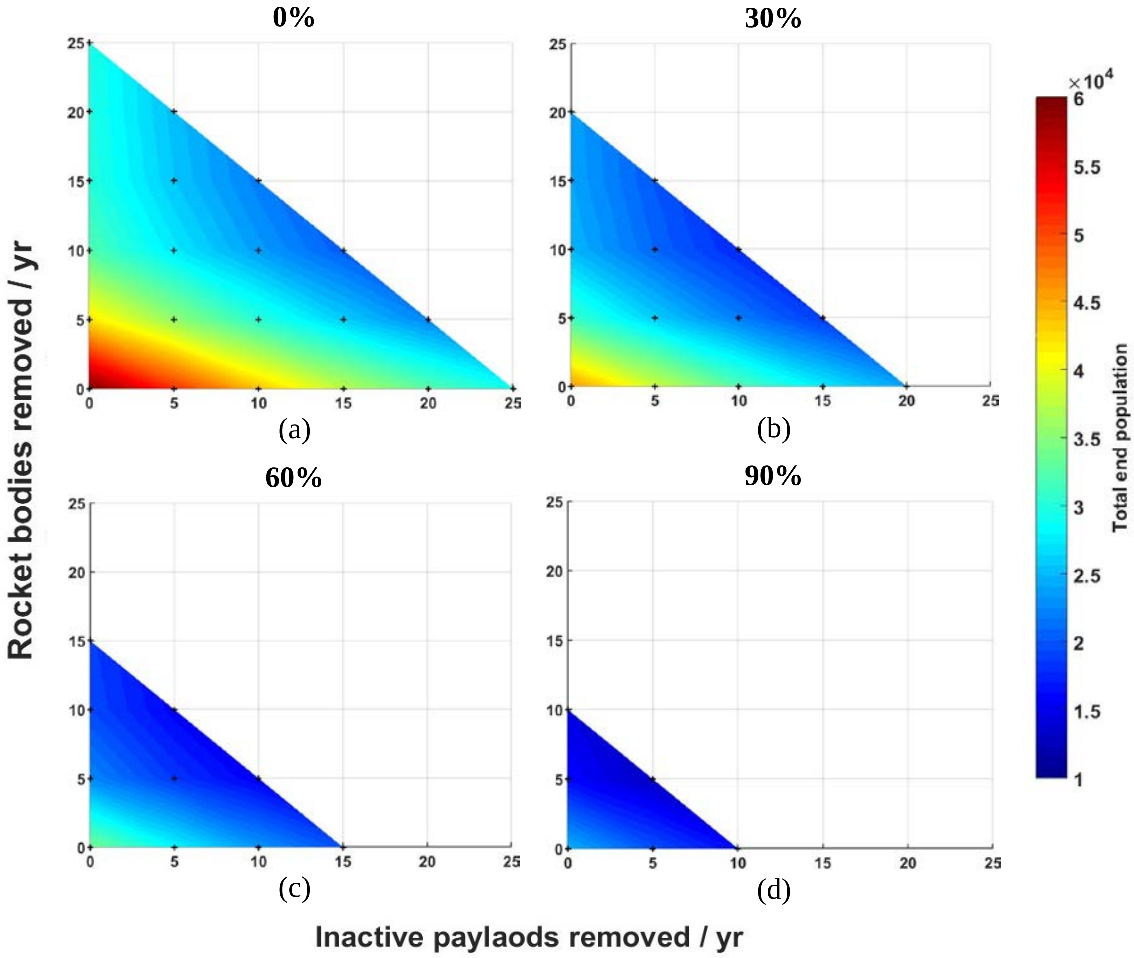

Figure 4-3. The total population at end time as a function of rocket bodies and inactive payloads actively removed and PMD compliance level. The colour map represents a linear interpolation of the results that are marked with a cross.

When fixing the PMD compliance level, the total population at end time varied greatly as a function of which species of objects was removed, as depicted by the asymmetric variation in colour, particularly visible in Figure 4-3a. Indeed, regardless of the PMD compliance, in all the cases with less than 15 annual removals, removing rocket bodies rather than inactive payload always achieved a lower end population (and therefore higher NERF). However, when increasing the number of annual removals, the lower population at end time were obtained with more balanced combinations of removals between the two species.

Indeed, acting on a single species led to the drop in that species population in the high-density shells but left untouched the other one, that in the long term was still able to produce collision fragments. For a low removal rate, the higher benefits were obtained removing only the more massive rocket bodies; while also removing inactive payloads was convenient only for strategies with 15 or more removals. In a shell with both the species, the most dangerous objects would be the rocket bodies, characterised by a high cross-section area (which increased the collision probability) and high mass (i.e. able to generate more fragments). However, considering a single shell, the controller is not able to discern which objects are more dangerous, and it would automatically select the removal rate accordingly to the relative densities regardless of their mass and area (Eq. (2.58)). A similar caveat appears more in general among shells because the model is not capable of discerning two different shells with the same number of objects but different mass. Nevertheless, the model considers the mass of the objects during the generation of the number of fragments and, therefore, the active removal of a rocket body prevents the generation of a higher number of fragments compared to the removal of an inactive payload, reflecting, therefore, the expected behaviour in the real world.

Higher compliance with PMD measures reduced the orbital population far better than using ADR, where the quantitative improvement depended on the selected values of PMD and ADR, as highlighted in Figure 4-3. For a fixed value of maximum removal rates, increasing the PMD compliance always resulted in a lower end population, as expected. However, when high removal rates were used, similar results can be achieved both with a high level of compliance and a low level of removals, or the opposite. For example, when using a 90% compliance with PMD measures and no removals, it yielded a total population of 24,747 objects (NERF = 0.93), while, when using 0% compliance and a combination of maximum 25 annual removals, the results ranged from 20,360 to 29,662 (NERF from 1.05 to 0.80).

Looking at some specific case that used a 90% PMD compliance, the evolution of the total population for six different combinations of removal rate for inactive payloads and rocket bodies, i.e. u_{IP} and u_{RB}, is depicted in Figure 4-4. The upper dotted curve represents the case with no removal. The two dashed lines depict the cases where the total number of annual removals is $u = u_{IP} + u_{RB} = 5$ while the solid lines illustrate the case of $u = u_{IP} + u_{RB} = 10$.

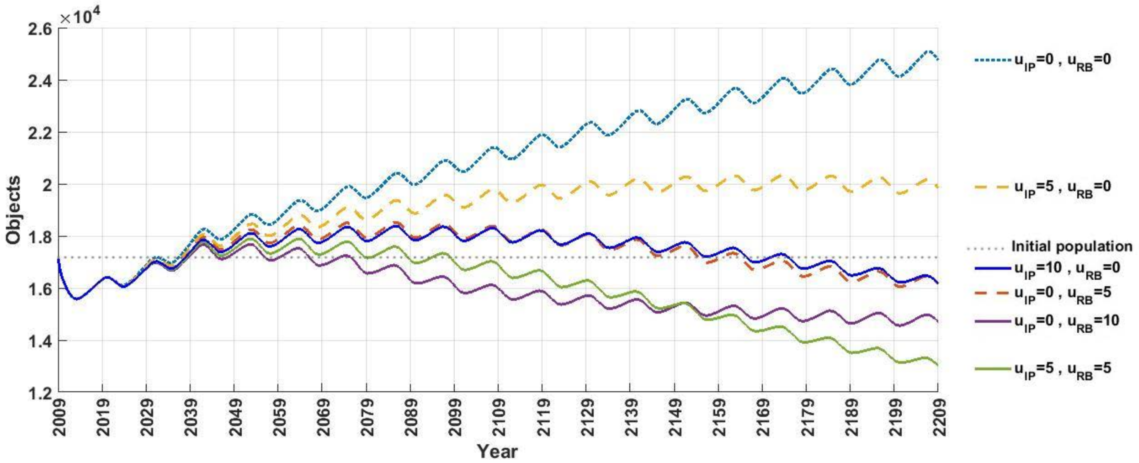

Figure 4-4. The evolution of the total population for six ADR strategies with 90 % PMD compliance and different combinations of u_{IP} and u_{RB}.

Results from simulations with the control operating on the rocket bodies had a higher NERF (Table 4-4) with respect to those where the control was only on the inactive payloads. Two different cases, the first one with $u_{IP} = 0$ and $u_{RB} = 5$, and the second one with $u_{IP} = 10$ and $u_{RB} = 0$, assumed similar values of the total population during the entire 200-yr timeframe, with their NERF values at the end time being almost identical: 1.16 and 1.15 respectively. The same happened for other values of PMD compliance as well, confirming that the effect of removing a single rocket body can be similar to removing two inactive payloads when using less than 15 total maximum annual removals. Further investigation on this subject, but with a quadratic control law, is carried out in Section 4.3.

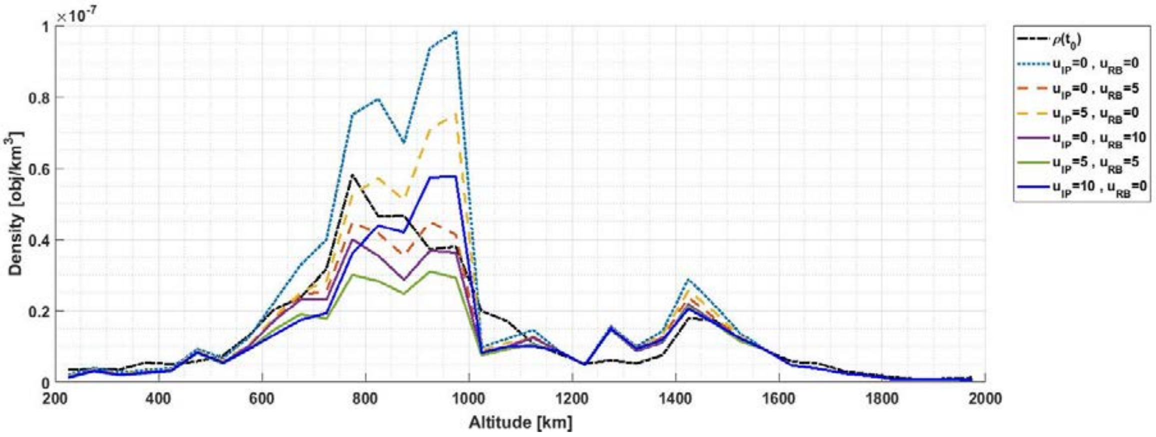

Figure 4-5. The spatial density at the end time of six ADR strategies with a different combination of u_{IP} and u_{RB}. All cases used a compliance level of 90% with PMD measures.

Table 4-4. Composition of the population and NERF at end time for six cases with the proportional controller and 90% PMD compliance.

u_{IP}	u_{RB}	**Total end population**	**NERF**
0	**0**	24,747	0.93
0	**5**	16,148	1.16
5	**0**	19,840	1.06
0	**10**	14,707	1.18
5	**5**	13,015	1.24
10	**0**	16,182	1.15

Figure 4-5 illustrates a comparison of the spatial density at the end time for different combinations of maximum annual removals of inactive payloads and rocket bodies with a 90% compliance with PMD measures. When no removal of rocket bodies was performed, the peaks in the 900-1,000 km region had a magnitude bigger than those in the lower 750-850 km region. Conversely, the removal of five rocket bodies per year was sufficient to have comparable maximum density peaks (at end time) in these two regions. Further considerations on the spatial density were already discussed in Section 3.3 (Figure 3-8) and will be discussed in Section 4.3.5 (Figure 4-12) and are omitted here to avoid repetition.

4.3. Quadratic control law on the partial densities

This section investigates the effectiveness of different combinations of mitigation and remediation practices in LEO, analysing and comparing the potential impact of ADR missions when using various levels of PMD compliance. Compared to the work presented in Sections 4.1 and 4.2, the analysis presented here used a quadratic control law and a diverse initial population. In addition, while in Sections 4.1 and 4.2 the removal rates were set to be variable with time, here the selected total annual removal rate was maintained fixed when the control was active (i.e. after the start year and when above the minimum density threshold), but the removals were distributed among different shells and species via the action of the controller.

All simulations used the default model parameters (Table 2-3). The levels of compliance with PMD guidelines tested were 0%, 30%, 60%, 90% and 100% (and always had a 100% success rate). The initial orbital population (Table 4-5) derived from the MASTER 2009 database (Oswald *et al.*, 2005; Flegel *et al.*, 2011), where all existing fragments were catalogued as explosion fragments (the model used the same average physical characteristics for both explosion and collision fragments). The quadratic controller on partial population densities presented in Section 2.8.3 was used, with the density thresholds, (which regulates the saturation of the density gain in each shell) equal to $\rho_{\min} = 10^{-9}$ objects/km^3 and $\rho_{Max} = 10^{-7}$ objects/km^3 (i.e. 1 and 100 objects in a cube with the side of 1,000 km). These thresholds were chosen due to its proximity to the maximum density reached at the end time of the no-removal case, equal to 9.57 10^{-8} objects/km^3 (see Figure 4-12).

The NERF index (Section 2.9) was used to evaluate and quantitatively compare the effectiveness of the combined actions of PMD and ADR in each strategy with respect to a best- and worst-case scenario run without ADR.

Table 4-5. The composition of the initial orbital population (derived from MASTER 2009). All existing fragments were catalogued as explosion fragments.

Object type	Initial population
Intact objects	**3,410**
Active satellites	191
Inactive satellites	1,716
Rocket Bodies	852
MROs	651
Fragments	**13,697**
Total objects	**17,107**

More than one hundred scenarios were run with different combinations of PMD compliance, and different annual removal rates for rocket bodies and inactive payloads, up to a total of 40 removals per year, with removals starting from 2020 (Table 4-6). This very high level of removals was set up in order to test a wider range of scenarios (compared to previous analysis) and verify what level of removal would be needed to achieve, for each PMD compliance, a population at end time equal or lower to a specific one, such as the initial one, which is equivalent to a NERF value of 0.77 (this value was obtained using the initial population in Eq. (2.64)).

Table 4-6. The tested values for annual removal rates and PMD compliance.

Parameter	Symbol	Annual removal rate [yr^{-1}]
Inactive payloads	u_{IP}	0, 5, 10, 15, 20
Rocket bodies	u_{RB}	0, 5, 10, 15, 20
Total removals	u	5, 10, 15, 20, 25, 30, 35, 40
Parameter		**Compliance**
PMD		0%, 30%, 60%, 90%. 100%

4.3.1. Benchmark effectiveness (best and worst- case with no ADR)

The benchmark effectiveness for six scenarios with no active debris removal was computed and used for numerical comparison for the cases with ADR (Table 4-7, Figure 4-6). The worst-case scenario was selected with a 0% PMD compliance, while the best-case used 100% compliance and had the collisions disabled. This latter case did not represent a realistic scenario but rather an ideal one where all collision could be prevented (e.g. via collision avoidance or just-in-time avoidance). In the real world, mission anomalies and failures would lower the overall PMD success rate.

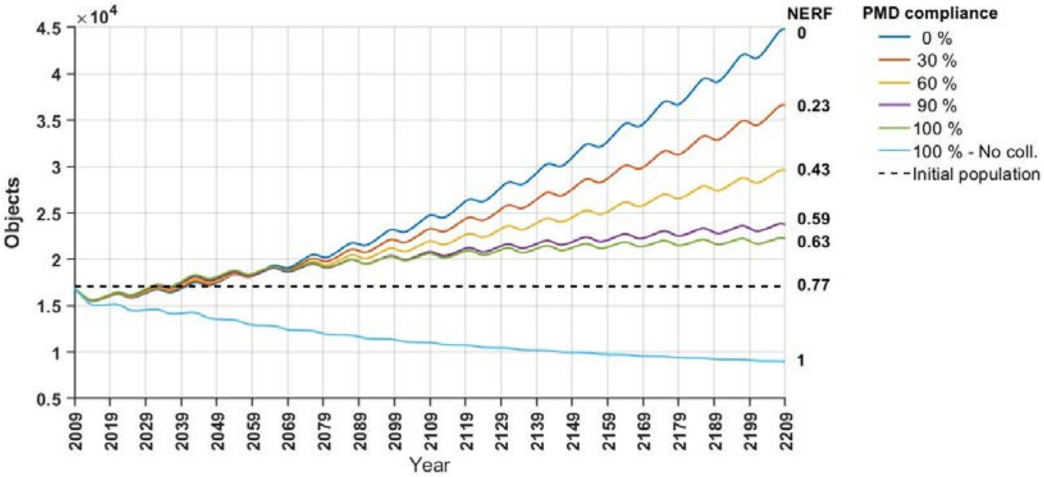

Figure 4-6. Comparison of the evolution of the LEO population when using different PMD compliance and no removals. The NERF at end time is also reported for each case.

Table 4-7. The end-time populations (and their percentage variations with respect to the initial time) and NERF values as a function of the PMD compliance level.

PMD compliance	**Intact objects**	**Fragments**	**Total**	**NERF**
0%	7,218 (+112%)	37,559 (+174%)	44,776 (+162%)	0.00
30%	6,319 (+85%)	30,276 (+121%)	36,595 (+114%)	0.23
60%	5,432 (+59%)	24,134 (+76%)	29,566 (+73%)	0.43
90%	4,545 (+33%)	19,194 (+40%)	23,738 (+39%)	0.59
100%	4,359 (+28%)	17,853 (+30%)	22,212 (+30%)	0.63
100%, no collisions	4,437 (+30%)	4,571 (-67%)	9,008 (-47%)	1.00

Moreover, not all collisions could be prevented with the current technology, such those among non-operational or uncatalogued objects. These six scenarios were characterised by an increase in the total orbital population, with the exclusion for the ideal best-case. Even in the second-best-case, i.e. with a 100% compliance, the end population remained well above the initial one, with a 30% increase (Table 4-7), while in the other cases the increase ranged from linear to exponential (with 0% compliance).

4.3.2. Different strategies, the same evolution

In general, multiple strategies were able to achieve similar evolution and end populations (and thus NERF, see Table 4-8), as depicted by the overlap of the solid red curve with the dotted black curve in Figure 4-7, where the upper curve represents the case with no removals. These results resemble those presented in Section 4.2 and, even if the numerical values were different due to the action of a different controller, the dynamics were similar, and the same conclusions were found (see Section 4.2).

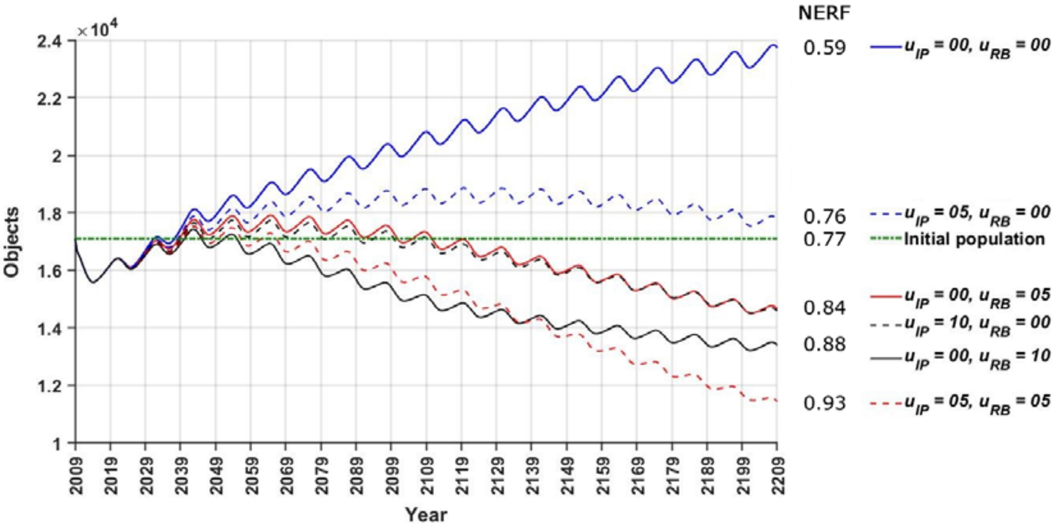

Figure 4-7. The evolution of the total population and NERF values for six strategies with 90% compliance with PMD guidelines and ADR on inactive payloads (u_{IP}) and on rocket bodies (u_{RB}). Multiple strategies ($u_{IP} = 0$ and $u_{RB} = 5$, $u_{IP} = 10$ and $u_{RB} = 0$) produced a similar outcome during the timeframe.

Due to the different control laws used, the two studies had a different amount and spatial and temporal distribution of the removed objects, but with the quadratic controller, the end population achieved lower values with the same maximum annual rates (compare Figure 4-4 with Figure 4-7).

Table 4-8. The NERF values obtained with various level of PMD compliance.

0% PMD compliance

u_{IP} u_{RB}	**0**	**5**	**10**	**15**	**20**
0	0.00	0.27	0.47	0.57	0.63
5	0.50	0.66	0.77	0.84	0.88
10	0.69	0.82	0.89	0.93	0.96
15	0.73	0.85	0.92	0.96	0.98
20	0.74	0.86	0.93	0.98	0.99

(a)

30% PMD compliance

u_{IP} u_{RB}	**0**	**5**	**10**	**15**	**20**
0	0.23	0.47	0.62	0.70	0.75
5	0.65	0.78	0.87	0.91	0.94
10	0.77	0.88	0.94	0.98	1.00
15	0.79	0.90	0.96	0.99	1.01
20	0.80	0.90	0.97	1.00	1.01

(b)

60% PMD compliance

u_{IP} u_{RB}	**0**	**5**	**10**	**15**	**20**
0	0.43	0.63	0.75	0.80	0.84
5	0.76	0.87	0.93	0.96	0.99
10	0.83	0.93	0.98	1.00	1.02
15	0.84	0.94	0.99	1.02	1.03
20	0.85	0.94	1.00	1.02	1.03

(c)

90% PMD compliance

u_{IP} u_{RB}	**0**	**5**	**10**	**15**	**20**
0	0.59	0.76	0.84	0.89	0.90
5	0.84	0.93	0.98	1.00	1.02
10	0.88	0.96	1.01	1.02	1.04
15	0.89	0.97	1.01	1.03	1.04
20	0.89	0.98	1.02	1.04	1.05

(d)

100% PMD compliance

u_{IP} u_{RB}	**0**	**5**	**10**	**15**	**20**
0	0.63	0.79	0.87	0.91	0.92
5	0.86	0.94	0.99	1.02	1.03
10	0.89	0.97	1.02	1.04	1.05
15	0.90	0.98	1.03	1.05	1.06
20	0.90	0.98	1.03	1.06	1.06

(e)

100% PMD compliance + no coll.

u_{IP} u_{RB}	**0**
0	1.0

(f)

4.3.3. Actively removing only one species at a time

When comparing the performances of strategies that removed only one object species at a time, those which removed only rocket bodies achieved a higher NERF score except with 15-20 removals and a PMD compliance above 90%, where however the differences in effectiveness are minimal (see Table 4-8, and Figure 4-8,). Indeed, in a breakup event, large and heavy rocket bodies are able to create a higher number of fragments compared to the smaller and lighter payloads.

In particular, the NERF values obtained for a selected rate of inactive payloads actively removed (e.g. $u_{IP} = 10$ or $u_{IP} = 20$, and $u_{RB} = 0$) were similar to those obtained with half that removal rate of rocket bodies ($u_{RB} = 5$ or $u_{RB} = 10$, and $u_{IP} = 0$), confirming that removing a single rocket body was as effective as removing two inactive payloads. Comparing the NERF scores in the first row with those in the first column in Table 4-8, it can be deduced that this effect occurred regardless of the PMD compliance levels.

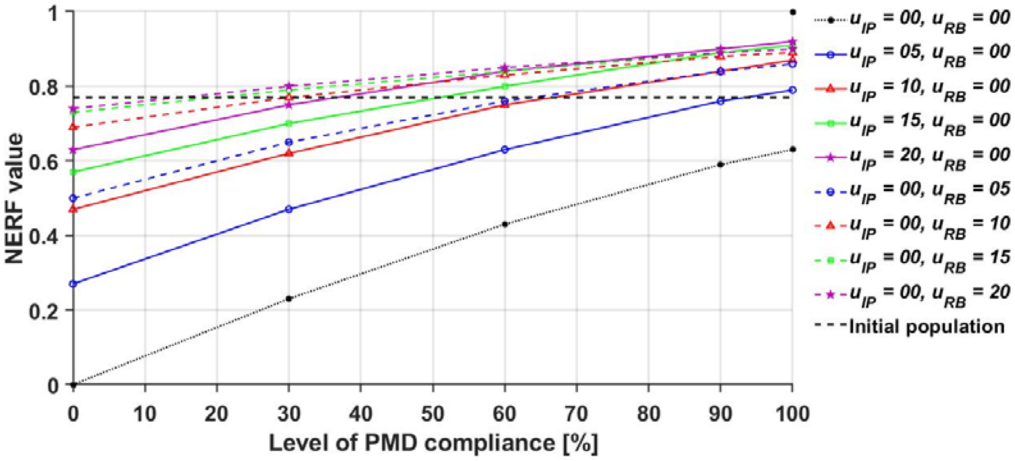

Figure 4-8. NERF values vs the PMD compliance level for six no-removal cases and for eight strategies that remove inactive payloads only (solid lines) and rocket bodies only (dashed lines). Except for very high removal values and PMD compliance, higher NERF were obtained performing ADR on rocket bodies only.

4.3.4. The non-linear effectiveness of ADR and PMD

In general, the effectiveness increased (and thus the end population decreased) with the removal rates and the PMD compliance level (Figure 4-9). However, the trend was not linear and showed decreasing benefits: the higher the PMD compliance or the annual removal rate, the lower the additional benefits on the total population, and thus on the NERF values.

Increasing the PMD compliance and maintaining constant the annual removal rate, a lower number of inactive intact objects were produced (by the spacecraft non-compliant with PMD), and therefore fewer catastrophic collisions occurred. These result in fragments that are linked to intact objects by a quadratic relationship (see Figure 3-11 and Equation. (3.1) in Section 3.3).

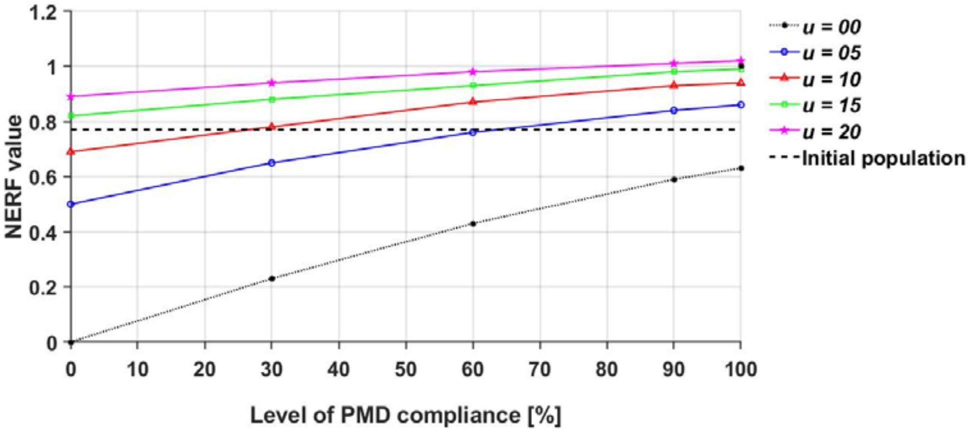

Figure 4-9. The maximum NERF value achievable as a function of the total annual removal rate and PMD compliance.

Keeping constant the PMD compliance level and removing the first 5 or 10 objects resulted in strong benefits with an increase in effectiveness up to 0.50 compared to the no-ADR case (Table 4-8). The marginal efficiency of any additional removal decreased, with the higher benefits (per unit of removal) achieved when removing the first objects, as seen with other models in (Liou and Johnson, 2009; White and Lewis, 2014b).

However, even if the final effect (i.e. the diminishing effect of each additional removal) is the same as other models, the cause is different: this is not due to the removal of specific objects with the higher danger index (e.g. heavy or large spacecraft). In general, the objects with more area and mass tend to be those higher in the risk/effect list, but this is also because they usually are in very congested regions (otherwise they might have a high effect but low collisions risk)

MISSD does not create a list of objects to be removed, and therefore it does not prioritise the removal of the most dangerous objects (i.e. those who get the highest value based on the selected formula). Nevertheless, each additional removal produced a diminishing effect on the effectiveness (i.e. influenced less and less the population) thanks to the action of the controller, which automatically removed objects from the shells with the highest densities, which were subjects to a higher debris flux, and thus reduced the collision risk where it had a higher value. However, in MISSD, each removal has a direct impact on the collision probability in a shell, while this is usually associated with uncertainty (i.e. some removals will have no effect at all); therefore, reducing the number of objects in any shell will decrease the collision probability, and thus the effectiveness of subsequent removals.

4.3.5. The effectiveness as a function of the PMD compliance and removal rates

The NERF values and total end populations for different levels of PMD compliance and removal rates are shown in Figure 4-10 and Figure 4-11, respectively. In both figures, the x- and y-axis represents the annual removal rate of inactive payload (u_{IP}) and rocket bodies (u_{RB}) respectively. The combinations of removals tested in the simulations are marked with a cross, while red squares in Figure 4-11 marks the best results obtained for different levels of annual removal rates (which lie on 45-degree parallel lines on the plot). The interpolated colour map and isolines visualise the end populations and NERF levels. They visually indicate that multiple strategies can achieve the same end population (or NERF), either varying the compliance level or the removal rates (numerical values are reported in Table 4-8).

For low values of active removals, it was more effective to remove rocket bodies rather than inactive payloads, as highlighted in the variation in the slope of isolines and colour, particularly visible near the origins of Figure 4-10 and Figure 4-11.

This behaviour can be verified by observing the plot of the spatial density (Figure 4-12). At the initial time, the 950-1,000 km shell had the highest number of rocket bodies (167 objects) and was the 4th most crowded shell for payloads (190 objects), while a total of 21 new inactive payloads and 12 rocket bodies were launched in the 900-1,000 km region every eight years. Removing a sufficient number of objects had a similar effect of a lower launch rate, with the difference that the removals were focused on the regions with higher populations (and thus risk).

The initial asymmetry vanished when increasing the number of total removals, and best results were obtained with a more balanced combination of removals, indicating the existence of an optimal ratio as a function of the total number of removals. Indeed, with the removal of only one species of objects, the various shells were cleaned from only the selected species of objects, while the objects of the other one kept generating additional collision fragments. Therefore, in the long term, removing only one species of objects was not as efficient as removing both, as suggested by the blue curve in Figure 4-12 which was obtained with $u_{IP} = 5$ and $u_{RB} = 5$, and a 90% PMD compliance.

Scenarios with higher PMD compliance could produce effectiveness similar to those achieved when actively removing additional debris, depending on the selected values of PMD and removal rate (Figure 4-10). As a general rule, a rise of 30% in PMD compliance resulted in effectiveness similar to the removal of five additional debris per year. Indeed, using a PMD compliance of 0%, a combination a limit of 15 total annual removals ($u = u_{IP} + u_{RB} = 15$) was the minimum needed to achieve a total end population at the same level as the initial epoch (i.e. NERF=0.77), and in no case the performances were better than the benchmark best-case (i.e. NERF=1). Using a 30% and 60% PMD compliance, simulations needed the annual removal limit set to ten ($u = u_{IP} + u_{RB} = 10$)

to achieve a population lower than the initial one. With a PMD compliance greater than 90%, only five were needed ($u = u_{IP} + u_{RB} = 5$), while the NERF exceeded 1 only when setting the annual removal rate to 20 (and only in 4 cases among 10).

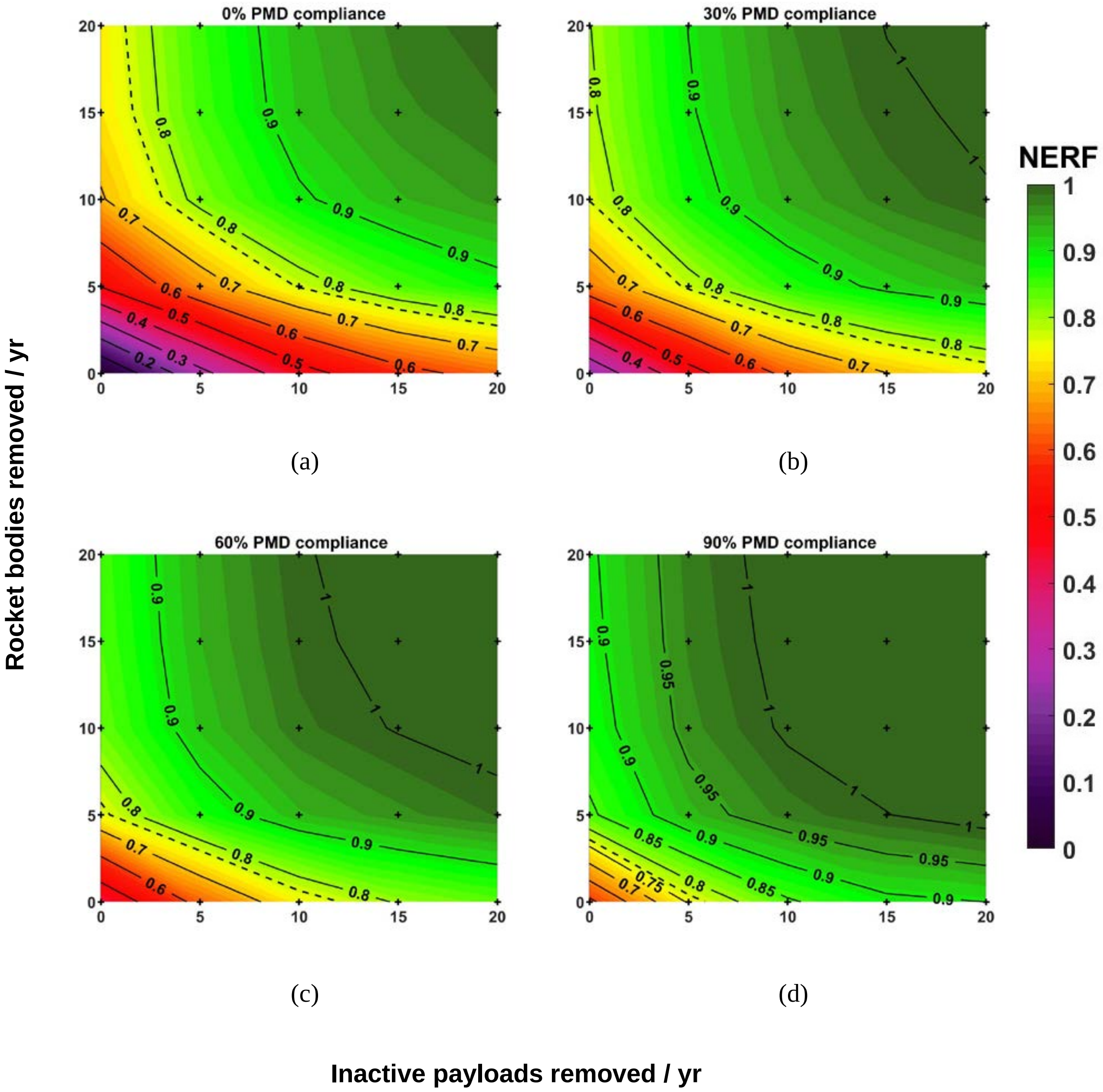

(a)

(b)

(c)

(d)

Figure 4-10. NERF values as a function of the PMD compliance and annual removal rates. The effectiveness increases with PMD compliance and asymmetrically with the total number of removals. The colour map and the contours represent a linear interpolation of the results, which are marked with a cross. The dotted line represents the level of 0.77, corresponding to the initial population.

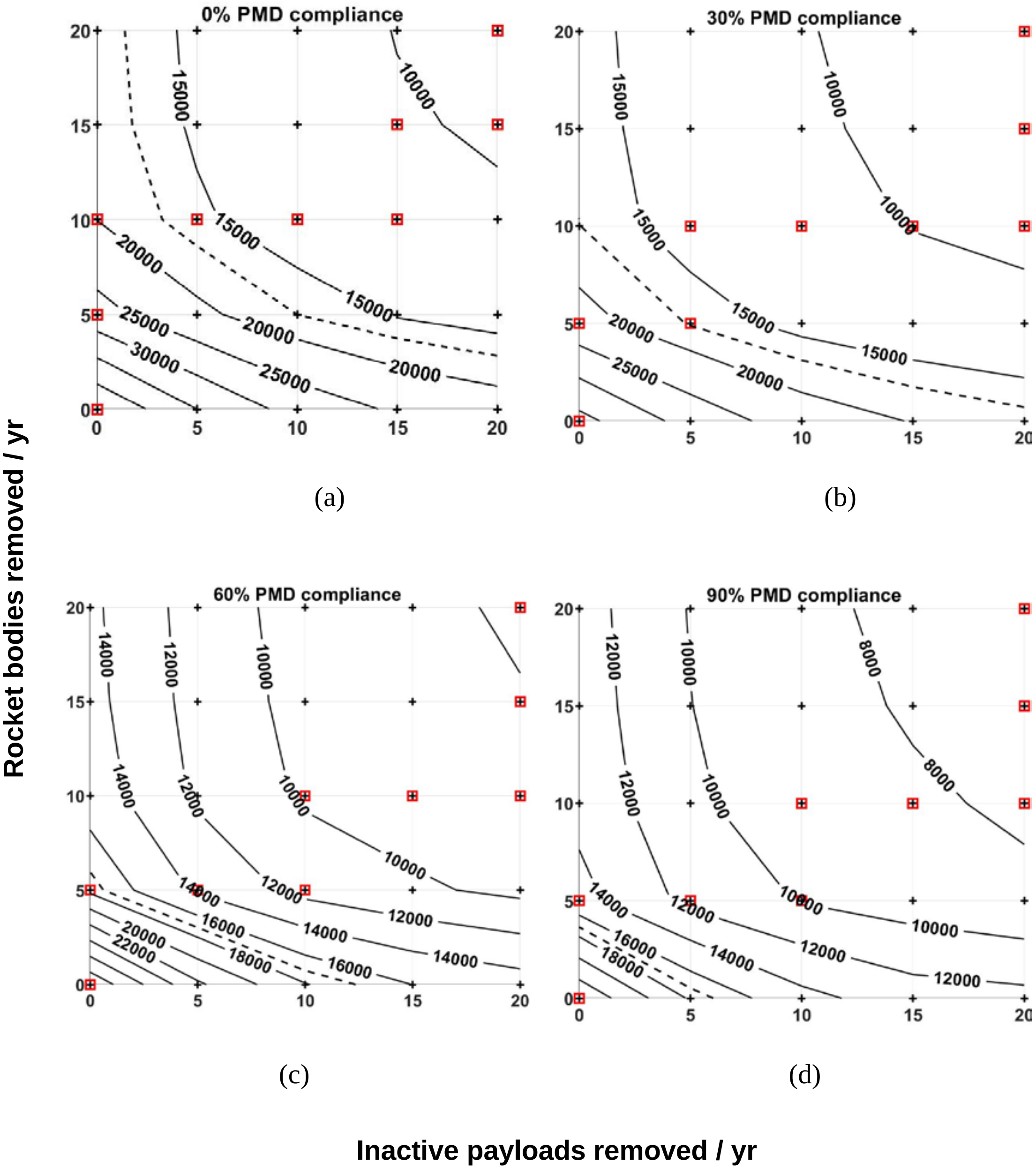

(a)

(b)

(c)

(d)

Figure 4-11. The total end population as a function of the PMD compliance and annual removal rates. The lines represent a linear interpolation of the results, which are marked with a cross, while the dotted line represents the level of the initial population. Red squares indicate the results with the lowest population for a fixed number of total removals per year.

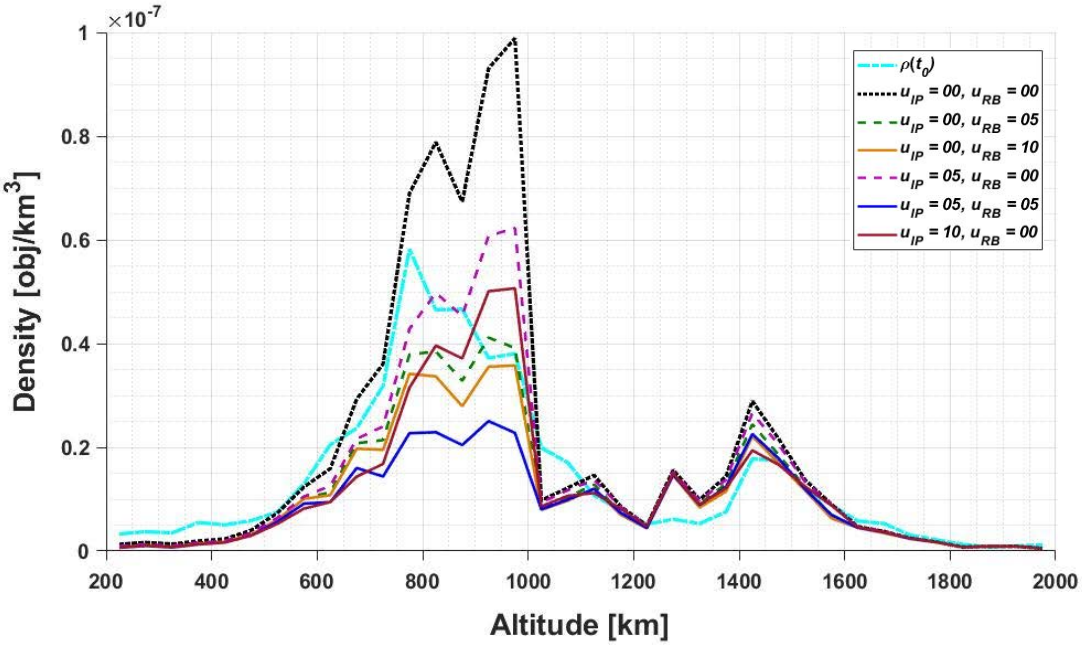

Figure 4-12. The spatial density at end time for six ADR strategies with a 90% PMD compliance.

Table 4-9. The minimum number of the total annual removals ($u = u_{IP} + u_{RB}$) needed to have the final population lower than the initial one (second column) and lower than the best-case scenario without removals (third column).

PMD Level	**Min removals for NERF≥0,77**	**Min removals for NERF≥1**
0%	15	-
30%	10	30
60%	10	25
90%	5	20

4.4. Summary

This chapter illustrated three control laws that were used to investigate the effectiveness of different ADR strategies that target inactive payloads and rocket bodies in LEO when subject to different levels of PMD compliance. Thanks to the controller, it was possible to automatically remove a different number of inactive payload and rocket bodies from each shell based on the selected strategy. Each strategy was then evaluated via a normalised performance index, which measured the effectiveness comparing the end populations against worst- and best-case scenarios.

Chapter 5. Large constellations

The work presented in this chapter explores other uses of the model outside its original scope. These analysis studied multiple scenarios each with a synthetic large constellation and no control, i.e. no active removals were performed (Somma, Lewis and Colombo, 2018b, 2019).

This chapter is divided into two main parts. Section 5.1 used MISSD to investigate the effect of varying the size and the residual lifetime of the satellites (Somma, Lewis and Colombo, 2019). The produced results were found to be deeply affected by the lack of satellite repositioning at the end of their lifetime. Therefore, a new analysis was carried out in Section 5.2 modifying the model and accounting for the spacecraft re-location in lower disposal regions and investigating the combined effects of varying the number of satellites, their PMD compliance and operative life (Somma, Lewis and Colombo, 2018b).

Recently, several companies, including OneWeb, Boeing, SpaceX and Samsung, have shown interest in a region between 1100 and 1300 km altitude, proposing constellations of hundreds (or even thousands) of spacecraft to provide telecommunications services and global internet coverage with a low latency (Lindsay, 2016; Radtke, Kebschull and Stoll, 2017).

These constellations are becoming a reality: in February 2018 SpaceX successfully launched the first two test satellites of their Starlink constellation, which should be composed of about 800 operative spacecraft by 2020/2021 (SpaceX, 2016). In March 2018, SpaceX received the Federal Communication Commission authorisation to launch and operate a total of 4425 satellite at 1125 km altitude (Federal Communication Commission, 2018a), while in November 2018 it received the approval for additional 7,518 satellites at altitudes from 335 to 346 km (Federal Communication Commission, 2018b). OneWeb signed a contract for 21 launches with the Arianespace Soyuz, stating that the commercial service of their constellation (formed by up to 900 satellites) will start in 2019 (OneWeb, 2017). The first six satellites were successfully launched in a parking orbit at 1,000 km altitude on the 28th February 2019 from French Guyana using a Russian Soyuz-2 ST-B rocket (OneWeb, 2019). In addition, there were performed test operations for the release in the following 20 launches of up to the entire satellite batch, composed by up to 36 satellites each, while additional launches ones are scheduled with Virgin Orbit and Blue Origin launchers (OneWeb, 2017).

Considering the increasing interest in large constellations at around 1200 km altitude, analysis of the effects of the presence of a constellation in a spherical shell at 1200-12500 km altitude were carried out. With the aim to increase the understanding of the effects of these constellations and their impact on the environment (i.e. the debris generation and interaction), sensitivity studies are carried out on the constellation size, post-mission disposal (PMD) compliance level, and duration of operational life.

5.1. A sensitivity study on the number of satellites and their post-mission lifetime

This section presents a study, similar to (Bastida Virgili *et al.*, 2016), where additional active payloads are launched in the 1200-1250 shell to simulate the presence of synthetic constellations. The analysis explored the evolution of the LEO population varying the number of satellites in the constellation (i.e. its size, Section 5.1.2) and their post-mission lifetime (Section 5.1.3), as listed in Table 5-1. Lastly, Section 5.1.4 discusses the results and draws conclusions.

Table 5-1. The constellation parameters explored.

Parameter	**Values**
Constellation size (# of satellites)	250, 500, 750, 1000
Satellite residual lifetime	0, 5, 10, 15, 20, 25

5.1.1. Method

All the simulations started in 2009 with the default initial population and launch profile (the MASTER 2009 database from which the data were extracted had the reference epoch of 1 May 2009, see Section 2.11). The constellation is active for 50 years from 2020 to 2070 and becomes fully deployed in 2025, with the same launch rate used to build-up and to replenish the constellation. After five years of operative life, satellites become inactive (also those not belonging to the constellation), and 90% of them are removed from the environment accordingly to their residual set post-mission lifetime.

Table 5-2. The maximum density during and at the end of the simulation as a function of the constellation size.

Const. size	$\rho_{\max}(t)$ **[#/km^3]**	**Time [yr.]**	**Altitude [km]**	$\rho_{\max}(t_{end})$ **[#/km^3]**	**Altitude [km]**
0	$9.55\ 10^{-8}$	2162	950-1000	$9.23\ 10^{-8}$	950-1000
250	$9.72\ 10^{-8}$	2206	950-1000	$9.98\ 10^{-8}$	950-1000
500	$1.95\ 10^{-7}$	2074	1200-1250	$1.03\ 10^{-7}$	950-1000
750	$3.75\ 10^{-7}$	2075	1200-1250	$1.56\ 10^{-7}$	1150-1200
1000	$6.17\ 10^{-6}$	2075	1200-1250	$2.72\ 10^{-7}$	1150-1200

Table 5-3. The total end population and the cumulative collisions as a function of the constellation size. The first row represents a no-constellation case.

Constellation size	**Total end population**	**Total collisions**
0	22,353	65
250	24,568	70
500	30,354	90
750	39,928	139
1000	53,394	233

Each constellation satellite had a mass of 200 kg, a diameter of 1 meter, and a cross-sectional area of 1 m^2. These parameters are in the range of those proposed for the planned new large constellations, which should have a mass of 140-400 kg and an approximate volume of 0.6-1 m^3, and an operative life longer than 5 years (Azzarelli, 2015; OneWeb, 2017; Federal Communication Commission, 2018a). The other objects' physical quantities (area, mass, radius) derived from averaging values in the MASTER database (Oswald *et al.*, 2005; Flegel *et al.*, 2011).

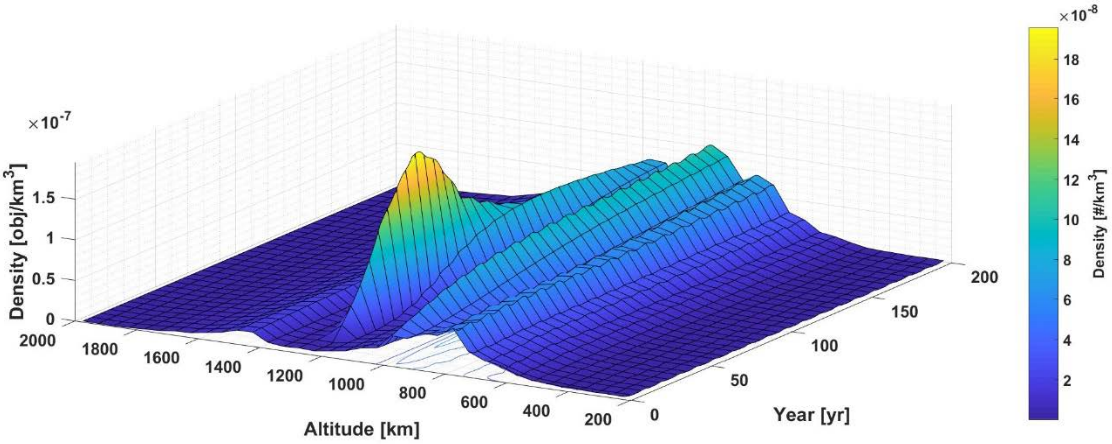

Figure 5-1. The total spatial density as a function of the altitude and time with a constellation formed by 500 satellites each with 5 years of operative life and 25 years of post-mission residual lifetime.

5.1.2. Constellation size

Different constellation sizes were tested, launching up to 8 rockets each with 25 satellites, with these values being compatible with the proposed plans and payload capability of commercial rocket launchers. Therefore, up to 200 satellites were launched per year, forming constellations of 250, 500, 750, and 1000 units in a maximum time of 5 years. Each of them had an operational life of 5 years and 25 years of residual lifetime, while rocket bodies were operational for a single time step (0.1 years).

Results showed, as expected, that the maximum object density, the total end population, and the cumulative collisions increased with the constellation size (Table 5-2, and Table 5-3). With 500 or more satellites, the maximum object density occurred in the constellation shell just after the constellation decommissioning (Figure 5-1 and Figure 5-2). Conversely, with 250 satellites, the density peak happened in the lower, more crowded 950-1,000 km region. In this case, both the collisions and the total population at the end time remained relatively close to the case with no constellation with an increase of +7.62% and +9.94% respectively. The evolution of the density of the 500-satellite constellation had a particular feature: the peak density was in the 1200 km region in 2074, but then the effects of the constellation presence vanished with time (Figure 5-1). Indeed, at the end time, the maximum density occurred (like in a no-constellation case) in the 950-1,000 km shell.

The density of inactive payloads resulted in an order of magnitude higher than that one of active payloads (Figure 5-2) due to the inappropriate modelling of the satellite’s PMD. Discussion on this topic will be presented in Section 5.1.4.

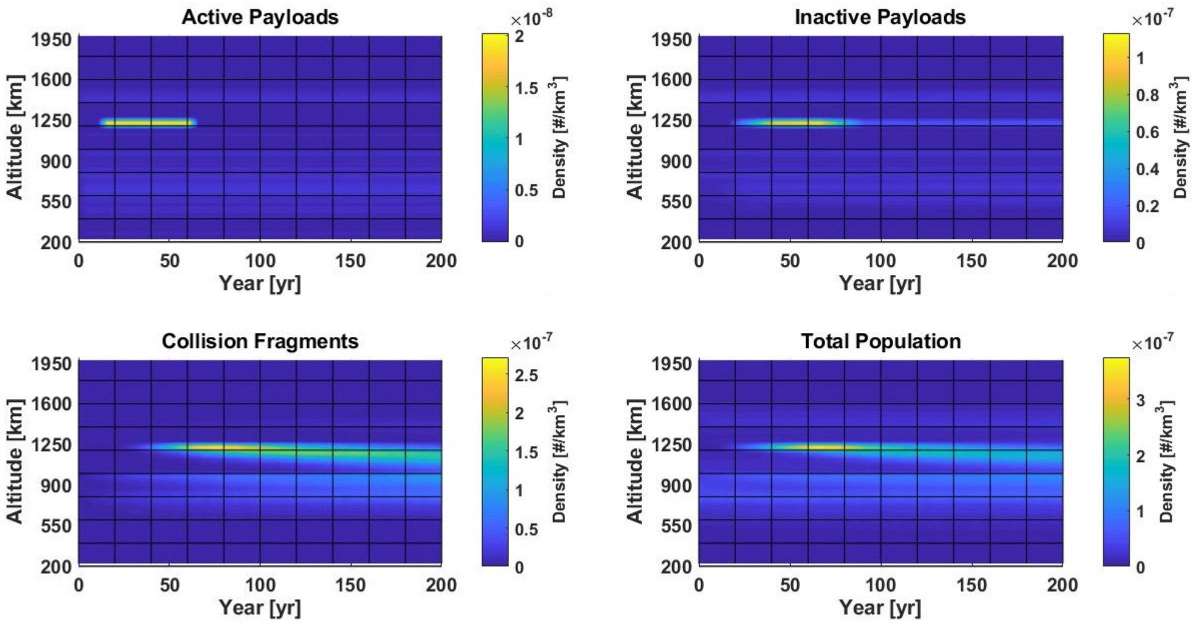

Figure 5-2. The spatial density of active and inactive payloads, collision fragments and total population as a function of altitude and time with a constellation formed by 750 satellites.

5.1.3. Residual lifetime

This study tested the sensitivity of the LEO population to the post-mission residual orbital time. A constellation of 750 satellites was built up and maintained with 150 satellites launched per year (via

6 launches with 25 satellites each) in the 1200-1250 km shell with a residual lifetime of 0, 5, 10, 15, 20, and 25 years after 5 years of operative life.

Results showed, as expected, that the collision rate, total population and maximum orbital density increased with the residual time (Table 5-4 and Table 5-5). The effects were not limited to the constellation altitude but also scattered to lower altitudes due to the effect of drag on the newly generated fragments which possess a higher area over mass ratio compared to intact objects (Figure 5-2), with the maximum density achieved at the constellation shell or just below it (Table 5-5).

Table 5-4. The total end population and the cumulative collisions as a function of the satellite residual post-operational lifetime.

Residual lifetime	**Total end population**	**Total collisions**
0	21,246	50
5	23,666	59
10	26,816	72
15	30,629	89
20	35,025	111
25	39,928	138

Table 5-5. The maximum density achieved during and at the end of the simulation as a function of the satellite residual post-operational lifetime.

Residual lifetime	$\rho_{\max}(t)$ **[#/km^3]**	**Time [yr.]**	**Altitude [km]**	$\rho_{\max}(t_{end})$ **[#/km^3]**	**Altitude [km]**
0	$7.81\ 10^{-8}$	2206.0	950-1000	$7.64\ 10^{-8}$	950-1000
5	$1.09\ 10^{-7}$	2070.1	1200-1250	$8.26\ 10^{-8}$	950-1000
10	$1.64\ 10^{-7}$	2070.1	1200-1250	$8.98\ 10^{-8}$	950-1000
15	$2.27\ 10^{-7}$	2074.0	1200-1250	$9.80\ 10^{-8}$	950-1000
20	$2.99\ 10^{-7}$	2074.6	1200-1250	$1.20\ 10^{-7}$	1150-1200
25	$3.75\ 10^{-7}$	2162.0	1200-1250	$1.56\ 10^{-7}$	1150-1200

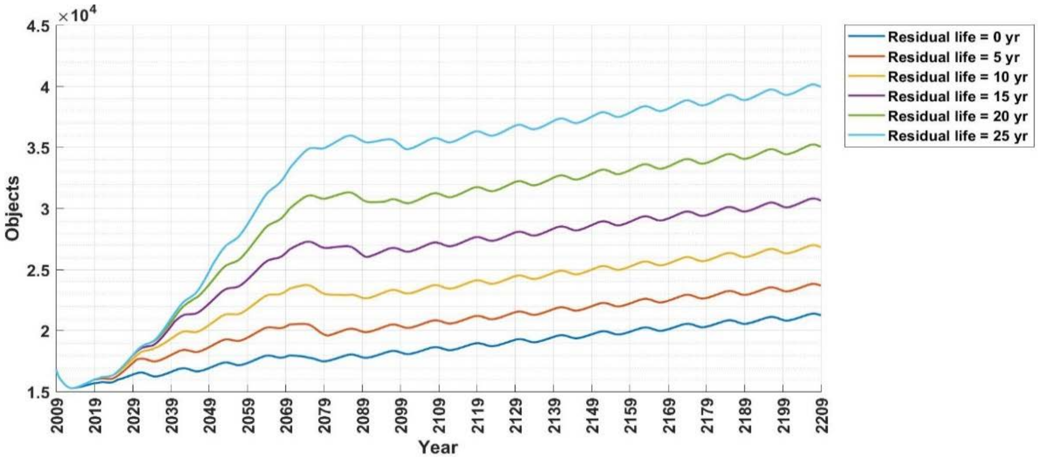

Figure 5-3. The evolution of the total LEO population as a function of the satellite residual lifetime.

Reducing the satellite residual lifetime resulted in fewer inactive payloads in the environment and in a lower number of collisions, leading to a beneficial effect visible from the very early phase of the constellation build-up (Figure 5-3). The presence of the constellation and the orbital lifetime of its satellites produced only a temporary effect, as also highlighted in (Bastida Virgili *et al.*, 2016). However, after the constellation decommissioning, ranging from 2070 to 2095, the total population always increased with similar linear trends (Figure 5-3).

Compared to the case with 25 years, when selecting 5 years of residual lifetime, the total end population and the number of collisions decreased by 40.7% and by 57.2% respectively. This latter case is of particular interest, being similar to one of the planned constellations that aim to perform end-of-life manoeuvres to move the satellites to highly elliptic orbits with less than 5 years of orbital post-operational lifetime (Lindsay, 2016). In this aspect, the model overestimated the number of inactive payloads and collisions, because all orbits were modelled as circular and the inactive payloads were constrained to their original orbits. In reality, the size of the LEO population should assume lower values. The current model applied the same selected residual lifetime to all the rocket bodies, MROs, and inactive payloads (belonging to the constellation or not). Therefore, the model potentially underestimated these "background" populations except when the selected residual life corresponded to the default value of 25 years. In this case, the total population increased from about 24,000 without the constellation to 39,000 (+65.4%), while collisions grew from 74 to 138 (87.5%). However, these results were biased by the inactive population at constellation altitude, due to an incorrect modelling of the satellite's PMD, as discussed in Section 5.1.4. This issue was then corrected modelling the re-orbit of satellites into lower altitude shells at the end of their operative time, as presented in Section 5.2.

5.1.4. Discussion and conclusions

Several sensitivity studies were performed using the MISSD model to investigate the effect of the size and residual lifetime of a large constellation of spacecraft in the 1200-1250 km region.

The used implementation for PMD has the limitation of keeping the satellites at the same altitude of inactive spacecraft, for 25 years after which they are removed, therefore add hundreds of objects into the same shell that can collide. As results, the density of inactive payloads in the constellation shell peaked at about an order of magnitude higher than that one of active payloads (Figure 5-2) in the same shell. The generation of collision fragments and the total population in the constellation's shell correlates with this. Therefore, results were influenced by the assumptions and implementation with respect to the constellation PMD. Acknowledging this limitation, resulted in modifying the model, that in the latest version is able to account for the spacecraft re-location in lower disposal regions. As a result, a new constellations analysis was carried out (Section 5.2).

In the real world, constellation satellites can be transferred (at the end of their operative life) to an elliptic disposal orbit with a much lower perigee. Therefore, inactive payloads and collision fragments should not amass in a thin region but spread to lower altitudes and decay faster. As a result of the lack of modelling of the effect of eccentricity on the orbital decay, MISSD overestimated the number of collision fragments and the total population.

Nevertheless, concerning the analysis on the satellite residual time, removing the bias (i.e. additional fragments produced by the inactive payloads at the constellation altitude) the model reported a similar trend of the population and conclusion of a previous study (Bastida Virgili *et al.*, 2016). Indeed, the satellite post-operational residual time influenced the different rates of increase in the population during the build-up of the constellation; afterwards, a dynamic equilibrium is partially reached during and just after the constellation replenishment; and then similar rate of increase is present in all the cases, with the total population being influenced by the bias in the over-generated collision fragments.

Decreasing the residual lifetime of the satellites reduced the influence of the limitation mentioned above (see the reduction in the number of collisions, Table 5-4), with the results having a null residual lifetime not being affected by this issue.

The launch of a large constellation of 250 or more satellites at 1200-1250 km altitude increased the collision risk in LEO, especially in the 1100-1250 km region. However, reducing the residual lifetime from 25 to 5 years prevented the increase of the inactive population in the early phase of the constellation build-up, and thus limited the creation of new collision fragments. The simulations used an optimistic value for PMD compliance but, on the other hand, the model overestimated the number of fragments generated by the collision with inactive constellation spacecraft. Moreover, the simulated scenarios are similar in number and physical characteristics to some of the recently proposed large constellations. Considering the results, commercial operators should commit to the design of their spacecraft so to have the lowest residual life and to maximise the satellite deorbit reliability. Such measures could lead to mitigating the possible increase of the orbital population and collision risk caused by the presence of large constellations in LEO.

5.2. Re-orbit of spacecraft at end-of-life

5.2.1. Method

A common set of parameters was used to simulate the launch and replenishment of a large constellation at an altitude of 1200-1250 km (see default values in Section 2.11, and Table 5-6). Compared to Section 5.1, a step in increasing the realism was made in the MISSD model, with the implementation of collision avoidance and the repositioning of upper stages, inactive payloads, and MROs into lower circular orbits with a specific residual lifetime. However, the model still lacked orbital perturbations and was not capable of computing the drag for eccentric orbits, producing errors on the distribution of the decaying object which were, therefore, subject only to a lowering in their semi-major axis instead of the lowering of their apogee first. Therefore, the rationale for repositioning the satellites into lower orbits (that could, for example, be achieved in reality with a Hohmann transfer) is to maintain a valid physical model, where objects in circular orbits obey the real laws of physics and decay to lower shells (rather than assigning fraction of objects with different decay times).

Table 5-6. Summary of model parameters used.

Parameter	Value(s)
Initial population	No
Launch traffic model	Constellation only
Solar cycle	No
Collision avoidance	Active satellite (99% success)

Table 5-7. The constellation parameters explored.

Parameter	Values
Size (# of satellites)	500, 1000, 1500, 2000
PMD compliance	0%, 30%, 60%, 90%, 100%
Satellite operative life	4, 8, 16 years

To study the intrinsic dynamics linked to the presence of the constellation, the initial LEO population was neglected. The simulations were run for 200 years, and only objects associated with the constellation were launched. The effect of the solar cycle was also neglected. These assumptions resulted in the exclusion of the constellation interactions with the initial population but, as a side effect, they provided outputs simpler to understand and were used as a testbench for the newly introduced features (i.e. collision avoidance and inactive spacecraft satellite re-positioning).

Sensitivity studies were carried out varying the PMD compliance, size of the constellation, and satellite operative life (see Table 5-7), with the number of annual launches changing accordingly. All active satellites performed collision avoidance manoeuvres with rocket bodies or inactive satellites, with a 99% success rate. This percentage was chosen to leave a small, but not null, chance to have a collision due to errors in the conjunction assessment, to the residual risk that could be present after a manoeuvre, or to the choice by the operator to not perform a manoeuvre. For example, the Iridium-Cosmos collision could have been prevented, the Iridium still being controllable, and the predicted close approach was 584 m (Celestrak, 2012).

With each launch, one rocket body, two MROs (e.g. payload adapters) and 25 satellites were used to build-up, deploy and to replenish the constellation, which was fully deployed in 8 years, with 50 years of continuous launches. These values are compatible with the recent proposals of private companies and the payload capability of commercial launchers. The physical quantities (e.g. mass, cross-section area) of the constellation satellites and rocket bodies were the same as the previous study (Section 5.1.1).

After releasing the satellites, 90% of the rocket bodies were manoeuvred to circular orbits at 675 km, where they had a residual lifetime shorter than 25 years. This should not be taken as a perfect representation of the current deorbiting manoeuvres (which uses high elliptic orbits to lower the perigee), but as the first step to increase the realism of the model. All the MRO were also released in the same altitude shell. After their operative life, the satellites became inactive, and a percentage of them (according to the set PMD compliance level) were re-orbited in a lower circular orbit at 625 km from where they decay in about 25 years due to atmospheric drag.

5.2.2. Results

As expected, the end population was a non-linear function of the constellation size and the PMD compliance level (Figure 5-4). Doubling the satellite operational lifetime resulted in the number of total spacecraft launched being halved. Therefore, fewer inactive satellites were left in the environment; as a result, the total end population was reduced between 75% and 77% (depending on the constellation size and PMD compliance level), while collisions decreased as well between 75% and 88%.

In the worst-case scenario (i.e. a constellation containing 2,000 satellites and 0% PMD compliance), 4.9 collisions per year occurred in the constellation shell while it was active and up to 10.6 by the end of the simulation. Furthermore, additional collisions occurred below the constellation altitude between the decayed fragments and the few decayed derelict objects (i.e. inactive payloads, MROs and spent rockets' upper stages) not complaint with PMD, and also in the lower disposal regions. However, the fragments produced at these lower altitudes were deeply affected by the cleansing effect of atmospheric drag.

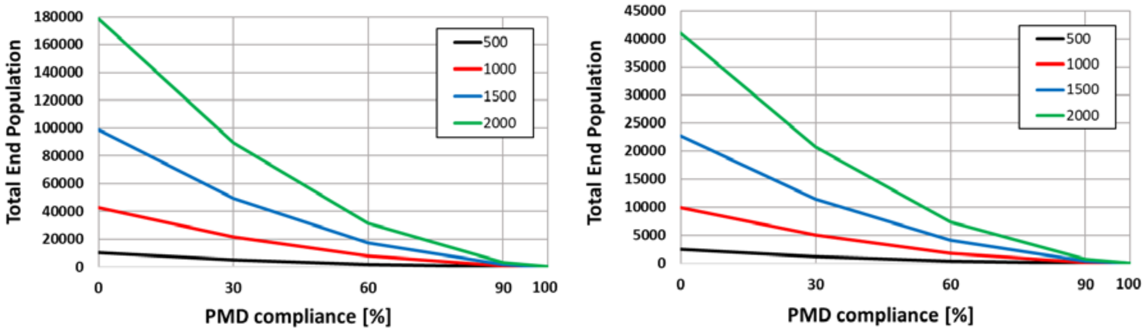

Figure 5-4. Total population at end time as a function of the PMD compliance level and size of the constellation with a satellite operational lifetime of 8 years (left) and 16 years (right).

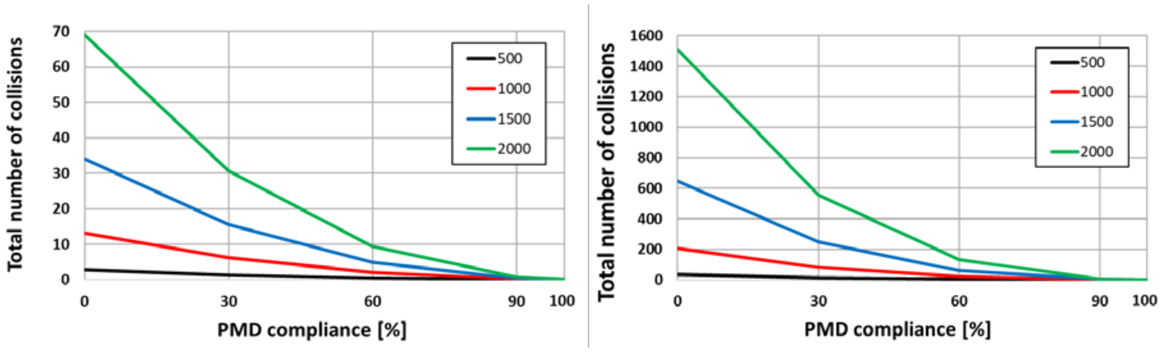

Figure 5-5. The total number of collisions at the constellation altitude at the decommissioning time (left) and at the end time (right) with a satellite operational lifetime of 8 years.

The case with the constellation formed by 1000 satellite was selected to illustrate some of the results. As the satellites were small and lightweight, the number of collisions and generated fragments remained limited. Collisions of active payloads with derelict objects generated hundreds of fragments but were limited in number due to collision avoidance manoeuvres. Collisions between intact objects and fragments were more frequent and maintained almost a constant rate after the constellation decommissioning, but they produced only dozens of fragments per event. These fragments then decayed faster than intact objects due to their higher area to mass ratio, scattering in the lower shells, due to atmospheric drag, with a rate higher than their generation rate (Figure 5-6).

For a PMD compliance equal to or less than 60%, collision fragments became predominant between 60 and 110 years after the beginning of the simulation, while for higher compliance levels, the inactive payloads were the majority of the population during the almost all the timeframe (Figure 5-7). For low PMD compliance levels, the collision fragments in the total population increased steadily (top image in Figure 5-7). However, this behaviour was due to the summation of the fragments at all altitudes, while the number of fragments at the constellation altitude reached its maximum before the end time even with a 0% and 30% compliance (Figure 5-8). Running additional simulations with an end time of 500 years, the same trend appeared at lower altitudes (also visible in the top image of Figure 5-6), with different times needed before reaching the maximum. For all the constellation sizes, the region around the constellation altitude appeared to be able to maintain a dynamic equilibrium where random collision alone are not capable of increasing the total population, i.e. the rate at which collision fragments are generated is comparable with the rate they decay out of the shell (Kessler and Anz-Meador, 2001)

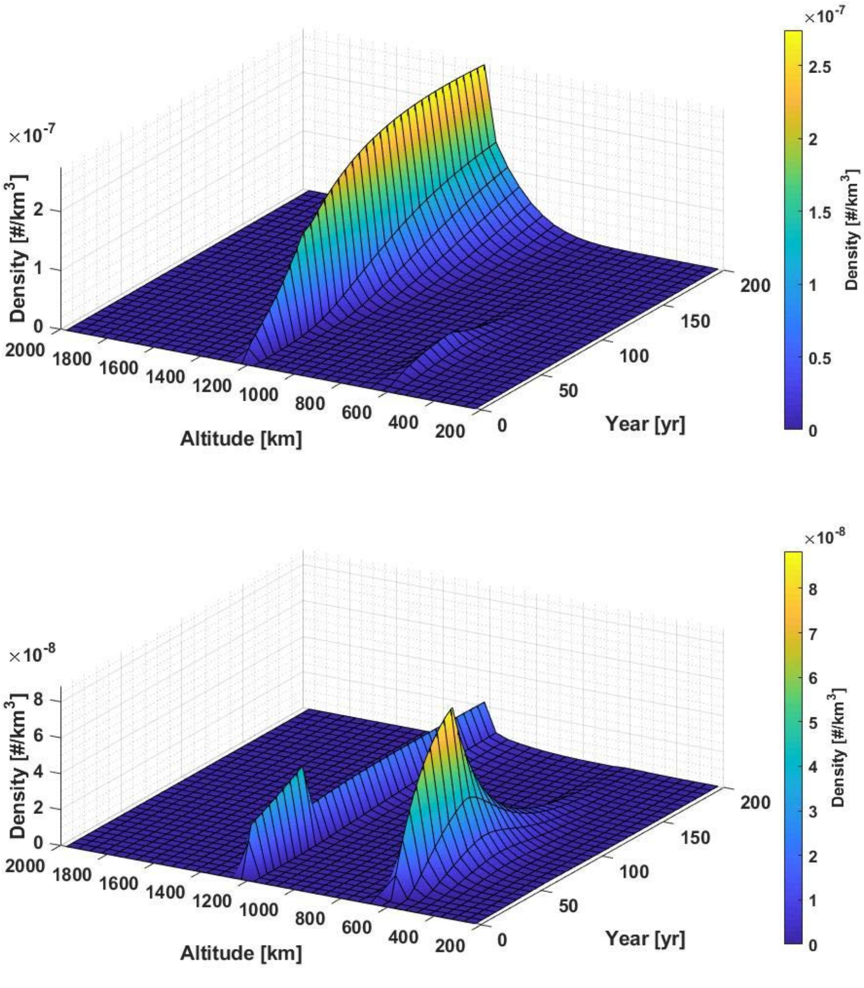

Figure 5-6. The evolution of total density as a function of the altitude for a 1000-satellite constellation for a PMD compliance of 30% (top) and 90% (bottom). Note that the two plots have a different scale on the density axis.

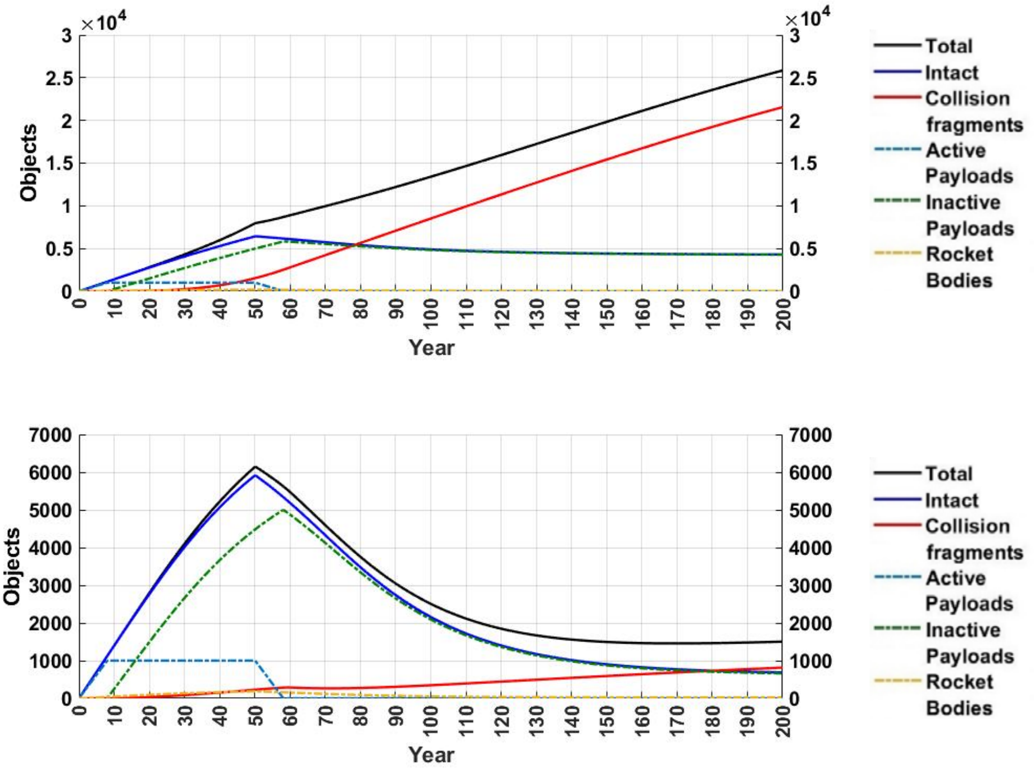

Figure 5-7. The evolution of the orbital population in LEO for a 1000-satellite constellation for a PMD compliance of 30% (top) and 90% (bottom).

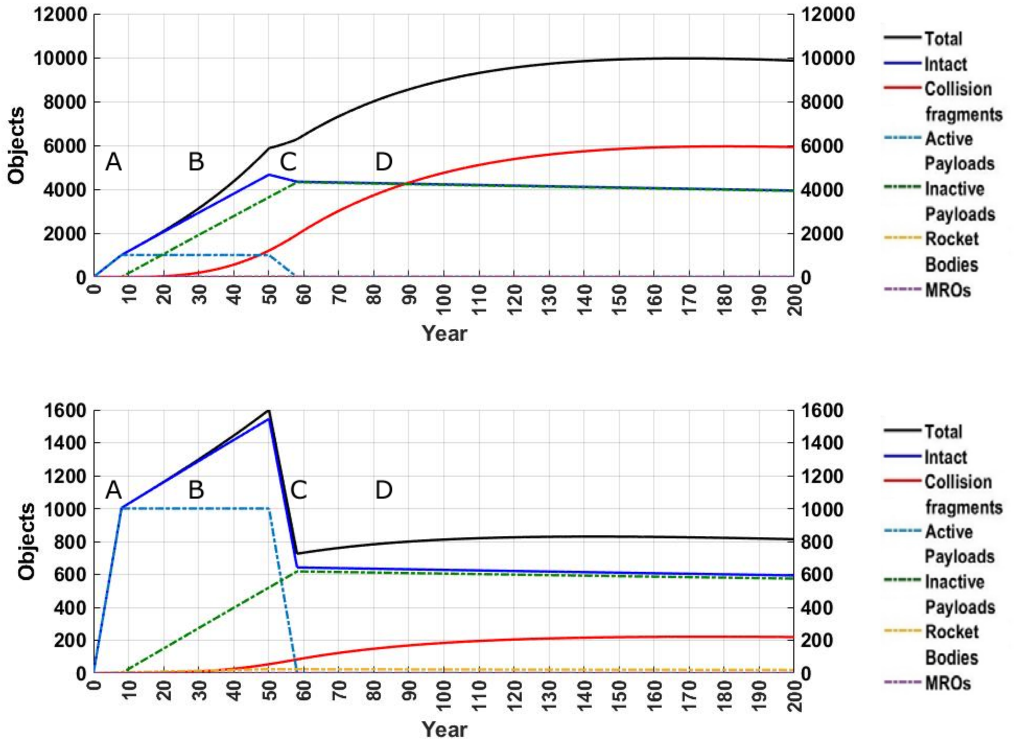

Figure 5-8. The evolution of the orbital population at the constellation altitude, for 1000 satellite and a PMD compliance of 30% (top) and 90% (bottom). Four different phases can be identified: build-up (A), replenishment (B), end of constellation operations (C), post-constellation (D)

Table 5-8. The number of inactive payloads and collision fragments at the constellation altitude at the end time, the total population, and total collisions as a function of PMD compliance, with a constellation formed by 1000 satellite each with 8 years of operative lifetime.

PMD compliance	**Inactive payloads**	**Collision fragments**	**Total population**	**Total collisions**
0%	5,514	11,743	48,827	207.32
30%	3,924	5,921	2,5862	84.4
60%	2273	2,102	10,193	22.96
90%	574	219	1,505	1.47
100%	0	7	100	0.02

The effects of the constellation build-up are visible in Figure 5-6: the intact population increased at constellation altitude and in the disposal orbit, where payloads were manoeuvred at the end of their operative life. After the constellation decommissioning, the intact population at constellation altitude remained steady at a value approximately equal to the 10% of the total number of objects launched (the PMD compliance was 90%), with some objects scattered in the 100 km below, and few involved in collisions, which contribute to the remaining quota of the population at the constellation altitude (574 inactive satellites and 220 fragments).

The effects of the presence of the constellation vanished with time at all but constellation altitudes regardless of the PMD compliance, where the non-compliant spacecraft remained (Figure 5-6 and Figure 5-8).

5.2.3. Discussion

The choice to simulate only the building and evolution of the constellation, neglecting the current initial population and other future launches, was made to eliminate any interference and generate the intrinsic dynamics of a large constellation positioned at high altitude. It might be argued that in this way it was removed the possibility for a more complete understanding of the impact of the constellation while interacting with the background population (e.g. there were almost no collisions with compliance higher than 90%). However, even if the initial population would have increased the number of collisions and therefore influenced the distribution of the objects (in particular in the post-constellation phase), the basic dynamics of the population remains the same and agree with a previous study (Bastida Virgili *et al.,* 2016). Indeed, the same four different phases can be identified, as illustrated in Figure 5-8: build-up (A), replenishment (B), end of constellation operations (C), post-constellation (D). However, the removed the background population helped to identify the constellation dynamics with clear trends and contributes from the specific species that could have been masked by other interactions with the background population or not identified looking only at the total population.

In the short term, the constellation produced an increase in the spatial density both at the constellation altitude and in the lower region where the decommissioned satellite would pass, increasing the risk of collision with other spacecraft or fragments. In reality, these inactive spacecraft would be likely catalogued and easy to track, resulting in an increase in the number of collision hazard and avoidance manoeuvres.

In general, these simplifications would produce different results with the current LEO population and launch traffic. However, between 1200 to 1250 km, low traffic and density of objects exist, with only about 17 intact and 168 fragments in 2009 (Oswald *et al.*, 2005; Flegel *et al.*, 2011). In previous simulations with no constellation, the relative lower traffic and population in higher altitudes would mitigate, but not cancel completely, the consequences of not implementing the spacecraft relocation at the end of their operational life.

Due to the lack of modelling of the drag on elliptic orbits, it was assumed that end-of-life transfers happened directly to circular lower disposal orbits. This lack of elliptic disposal orbits (with apogee near the initial altitude and perigee at the disposal altitude) affected the distribution and evolution of inactive spacecraft, which were instantly repositioned to a lower disposal circular orbit. As results, the inactive spacecraft were absent from 1200 to 625 km (see Figure 5-6) instead of transiting into these intermediate altitudes due to the orbital eccentricity.

Another source of error is the assumption that all inactive payloads, MROs, and fragments within a shell can collide with any other object in the same volume (i.e. their position probability is uniformly distributed within the volume). Constellations have a spatial structure, and therefore they are not represented correctly in the model, with also the inactive satellites that would maintain some spatial structure after their decommissioning. Additional analysis might be able to quantify and correct these errors using results from other models to perform a calibration of the collision rates and then applying corrective factors in MISSD (see Eq. (2.20) in Section 2.3). Another solution would be to continue developing the model, modelling the structure of the constellation and the decay of non-circular orbits (e.g. adding inclinations and eccentricity bins).

5.2.4. Conclusions

Large constellations will greatly increase the total number of intact objects in LEO. Such constellations have the potential to endanger the local stability of the space environment since the beneficial effect of drag is negligible at the proposed altitude.

A high level of PMD compliance was able to prevent a steep increase in collisions and fragments in the long term. In addition, increasing the satellite operational lifetime vastly decreased the total number of inactive spacecraft produced by the constellation replenishment. The presence of the constellations also presented short-term effects, with an increase in the local collision risk and thus the number of collision avoidance manoeuvres needed to operate the spacecraft safely.

Space operators should not only watch for the effects of the constellation on the short term (i.e. the increasing collisions risk and thus the number of collision avoidance manoeuvres), but also for the long-term ones, in the interest of the space environment preservation.

Chapter 6. Summary and general discussion

This chapter begins with a summary of the key results (Section 6.1) and continues with a critical assessment of the method assumptions and their implications for the results (Section 6.2). The method robustness is then presented (Section 6.4) before the main discussion on the results (Section 6.4). Lastly, the impact of the research is stated (Section 6.4).

After an introduction of the space debris problem and a literature review (Chapter 1), it was presented a model of the LEO environment capable of computing the evolution of the orbital population in the low Earth orbit (Chapter 2). The model, called MISSD, included six object species, an altitude shell discretisation, launches, collisions, explosions, atmospheric drag, post-mission disposal (and its level of compliance), and a novel feedback controller on active debris removal that is capable of handling multiple user-selected control laws.

While other models try to produce accurate orbit predictions with orbital propagators, MISSD used a simplified approach, with objects grouped into six species with similar physical and behavioural characteristics. As results, it was possible to evaluate and identify rules which might have otherwise been missed.

Using the NERF as a common performance index (Section 2.9), it was possible to investigate and compare the effectiveness of different combinations of PMD compliance and ADR strategies in LEO. After performing tuning and sensitivity analysis (Chapter 3), the potential impact of ADR missions that target inactive payloads and rocket bodies was then analysed and compared at various levels of PMD compliance (Chapter 4). Additional studies with synthetic large constellations were also performed to explores other uses of the model outside its original scope (Chapter 5).

6.1. Key results

The work performed in this thesis allowed to answer the research questions posed in Section 1.5.

- Are there any general rules for increasing the effectiveness of ADR strategies?

Results obtained from simulations that used two different control laws agreed that same end population, and thus strategy effectiveness (NERF), could be achieved with multiple strategies varying the PMD compliance and the maximum annual removal rates. However, **the effectiveness of ADR-strategies could be increased selecting optimal combinations of removals of inactive payloads and rocket bodies in LEO,** which were a function of the PMD compliance and the set maximum annual removal rate.

Different control laws produced different results, with higher benefits obtained with the quadratic control law.

- What species of objects should be actively removed?

With less than 15 maximum annual removals, the strategies that maximise the effectiveness had twice the maximum annual removal rate for rockets bodies compared to inactive payloads. Increasing the maximum annual removals and PMD compliance, **the optimal strategy shifted to a more balanced combination**, with the exact number depending mainly on the PMD compliance level.

6.2. Method critical assessment

Earth harmonics, luni-solar and other orbital perturbations were not modelled because of the lack of any geographical and spatial reference of the Earth's surface and gravity (the gravitational potential is assumed to have a spherical symmetry). This implies that the orbital elements of each object are not subject to variation, except for the atmospheric drag, which was modelled because of its major influence on the semi-major axis. The third-body perturbation of Moon, Sun and other planets act on the right ascension of the ascending node and argument of perigee, and has a low influence in LEO, while their effect increases in magnitude for higher regions of space. The Earth oblateness acts on the same orbital parameters and is a function of the orbit altitude, eccentricity, and inclination. Given that orbits are assigned to a spherical shell, having a nodal regression does not influence the system dynamics and the collisions rate, which are computed only from the number of objects. The model does not account for solar radiation pressure, which would have minor effects only on the upper part of LEO.

Another caveat of this model is linked to the modelling of the orbital decay. The current model does not consider the orbital eccentricity, with objects were restrained to have only circular orbits (and therefore have a circular decay formulation) Therefore, when computing the objects' average characteristics and decay parameters, each object is assumed to have a circular orbit and lie in a single shell. Using 36 shells, it is equivalent to having an eccentricity lower than 0.0076 (0.006) in the upper (lower) shell. With the initial population selected in this study (see section 2.1), more than 85% of the payloads and 65% of rocket bodies have an eccentricity that satisfies this assumption. However, the percentages are much lower for collision and explosion fragments. Some of them possess a high eccentricity gained during their generation. This might lead to differences in the compositions of the population, especially in the higher shells, with an over-estimation of the number of fragments due to their artificial placement in circular orbits with a longer lifetime. A possible improvement of the model might include the addition of eccentricity bins, as previously done in other PIB models (Rossi *et al.*, 1998; Kebschull *et al.*, 2016). However, only a relative minority of the LEO population is present above 1,000 km. As previously discussed (Sections 2.7, and 2.10), this simplified PMD formulation - and the assumed compliance level - used with a standard initial population and launch traffic, influenced in a minor way the magnitude of the results, but did not influenced the overall system dynamics and the draw conclusions (see also the scale of the inactive payloads and density components in Figure 3-10 in Section 3.3). In addition, to reduce these errors in future studies, the model was improved with the implementation of the option for the satellites and rocket bodies to be relocated, at the end of their operational life, as presented in Chapter 5.

Another source of error is the assumption that all objects can collide with each other in each shell (i.e. their position probability is uniformly distributed within the volume), as in all PIB models, thus overestimated collisions. However, in the model formulation, it was provided with a way to tune the number of collisions based on results from other models (see Eq. (2.20) in Section 2.3).

Due to the statistical approach, objects lose their individuality once they were injected into the model (i.e. single objects were not tracked and propagated in the model). As a result, the model, which was not built for this purpose, did not allow to track fragments and create a list of specific hazardous objects.

Due to the deterministic approach, stochastic events were not modelled. These includes (but are not limited to) satellite becoming inactive due to anomalies, a decrease in the launch activities due to technical problems or an increase due to a technological advance, ASAT tests, variation in the atmospheric density due to solar-related stochastic events (e.g. a higher or lower solar cycle, solar flares), and the physical characteristics of fragments generated in breakup events.

Concerning those latter, it was also assumed that the objects could be represented by the average physical characteristics for the same group in each shell and that these characteristics would not change in the future. This simplification introduced errors, especially when compared with the current population. However, we have no way to estimate their future values, as well as for the future level of adoption of PMD measures, future launch rate and profile for which sensitivities studies were carried out (Section 3.4).

It was assumed that the removal missions were possible, had a 100% reliability, and started in 2020, with the objects being removed at the end of each time step. Even if there is no certainty on when the first complete ADR mission will be carried out, there has been in recent years an increase in interest, funding and research on critical components of the technology required for ADR missions, with the first technology demonstrator already launched and with recent tests (September 2018 - February 2019) successfully concluded in with a net capture, a harpoon, and a visual navigation experiments (Taylor *et al.*, 2018; Surrey Satellite Technology Limited, 2019).

Based on the observed values, the controller selects the removal rates to be applied at the end of each time step. This is a suboptimal choice that might lead to some oscillations in the removal rate (and thus the size of the orbital population) for very small timestep. In addition, some time would be required for preparing, launching, and achieving the removal of the objects that might have partially deorbited, collided or no longer in the removal list given the updated populations. An improvement on this issue might be to include a time delay in the ADR and to use as a base for the removal rates on the future prediction of the environment rather than on the actual conditions.

Another caveat is that the effect of the objects' removal is immediate and certain because of the way that collisions are calculated, with the collision rate being explicitly based on the square of the number of objects in each shell; so, reducing the number of objects will have an immediate and quantifiable effect. Conversely, in reality, the removal of an object might have an effect on a future time when a collision that involved the removed object would have been taking place. As a result of this uncertainty, (on average) many removals are needed to prevent a single collision.

The model was able to capture the overall dynamics of the long-term evolution of the LEO population, with results comparable to the arithmetic average results of Monte Carlo analysis. However, studies with Monte Carlo techniques can produce probability functions on the outcome when varying some input parameters, such as the launch rate, solar cycle, explosion rate. Results from White and Lewis showed that this variability on the outcome can reach up to a factor of ten in the population range and that the distribution of their results followed a log-normal distribution in which the mode of the end population was about 15-25% lower than the arithmetic average (White and Lewis, 2014b). Therefore, using the arithmetic average resulted in a more conservative approach. A similar study reported that the breakup model, the collision prediction algorithm and future solar activity would affect the future population but would leave unchanged the long-term dynamics, while the level of compliance with PMD would change the long-term dynamics, with variation from exponential to linear trend in the future LEO population (Revelin, Di Costanzo and Dolado-Perez, 2015). As results, studies in this work have been performed at different levels of PMD compliance so to verify that the conclusions would not be affected. In addition, a sensitivity study on a base case was performed varying the compliance levels from 0% to 100% (Section 3.4.1).

6.3. Model robustness

The MISSD model was compared against the IADC 2013 study (Inter-Agency Space Debris Coordination Committee *et al.*, 2013; Liou *et al.*, 2013) and it was able to produce quantitative results consistent with other similar works in the literature (Section 3.1). The influence of the solar cycle and the NASA break up formulation were also verified (Sections 3.2.1 and 3.2.2).

The stability of the Euler integrator was assured selecting a step size of 0.1 years as results of the investigation performed in Section 3.1, while the selection of the default number of altitude bands was conducted in Section 3.1.2. Sensitivity studies on the PMD compliance level and launch rate were also performed to test the model robustness to the variance of these inputs (Section 3.2.2).

Simulations were performed implementing the solar activity with an average mean value or with an 11-yr cycle, or with a different initial population, with more than 7,000 simulations run in total. Nevertheless, the conclusions drawn from the analysis were not affected because the influence of these parameters was limited only to the numerical outputs and not to the overall dynamics.

6.4. **Results discussion**

The analysis presented here confirmed that the future LEO population might increase even with a 90% compliance with post-mission disposal guidelines, no launches, and no ADR (Kessler *et al.*, 2010; Bennett and Sang, 2011). Active debris removals presented a possible solution to maintain or reduce the orbital population and the collision risk in specific regions within a target value.

The results highlighted that a combination of both PMD and ADR measures could maintain a dynamic equilibrium in the total LEO population in a 200-yr timeframe, while in general, even a very high level of PMD alone (e.g. 90%) was not sufficient in the performed simulations.

Strategies that removed only inactive payloads achieved lower NERF scores compared to those that removed, even partially, bigger, and heavier rocket bodies. This remained valid for all PMD compliance levels and was found using both the linear and the quadratic control law.

Varying the PMD compliance and the annual removal rates, it was possible to achieve the same effectiveness with multiple strategies. However, fixing the PMD compliance and using ADR, it existed optimal combinations of removals of inactive payloads and rocket bodies . In particular, in multiple instances, for a set amount of annual removals, the highest efficiency resulted from acting on rocket bodies only, while the highest efficiency was never obtained removing inactive payloads only. In general, the effectiveness values obtained for a selected removal rate of inactive payloads, when setting less than 15 maximum annual removals, were similar to those obtained with half that rate of rocket bodies, suggesting that removing a single rocket body could be as effective as removing two inactive payloads (which had a smaller cross-section area and weight). This held true when using either the linear or the quadratic control law, and regardless of the level of PMD compliance.

Increasing the total annual removal rate and PMD compliance, the optimal strategy shifted to a more balanced combination of inactive payloads and rocket bodies, but always with a minimum level of rocket bodies actively removed. Although previous researches do exist on ADR missions directed toward the removal of this type of object (Praly *et al.*, 2012; Bonnal, Ruault and Desjean, 2013a; Pardini and Anselmo, 2016), the findings indicate the importance of further investigations. While in reality different launchers exist, the model assumed that all rocket bodies had the same physical characteristics, because they maintain general common characteristics, such a higher mass and larger cross-section area than a payload. Therefore, the results hold true with the difference that the removals might need to be performed on a more specific family of these upper stages (Rossi, Valsecchi and Alessi, 2015; Pardini and Anselmo, 2016), such as the many Russian rocket upper stages that lie in the Sun-Synchronous region (Yamamoto, Okamoto and Kawamoto, 2017).

As a general rule, a rise of 30% in PMD compliance produced similar effectiveness to the removal of five additional debris, confirming then the primary role of broad adoption of post-mission disposal. Indeed, when using no PMD compliance at all, more than 15 annual removals were needed to be set as the maximum annual rate in the controller to achieve a population at end time lower than the initial one; ten were needed with a 30% and 60% PMD compliance and 5 or less with a compliance greater than 90%. However, it must be remembered that due to the variability and uncertainty in the parameters and future events it is statistically possible to achieve the same population in a scenario without any removal, or even a lower one (White and Lewis, 2014b).

In the trade-off between the proposed strategies, it should also be considered that the success of a strategy in the real world will depend on the widespread adoption of mitigation measures (not only PMD) by the whole space community, with the current predicted global level of compliance still far from the commonly adopted target of 90% (Morand *et al.*, 2014; Bonnal and Mcknight, 2017). The technology for actively removing objects has matured over the last years, as recently demonstrated in orbit by the RemoveDebris mission (Taylor *et al.*, 2018; Surrey Satellite Technology Limited, 2019). However, the active removal of a non-cooperative target has not been successfully completed yet. Moreover, the reliability and risk of these missions should also be taken into consideration when operating in proximity to uncooperative objects. In addition, the removal of a spacecraft by a third party operator might also create legal issue due to the lacking of international rules (excluding the conventions of a spacecraft responsibility being on the spacecraft owner or the launching state) (Weeden, 2011; Emanuelli *et al.*, 2014).

Considering the increasing interest in large constellations at around 1200 km altitude, analysis of the effects of the presence of a synthetic constellation in a spherical shell at 1200-1250 km altitude were carried out and included the abilities for spacecraft to perform re-location into lower orbits at the end of their operative life (Chapter 5). Large constellations affected the environment in the short term (e.g. increasing collisions risk and thus the number of collision avoidance manoeuvres), but leave the long-term dynamics unaffected, as already demonstrated in the past (Bastida Virgili *et al.*, 2016). Results confirmed that the collision rate, total population, and maximum orbital density increased with the residual orbital time of constellation spacecraft and that the end population was a non-linear function of the constellation size and the PMD compliance level.

The possible growth in the orbital population and collision risk caused by the presence of such large constellations in LEO could be mitigated by the increase in the PMD compliance, satellite operational lifetime, and reduction in the residual lifetime. Considering these and results from other studies (Bastida Virgili *et al.*, 2016; Lucken and Giolito, 2018), commercial operators should commit to the design of their spacecraft so to have the lowest residual life and to maximise the satellite deorbit reliability. Such measures could lead to mitigating the possible increase of the orbital population and collision risk caused by the presence of large constellations in LEO.

These large constellations are becoming a reality, with the first six satellites of one of the planned large constellations were successfully launched at the end of February 2019 (OneWeb, 2019). However, a sense of responsibility toward the shared use of the space might be emerging, with the operator of the above-mentioned constellation aiming to have a disposal orbit of fewer than 5 years with a reliability greater than 90% (Lindsay, 2016, 2017).

6.5. Impact of the research

The work performed in this thesis defined a method to compute the evolution of the LEO population and compare the effectiveness of different mitigation and remediation strategies. A wide variety of scenarios were tested, allowing the possibility to identify principles to increase the effectiveness of ADR strategies. These principles could be exploited in further research in the field or applied to a real case scenario. For example, rocket bodies are known to contribute to the space debris problem. However, thanks to this research, it was possible to explicitly quantify the benefits of their removal compared to inactive payloads.

This thesis also showed that a feedback controller that acts differently as a function of the object species and orbital distribution (following one among the available control law) could be effectively used to simulate the process of adopting ADR strategies and adapting them to temporal and spatial variations. Indeed, this novel controller allowed an investigation for the first time of the relationships among control measures and different object species, measuring and comparing their effectiveness in a broad set of scenarios when subject to a different combination of mitigation and remediation practice implemented (i.e. PMD and ADR).

From a practical point of view, the results produced could contribute to the discussion on the effectiveness and improvements of remediation guidelines for the LEO environment. Thanks to its modular approach, its relative simplicity and its fast execution time, the used model could also further be exploited as an educational tool to swiftly test hypothesis and produce results. Lastly, the MISSD model inspired the creation of another space debris model (Lucken and Giolito, 2018).

6.6. Future Outlook

MISSD evolved through time, with incremental changes and additional modules and options developed so to have always a working model able to produce outputs while gaining in complexity. At every main improvement, validation analyses were performed to test the newly introduced capabilities and general model behaviour. However, the model might still be improved for future works in several ways.

For example, additional discretisation on the orbital parameters (semi-major axis, eccentricity and orbit inclination) and physical characteristics (area and mass, Figure 6-1) could make possible to improve the controller selection of the objects subject to ADR and their correlations with the existing current population. In addition, this would also make possible additional studies, such as investigate the influence of CubeSat and specific (mega-) constellation on the space environment (Figure 6-1). With a minor variation of the existing code, additional objects types could also be included in order to differentiate the action of the controller further.

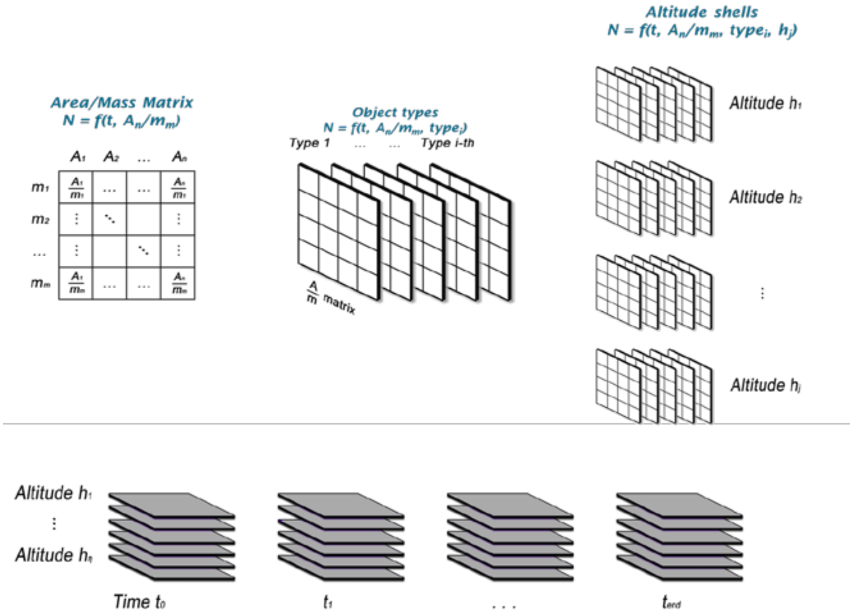

Figure 6-1. Schematics of the A/M discretisation in the altitude shells and over time.

Another improvement would be the inclusion of a fully proportional-integrative-derivative controller (PID, Figure 6-2). This PID controller could be based on the proportional one presented in Section 2.8.1, and expanded with an integrative part that takes into account the history of the population evolution and a derivative part that try to predict the future variation:

$$u(t) = k_P e(t) + k_I \int_0^t e(\tau)\, d\tau + k_D \frac{de}{dt}, \tag{6.1}$$

where k_P, k_I and k_D are the proportional, integral and derivative gains and $e(t)$ is the error with a set population (or density).

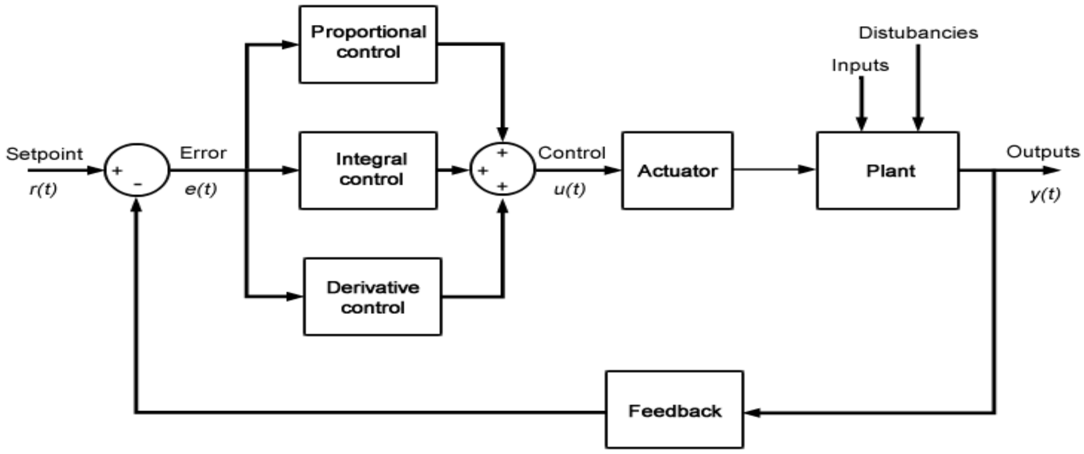

Figure 6-2. Schematics of a possible PID controller

The introduction of a Poisson extractor and Monte Carlo simulation will also make it possible to obtain probabilistic distribution on the simulation outcomes. Lastly, the already produced data could be used to perform additional studies to identify the correlations among the species and location of the removed objects.

Chapter 7. Conclusions

In the last decades, space-related services became more and more part of everyday life. Moreover, the commercial use of space (which includes the providers of such services) is forecast to keep increasing in the next decades. However, all the spacecraft which deliver these services are in constant risk of being damaged or destroyed by an orbital collision caused by space debris. To solve the problem, mitigation measures and standards have been defined at industrial, national, and international level; nevertheless, the number of debris keeps increasing. This increase poses a risk to the sustainable use of space, due for example to the increasing cost of monitoring activities, avoidance manoeuvres, spacecraft shielding, and a decrease in performances derived for example from the loss of sub-systems or solar panel cells. As a solution to the space debris problem, the active removal of debris from space has been proposed, and in recent years several studies have addressed the technical and technological challenges to realise the first successful complete ADR mission, with a technology demonstrator mission that, from September 2018 to February 2019, successfully performed experiments with a net capture device, a harpoon, and a visual navigation instrument (Taylor *et al.*, 2018; Surrey Satellite Technology Limited, 2019).

This thesis tested and measured the effectiveness of traditional PMD and ADR strategies in a wide range of scenarios when using a feedback controller with different control laws to select the number and location of the spacecraft to be removed in LEO.

Results confirmed the benefits of having a high PMD compliance, no matter the number of objects actively removed. It is of primary importance to increase the spacecraft compliance with PMD guidelines, but even with a 90% compliance level, their application alone is likely not sufficient to maintain a dynamic equilibrium of the LEO future population. As a result, several ADR strategies were tested in different conditions using different control laws, i.e. proportional, linear, and quadratic, on the total and partial density in each shell.

The results obtained from simulations that used the linear and quadratic control laws agreed that a similar population evolution could be achieved with multiple strategies varying the PMD compliance and the maximum annual removal rates. However, the effectiveness of ADR-strategies could be increased selecting optimal combinations of removals of inactive payloads and rocket bodies. Those optimal combinations of removals between rocket bodies and inactive payloads varied with the maximum annual removal rate allowed (and in magnitude with PMD compliance). When setting a maximum annual removal rate lower than 15, the strategies that maximise the effectiveness had about twice the rate for rockets bodies compared to inactive payloads. Increasing this rate, the optimal strategy shifted to a more balanced combination, with the exact number depending mainly on the PMD compliance level. In addition, it was proven that different control laws produced different results, with the highest NERF obtained with the quadratic control law.

Given the results obtained with this research, it is recommended to perform further studies to analyse the produced data, to investigate other control laws, and to identify the correlations among the species and location of the removed objects. A more complex version of the model, which includes more physical discretisation, such as on objects' mass, orbital eccentricity and inclination, would also contribute to the production of more detailed results. However, the controller and its ADR control law proposed in this thesis are independent of the model, and therefore it can be applied to other existing models and further expand its potentiality.

List of References

Anselmo, L., Rossi, A. and Pardini, C. (1999) ‘Updated results on the long-term evolution of the space debris environment’, *Advances in Space Research*, 23(1), pp. 201–211. doi: 10.1016/S0273-1177(99)00005-8.

Anz-Meador, P. D. (2016a) ‘Top Ten Satellite Breakups Reevaluated’, *Orbital Debris Quarterly News*, 20(1–2), pp. 5–6.

Anz-Meador, P. D. (2016b) ‘UNCOPUOS Reaches Consensus on the First Set of Guidelines for the Long-term Sustainability of Outer Space Activities’, *Orbital Debris Quarterly News*, 20(4), pp. 5–6.

Ariyoshi, Y. and Hanada, T. (2009) ‘GEODEEM4.0: Updated Model for Better Understanding GEO Debris Environment’, *27th International Symposium on Space Technology and Science*, pp. 1–6.

Azzarelli, T. (2015) ‘Future connectivity via LEO satellites’, in *techUK*. London, United Kingdom, pp. 1–10.

Bank of America Merrill Lynch (2017) *To Infinity And Beyond – Global Space Primer*. Available at: https://go.guidants.com/q/db/a2/1e1ffc185c1d44bd.pdf.

Barea, A., Urrutxua, H. and Cadarso, L. (2019) ‘Optimal large-scale object selection and trajectory planning for active space removal mission’, in *4th International Workshop on Key Topic in Orbit Propagatioin Applied to Space Situational Awareness*. Logroño, Spain.

Bastida Virgili, B. *et al.* (2016) ‘Risk to space sustainability from large constellations of satellites’, *Acta Astronautica*. Elsevier, 126, pp. 154–162. doi: 10.1016/j.actaastro.2016.03.034.

Bennett, J. C. and Sang, J. (2011) ‘Modelling the evolution of the low-Earth orbit debris population’, *11th Australian Space Science Conference*. Canberra, Australia, 33, pp. 165–178. doi: 10.1016/S0032-0633(98)00070-1.

Blake, R. and Lewis, H. G. (2014) ‘The effect of modelling assumptions on predictions of the space debris environement’, in *65th International Astronautical Congress*. Toronto, Canada.

Bonnal, C. and Mcknight, D. S. (2017) *IAA Situation Report on Space Debris - 2016*.

Bonnal, C., Ruault, J.-M. and Desjean, M.-C. (2013a) ‘Acta Astronautica Active debris removal : Recent progress and current trends’, *Acta Astronautica*, 85, pp. 51–60. doi: 10.1016/j.actaastro.2012.11.009.

Bonnal, C., Ruault, J.-M. and Desjean, M.-C. (2013b) ‘Active debris removal: Recent progress and current trends’, *Acta Astronautica*. Elsevier, 85, pp. 51–60. doi: 10.1016/j.actaastro.2012.11.009.

Celestrak (2012) *Iridium 33 / Cosmos 2251 Collision*. Available at: http://celestrak.com/events/collision/ (Accessed: 15 March 2018).

Celestrak (2014) *Satellite Catalog (SATCAT), Online Satellite Catalog - SATCAT*. Available at: http://www.celestrak.com/satcat/search.asp (Accessed: 7 September 2016).

Committee on Space Research (1972) ‘CIRA 1972: COSPAR International Reference Atmosphere 1972’. Berlin, German: Akademie-Verlag.

Cordelli, A. *et al.* (1993) ‘Future collisional evolution of Earth-orbiting debris’, *Advances in Space Research*, 13(8), pp. 215–219. doi: 10.1016/0273-1177(93)90593-Z.

Cordelli, A., Farinella, P. and Rossi, A. (1998) ‘The influence of the fragmentation threshold on the long term evolution of the orbital debris environment’, *Planetary and Space Science*, 46(6), pp. 691–699. doi: 10.1016/S0032-0633(97)00217-1.

Corley, B. (2016) ‘International Space Station Debris Avoidance Process’, *Orbital Debris Quarterly News*, 20(4), pp. 7–8.

DeLuca, L. T. *et al.* (2013) ‘Active space debris removal by a hybrid propulsion module’, *Acta Astronautica*. Elsevier, 91, pp. 20–33. doi: 10.1016/j.actaastro.2013.04.025.

Dolado-Perez, J. C., Di Costanzo, R. and Revelin, B. (2013) ‘Introducing Medee – a New Orbital Debris’, *Proceedings of the 6th European Conference on Space Debris, 22-25 April 2013*. Darmstadt, Germany, 2013(April), pp. 22–25.

Dolado-Perez, J. C., Pardini, C. and Anselmo, L. (2015) ‘Review of uncertainty sources affecting the long-term predictions of space debris evolutionary models’, *Acta Astronautica*. Elsevier, 113(June), pp. 51–65. doi: 10.1016/j.actaastro.2015.03.033.

Eichler, P. (1998) ‘Synergistic use of debris environment models for flexible, very long term projections’, 40(12), pp. 843–858.

Eichler, P. and Rex, D. (1990) ‘Chain reaction of debris generation by collisions in space - a final threat to spaceflight?’, *Acta Astronautica*, 22(C), pp. 381–387. doi: 10.1016/0094-5765(90)90043-K.

Eichler, P. and Reynolds, R. C. (1995) ‘A comparison of debris environment projections using the evolve and chain models’, *Advances in Space Research*. Edited by I. S. for O. and Photonics, 16(11), pp. 127–135. doi: 10.1016/0273-1177(95)98763-E.

Emanuelli, M. *et al.* (2014) ‘Conceptualizing an economically, legally, and politically viable active debris removal option’, *Acta Astronautica*. Elsevier, 104(1), pp. 197–205. doi: 10.1016/j.actaastro.2014.07.035.

ESA (2004) ‘European Code of Conduct for Space Debris Mitigation’, (1), pp. 1–20.

ESA Space Debris Office (2018) *ESA's Annual Space Environment Report, GEN-DB-LOG-00239-OPS-GR*. Available at: https://discosweb.esoc.esa.int/ web/guest/statistics.

European Space Agency (2011) *National Space Legislation*. doi: 10.1007/978-3-319-70431-9_3.

European Space Agency (2016) *Copernicus Sentinel-1A satellite hit by space particle*. Available at: http://www.esa.int/Our_Activities/Observing_the_Earth/Copernicus/Sentinel-1/Copernicus_Sentinel-1A_satellite_hit_by_space_particle (Accessed: 27 October 2016).

Farinella, P. and Cordelli, A. (1991) 'The proliferation of orbiting fragments: A simple mathematical model', *Science & Global Security*, 2(4), pp. 365–378. doi: 10.1080/08929889108426373.

Federal Communication Commission (2018a) *FCC authorizes SpaceX to Provide Broadband Services via Satellite Constellation, FCC News from the Federal Communication Commission*. Available at: https://transition.fcc.gov/Daily_Releases/Daily_Business/2018/db0329/DOC-349998A1.pdf (Accessed: 30 May 2018).

Federal Communication Commission (2018b) *FCC Boosts Satellite Broadband Connectivity & Competition, FCC News from the Federal Communication Commission*. Available at: https://www.fcc.gov/document/fcc-boosts-satellite-broadband-connectivity-competition.

Flegel, S. K. *et al.* (2011) *Maintenance of the ESA MASTER Model – Final Report, ESA Contract Number: 21705/08/D/HK*. European Space Agency.

Government of Canada and Natural Resources Canada (2017) *Solar radio flux - Archive of measurements*. Available at: http://www.spaceweather.gc.ca/solarflux/sx-5-en.php (Accessed: 27 July 2017).

Hoedin, A. . (1987) 'MSIS-86 Thermospheric Model', *Journal of Geophysical Research: Space Physics*, 92(A5), pp. 4649–4662.

Houston, P. L. (2000) *Chemical Kinetics and Reaction Dynamics*. Dover Book. Edited by C. Corporation.

Inter-Agency Space Debris Coordination Committee (2007) *IADC Space Debris Mitigation Guidelines*.

Inter-Agency Space Debris Coordination Committee *et al.* (2013) *Stability of the Future LEO Environment*. doi: IADC-12-08, Rev. 1.

International Organization for Standardization (2010) *ISO 24113, Space systems, Space debris mitigation requirements*. Available at: https://www.iso.org/standard/42034.html.

Johnson, N. L. *et al.* (2001) 'NASA's new breakup model of EVOLVE 4.0', *Advances in Space Research*, 28(9), pp. 1377–1384. doi: 10.1016/S0273-1177(01)00423-9.

Kebschull, C. *et al.* (2013) ‘A simplified approach to analyze the space debris evolution in the Low Earth Orbit’, in *64th International Astronautical Congress*. Beijing, China.

Kebschull, C. *et al.* (2014) ‘Simulation of the space debris environment in LEO using an analytical approach’, in *40th COSPAR Scientific Assembly*. COSPAR, pp. 166–180. doi: 10.1016/j.asr.2016.08.005.

Kebschull, C. *et al.* (2016) ‘Simulation of the space debris environment in LEO using an analytical approach’, *Advances in Space Research*. COSPAR. doi: 10.1016/j.asr.2016.08.005.

Kessler, D. J. *et al.* (2010) ‘The Kessler Syndrome: Implications to Future Space operations’, *Advances in the Astronautical Sciences*, 137(8), pp. 47–62.

Kessler, D. J. (2016) ‘A Brief History of Orbital Debris Programs and the Increasing Need for Debris Removal’, in *4th Workshop on Debris Modelling and Remediation*. Paris, France.

Kessler, D. J. and Anz-Meador, P. D. (2001) ‘Critical number of spacecraft in low Earth orbit: using satellite fragmentation data to evaluate the stability of the orbital debris environment’, in Sawaya-Lacoste, H. (ed.) *3rd European Conference on Space Debris*. Darmstadt, Germany: ESA Publications Division, Noordwijk, Netherlands, pp. 265–272.

Kessler, D. J. and Cour-Palais, B. G. (1978) ‘Collision frequency of artificial satellites: The creation of a debris belt’, *Journal of Geophysical Research*, 83(A6), pp. 2637–2646. doi: 10.1029/JA083iA06p02637.

Kessler, D. J., Reynolds, R. C. and Anz-Meador, P. D. (1989) ‘Orbital debris environment for spacecraft designed to operate in low Earth orbit’, *Nasa TM-100 471*. doi: 10.2514/3.26250.

King-Hele, D. G. (1987) *Satellite Orbits in an Atmosphere: Theory and Application*. Glasgow: Blackie and Son Ltd., Glasgow, U.K.

Krisko, P. H. (2011) ‘Proper Implementation of the 1998 NASA Breakup Model’, *Orbital Debris Quarterly News*, 15(4), pp. 4–5.

Krisko, P. H., Johnson, N. L. and Opiela, J. N. (2001) ‘Evolve 4.0 Orbital Debris Mitigation Studies’, *Advances in Space Research*, 28(9), pp. 1385–1390. doi: 10.1016/S0273-1177(01)00425-2.

Lafleur, J. M. (2011) ‘Extension of a simple mathematical model for orbital debris proliferation and mitigation’, *Advances in the Astronautical Sciences*, 140, pp. 1037–1056.

Larson, W. J. and Wertz, J. R. (1999) *Space Mission Analysis and Design*. 3rd ed., *Book*. 3rd ed. Edited by The Space Technology Library Editorial Board. Microcosm Press and Kluwer Academic Publishers.

Lewis, H. G. *et al.* (2001) ‘DAMAGE: a dedicated GEO debris model framework’, *3rd European*

Conference on Space Debris. Edited by Huguette Sawaya-Lacoste. Noordwijk, Netherlands: The European Space Agency (ESA), 1(ESA SP-473), pp. 373–378.

Lewis, H. G. *et al.* (2009a) ‘Active removal study for on-orbit debris using DAMAGE’, in *5th European Conference on Space Debris*. European Space Agency.

Lewis, H. G. *et al.* (2009b) ‘The fast debris evolution model’, *Advances in Space Research*. COSPAR, 44(5), pp. 568–578. doi: 10.1016/j.asr.2009.05.018.

Lewis, H. G. *et al.* (2011) ‘Effect of thermospheric contraction on remediation of the near-Earth space debris environment’, *Journal of Geophysical Research: Space Physics*, 116(January), pp. 1–10. doi: 10.1029/2011JA016482.

Lewis, H. G. (2011) ‘The University of Southampton’s DAMAGE Model’, in *ReVuS General Assembly*. Southampton, England.

Lewis, H. G., White, A. E. and Stokes, H. P. (2012) ‘The Effectiveness of Space Debris Mitigation Measures’, in *ISU Annual International Symposium*. Strasbourg, France, pp. 1–11.

Lindsay, M. (2016) ‘OneWeb – Overview’, in *53rd Session of the Scientific and Technical Subcommittee of the UNCOPOUS*. Wien, Austria, pp. 1–18.

Lindsay, M. (2017) ‘OneWeb’s Approach to Space Debris Mitigation’, in *United Nations/United Arab Emirates - High Level Forum: Space as a Driver for Socio-Economic Sustainable Development*. Dubai, United Emirates. Available at: http://www.unoosa.org/documents/pdf/hlf/HLF2017/presentations/Day3/Special_Session/Presentation2.pdf.

Liou, J.-C. *et al.* (2003) ‘A New Approach To Evaluate Collision Probabilities Among Asteroids, Comets’, *Lunar and Planetary Science*, XXXIV, pp. 2–3.

Liou, J.-C. *et al.* (2004) ‘LEGEND – A three-dimensional LEO-to-GEO debris evolutionary model’, *Advances in Space Research*, 34(5), pp. 981–986. doi: 10.1016/j.asr.2003.02.027.

Liou, J.-C. (2006) ‘Collision activities in the future orbital debris environment’, *Advances in Space Research*, 38(9), pp. 2102–2106. doi: 10.1016/j.asr.2005.06.021.

Liou, J.-C. (2007) ‘Detection of Orbital Debris from Chinese ASAT Test Increases; One Minor Fragmentation Event in Second Quarter of 2007’, *Orbital Debris Quarterly News*, 11(3), pp. 1–2.

Liou, J.-C. (2011a) ‘A Note on Active Debris Removal’, *Orbital Debris Quarterly News*, 15(3), pp. 7–8.

Liou, J.-C. (2011b) ‘An active debris removal parametric study for LEO environment remediation’, *Advances in Space Research*. COSPAR, 47(11), pp. 1865–1876. doi: 10.1016/j.asr.2011.02.003.

Liou, J.-C. (2011c) ‘Project Review: An Update on LEO Environment Remediation with Active

Debris Removal', *NASA Orbital Debris Quarterly News (ODQN)*, 15(2), pp. 4–6.

Liou, J.-C. (2012) *Orbital Debris Modeling*. Available at: http://www.ntrs.nasa.gov/archive/nasa/casi.ntrs.nasa.gov/20120003286_2012003361.pdf.

Liou, J.-C. *et al.* (2013) 'Stability of the Future Leo Environment – an IADC Comparison Study', *6th European Conference on Space Debris*. Darmstadt, Germany: European Space Agency, (November 2015), pp. 1–8. doi: 10.13140/2.1.3595.6487.

Liou, J.-C. (2014) 'Fengyun-1C Debris Cloud Remains Hazardous', *Orbital Debris Quarterly News*, 18(1), pp. 2–3.

Liou, J.-C. (2018) 'U. S. Space Debris Environment, Operations , and Research Updates', in *55th Session of the Scientific and Technical Subcommittee Committee on the Peaceful Uses of Outer Space, United Nations*. Vienna, Austria.

Liou, J.-C. and Johnson, N. L. (2005) 'A LEO satellite postmission disposal study using legend', *Acta Astronautica*, 57(2–8), pp. 324–329. doi: 10.1016/j.actaastro.2005.03.002.

Liou, J.-C. and Johnson, N. L. (2009) 'A sensitivity study of the effectiveness of active debris removal in LEO', *Acta Astronautica*, 64(2–3), pp. 236–243. doi: 10.1016/j.actaastro.2008.07.009.

Liou, J.-C., Johnson, N. L. and Hill, N. M. (2010) 'Controlling the growth of future LEO debris populations with active debris removal', *Acta Astronautica*. Elsevier, 66(5–6), pp. 648–653. doi: 10.1016/j.actaastro.2009.08.005.

Lucken, R. and Giolito, D. (2018) 'Collision risk prediction for constellation operators', in *69th International Astronautical Congress*. Bremen, Germany.

Mcknight, D. S. *et al.* (2013) 'System engineering analysis of derelict collision prevention options', *Acta Astronautica*. Elsevier, 89, pp. 248–253. doi: 10.1016/j.actaastro.2013.04.016.

Mcknight, D. S. (2016) 'Operational Success Framework for Orbital Debris Management', in *Stardust Global Virtual Workshop*. Southampton, United Kingdom.

Mcknight, D. S., Maher, R. and Nagl, L. (1995) 'Refined Algorithms for Structural Breakup due to Hypervelocity Impact', *International Journal of Impact Engineering*, 17(4–6), pp. 547–558. doi: 10.1016/0734-743X(95)99879-V.

Morand, V. *et al.* (2014) 'Analysis of Mitigation Guidelines Compliance At International Level in Low Earth Orbit', in *65th International Astronautical Congress*. Toronto, Canada.

NASA Orbital Debris Program Office (2000) 'ISS Performs First Collision Avoidance Maneuver', *Orbital Debris Quarterly News*, 5(1), p. 7.

NASA Orbital Debris Program Office (2001) 'GOES 2 and Landsat 4 Retired', *Orbital Debris Quarterly News*, 6(3), p. 4.

Nazarenko, A. I. (1997) ‘The Development of the Statistical Theory of a Satellite Ensemble Motion and its Application to Space Debris Modeling’, in *2nd European Conference on Space Debris*. Darmstadt, Germany: European Space Agency, pp. 233–238. doi: 10.1017/CBO9781107415324.004.

Nyberg, B. (1999) ‘An Introductory Guide to Adaptive Management for Project Leaders and Participants’, *British Columbia Forest Service, Victoria, Canada*, p. 24.

OneWeb (2017) *OneWeb Satellites Breaks Ground On The World’ s First State-Of-The-Art High-Volume Satellite Manufacturing Facility, Press release*. Available at: http://oneweb.world/press-releases/2017/oneweb-satellites-breaks-ground-on-the-worlds-first-state-of-the-art-high-volume-satellite-manufacturing-facility (Accessed: 4 September 2017).

OneWeb (2019) *OneWeb makes history as first launch mission is a success*. Available at: https://www.oneweb.world/newsroom/oneweb-makes-history-as-first-launch-mission-is-a-success (Accessed: 10 March 2019).

Oswald, M. *et al.* (2005) ‘The MASTER 2005 Model’, in *European Space Agency, (Special Publication) ESA SP*, pp. 235–242.

Pardini, C. and Anselmo, L. (2014) ‘Review of past on-orbit collisions among cataloged objects and examination of the catastrophic fragmentation concept’, *Acta Astronautica*. Elsevier, 100(1), pp. 30–39. doi: 10.1016/j.actaastro.2014.03.013.

Pardini, C. and Anselmo, L. (2016) ‘Characterization of Abandoned Rocket Body Families for Active Removal’, *Acta Astronautica*. Elsevier, 126, pp. 243–257. doi: 10.1016/j.actaastro.2016.04.035.

Praly, N. *et al.* (2012) ‘Study on the eddy current damping of the spin dynamics of space debris from the Ariane launcher upper stages’, *Acta Astronautica*, 76, pp. 145–153. doi: 10.1016/j.actaastro.2012.03.004.

Radtke, J. *et al.* (2014) ‘Deriving the Spacecraft Criticality from Monte-Carlo Simulations of the Space Debris Environment’, in *Proceedings of the 65th International Astronautical Congress*. Toronto, Canada.

Radtke, J., Kebschull, C. and Stoll, E. (2017) ‘Interactions of the space debris environment with mega constellations - Using the example of the OneWeb constellation’, *Acta Astronautica*. Elsevier, 131(May 2016), pp. 55–68. doi: 10.1016/j.actaastro.2016.11.021.

Revelin, B., Di Costanzo, R. and Dolado-Perez, J. C. (2015) ‘Sensitivity Analysis of the long-term evolution of the space debris population in LEO’, *Journal of Space Safety Engineering*. Elsevier Masson SAS, 2(1), pp. 12–22. doi: IAC-14,A6,2,3,x21657.

Reynolds, R. C., Fischer, N. H. and Edgecombe, D. S. (1983) ‘A model for the evolution of the on-orbit man-made debris environment’, *Acta Astronautica*, 10(7), pp. 479–498. doi: 10.1016/0094-5765(83)90020-6.

Rossi, A. *et al.* (1994) ‘Collisional evolution of the Earth’s orbital debris cloud’, *Journal of Geophysical Research*, 99(E11), pp. 23,195-23,210. doi: 10.1029/94JE02320.

Rossi, A. *et al.* (1997) ‘Long term evolution of the space debris population’, *Advances in Space Research*, 19(2), pp. 331–340. doi: 10.1016/S0273-1177(97)00022-7.

Rossi, A. *et al.* (1998) ‘Modelling the evolution of the space debris population’, *Planetary and Space Science*, 46(11/12), pp. 1583–1596. doi: 10.1016/S0273-1177(97)00022-7.

Rossi, A. *et al.* (2009) ‘The New Space Debris Mitigation (SDM 4.0) Long Term Evolution Code’, in *5th European Conference on Space Debris*. Darmstadt, Germany: ESA.

Rossi, A., Cordelli, A. and Pardini, C. (1995) ‘Modelling the space debris evolution: Two new computer codes’, *Advances in the Astronautical Sciences-Space Flight Mechanics*, pp. 1–15. doi: 10.1.1.27.1460.

Rossi, A., Valsecchi, G. B. and Alessi, E. M. (2015) ‘The Criticality of Spacecraft Index’, *Advances in Space Research*. COSPAR, 56(3), pp. 449–460. doi: 10.1016/j.asr.2015.02.027.

Rossi, A. and Valsecchi, G. B. B. (2006) ‘Collision risk against space debris in Earth orbits’, *Celestial Mechanics and Dynamical Astronomy*, 95(1–4), pp. 345–356. doi: 10.1007/s10569-006-9028-7.

Saunders, A. (2012) *An empirical Model of Long-Term Thermospheric Density Change*.

Somma, G. L., Colombo, C. and Lewis, H. G. (2017) ‘A Statistical LEO Model to Investigate Adaptable Debris Control Strategies’, in Flohrer, T. and Schmitz, F. (eds) *7th European Conference on Space Debris*. Darmstadt, Germany: ESA Space Debris Office. doi: 10.13140/2.1.

Somma, G. L., Lewis, H. G. and Colombo, C. (2016) ‘Adaptive remediation of the space debris environment using feedback control’, in *67th International Astronautical Congress (IAC)*. Guadalajara, Mexico, pp. 26–30. doi: 10.13140/RG.2.2.21467.26404.

Somma, G. L., Lewis, H. G. and Colombo, C. (2017) ‘Increasing ADR effectiveness via an altitude-shell-dependent removal approach’, in *68th International Astronautical Congress*. Adelaide, Australia. Available at: https://www.researchgate.net/publication/329098120.

Somma, G. L., Lewis, H. G. and Colombo, C. (2018a) ‘Space Debris, how to increase the active removal effectiveness’, in *5th European Workshop on Space Debris Modeling and Remediation*. CNES HQ, Paris, France. doi: 10.13140/RG.2.2.14722.32960.

Somma, G. L., Lewis, H. G. and Colombo, C. (2018b) ‘Space Debris: Analysis of a Large Constellation at 1200 km Altitude’, in *69th International Astronautical Congress*. Bremen, Germany. doi: 10.13140/RG.2.2.34854.98889.

Somma, G. L., Lewis, H. G. and Colombo, C. (2019) ‘Sensitivity analysis of launch activities in Low Earth Orbit’, *Acta Astronautica*, 158, pp. 129–139. doi: 10.1016/j.actaastro.2018.05.043.

Space Foundation (2015) *Space Foundation Report Reveals Global Space Economy at $ 323 Billion in 2015, 22 June*. Available at: http://www.spacefoundation.org/media/press-releases/space-foundation-report-reveals-global-space-economy-323-billion-2015 (Accessed: 7 September 2016).

SpaceX (2016) *Federal Communications Commision filing, Purpose of Experiment*. Available at: https://apps.fcc.gov/els/GetAtt.html?id=185534.

Stokes, H. P. *et al.* (2017) ‘Status of the ISO space debris mitigation standards (2017)’, in *7th European Conference on Space Debris*. Darmstadt, Germany: ESA Space Debris Office.

Su, S. (1993) ‘On runaway conditions of orbital debris environment’, *Advances in Space Research*, 13(8), pp. 221–224. doi: 10.1016/0273-1177(93)90594-2.

Su, S. and Kessler, D. J. (1985) ‘Contribution of explosion and future collision fragments to the orbital debris environment’, *Advances in Space Research*, 5(2), pp. 25–34. doi: 10.1016/0273-1177(85)90384-9.

Surrey Satellite Technology Limited (2019) *RemoveDEBRIS: success for harpoon experiment*. Available at: https://www.sstl.co.uk/media-hub/latest-news/2019/removedebris-success-for-harpoon-experiment (Accessed: 20 February 2019).

Talent, D. L. (1990) ‘Analytical Model for Orbital Debris Environment Management’, in *AIAA/NASA/DoD Orbital Debris Conference: Technical Issues & Future Directions*, pp. 90–1363.

Talent, D. L. (1992) ‘Analytic Model for Orbital Debris Environmental Management’, *Journal of Spacecraft and Rockets*, 29(4), pp. 508–513. doi: 10.2514/3.25493.

Talent, D. L. (2007) ‘An Assessment of the Impact of the January 2007 Chinese ASAT Test on the LEO Environment’, in *AMOS Conference Proceedings (Advanced Maui Optical and Optical and Space Surveillance Technologies Conference)*, pp. 1–11.

Taylor, B. *et al.* (2018) ‘RemoveDebris Preliminary Mission Results’, in *69th International Astronautical Congress,*. Bremen, Germany.

The United Kingdom (1986) *The Outer Space Act 1986*.

Union of Concerned Scientists (2016) *Union of Concerned Scientists Database, Database*. Available at: http://www.ucsusa.org/nuclear_weapons_and_global_security/space_weapons/technical_issues/ucs-satellite-database.html (Accessed: 7 September 2016).

United Nations Committee On the Peaceful Uses of Outer Space (2007) ‘Report of the Scientific and Technical Subcommittee', in *44th session of the Scientific and Technical Subcommittee of the Committee on the Peaceful Uses of Outer Space*. Vienna, Austria. doi: 10.1093/oxfordhb/9780199560103.003.0005.

United Nations Committee On the Peaceful Uses of Outer Space (2010) *United Nations Space Debris Mitigation Guidelines of the Committee on the Peaceful Uses of Outer Space*. Vienna, Austria.

United Nations Committee On the Peaceful Uses of Outer Space (2017) 'Report of the Committee on the Peaceful Uses of Outer Space to the 18th Session of the United Nations General Assembly', in *International Legal Materials*. United Nations Committee on the Peaceful Uses of Outer Space, pp. 1058–1065. doi: 10.1017/s0020782900054498.

Vallado, D. A. (2013) *Fundamentals of Astrodynamics and Applications*. 4th edn. Edited by T. S. T. Library. Hawthorne, CA: Microcosm Press and Springer.

Walker, R. *et al.* (2001) 'Analysis of the effectiveness of space debris mitigation measures using the DELTA model', *Advances in Space Research*, 28(9), pp. 1437–1445. doi: 10.1016/S0273-1177(01)00445-8.

Walker, R. *et al.* (2002) 'Sensitivity of long-term orbital debris environment evolution to the deployment of nano-satellite swarms', *Acta Astronautica*, 51(1–9), pp. 439–449. doi: 10.1016/S0094-5765(02)00095-4.

Weeden, B. (2011) 'Overview of the legal and policy challenges of orbital debris removal', *Space Policy*. Elsevier Ltd, 27(1), pp. 38–43. doi: 10.1016/j.spacepol.2010.12.019.

Wetherill, G. W. (1967) 'Collisions in the Asteroid Belt', *Journal of Geophysical Research*, 72(9), pp. 2429–2444. doi: 10.1029/JZ072i009p02429.

White, A. E. (2014) *An Adaptive Strategy to Control the Space Debris Population*. University of Southampton.

White, A. E. and Lewis, H. G. (2014a) 'An adaptive strategy for active debris removal', *Advances in Space Research*. COSPAR, 53(8), pp. 1195–1206. doi: 10.1016/j.asr.2014.01.021.

White, A. E. and Lewis, H. G. (2014b) 'The many futures of active debris removal', *Acta Astronautica*. Elsevier, 95(1), pp. 189–197. doi: 10.1016/j.actaastro.2013.11.009.

Yamamoto, T., Okamoto, H. and Kawamoto, S. (2017) 'Cost Analysis of Active Debris Removal Scenarios', *7th European Conference on Space Debris*, (July), pp. 1–15.